The Seismic Velocity Structure of the Wadati-Benioff Zone – Insights from Guided Waves

Thesis submitted in accordance with the requirements of the University of Liverpool for the degree of Doctor in Philosophy by,

Thomas Ian Michael Garth

February 2014

Abstract

Low velocity hydrous minerals in the subducting plate deliver water to the mantle and are thought to cause intermediate depth Wadati-Benioff zone (WBZ) seismicity through dehydration embrittlement. High frequency seismic energy (> 2 Hz) from intermediate depth earthquakes that occur within this low velocity oceanic crust is retained and delayed by the crustal waveguide while lower frequency (< 0.5 Hz) energy travels at the faster velocities of the surrounding mantle. These guided waves therefore spend longer interacting with the low velocity oceanic crust than any other seismic phase, and have the potential to reveal a large amount about the velocity structure of the WBZ. Dispersive arrivals recorded in the forearc of Northern Japan are directly compared to synthetic waveforms produced from full 2D and 3D waveform simulations. Comparing the relative amplitude and arrival time of a given frequency using the velocity spectra and spectrogram respectively, allows the full dispersive P-waveform to be constrained. Analysis of dispersive arrivals from upper plane WBZ events at 150 – 220 km depth place the first observational constraints on the metamorphic reactions occurring before full eclogitisation of the subducting oceanic crust. I show that blueschist and lawsonite bearing rocks may persist well beyond the depths inferred from established thermo-petrological subduction zone models, and that full eclogitization may occur at much greater depths than is inferred by receiver function studies. The persistence of meta-stable hydrous minerals explains the occurrence of WBZ seismicity at 200 - 250 km depth, and may be due to the partially hydrated oceanic crust. Dispersion from events that occur well below the upper plane of WBZ seismicity can be explained by the occurrence of low velocity hydrated outer rise normal faults at intermediate depths. At depth, these faults are inferred to be 2 - 3 km thick and 12 - 15 % slower that the surrounding mantle, suggesting they are 50 - 71 % serpentinised. We suggest that the extended P-wave coda observed at stations close to the trench in Northern Japan are explained by low velocity dipping faults of a range of scale lengths forming a scattering medium. This scattering medium is simulated using a von Kármán function, and the synthetic waveforms produced are compared to the observed P-wave coda, that decays in amplitude with distance from the trench. The magnitude of this spatial coda decay is sensitive to the average bulk velocity of the scattering medium and provides a constraint on the hydration of the lithospheric mantle subducted beneath Japan. This first in-situ constraint on the degree of slab mantle hydration at intermediate depth suggests that 170.4 - 318.7 Tg/Myr/m of water is subducted beneath Northern Japan by the slab mantle. In summary we have shown that up to 94 % of the water subducted beneath Northern Japan is transported by the lithospheric mantle, and that upper and lower planes of WBZ zone seismicity are directly related to hydrous mineral assemblages, and so may occur through dehydration embrittlement. This work shows that guided waves have the potential to resolve new details of the WBZ velocity structure and the techniques developed here can be applied to other subduction zone settings.

Acknowledgements

Firstly thanks go to Andreas for proposing such an interesting project, and for his supervision, help and motivation throughout my PhD. I would also like to thank Nick, for his interest and support throughout the project, and Alex and Stuart for their help and advice especially in the early stages of my studies. Thanks also go to Andy and Xiao for their technical help. Most importantly though thanks go to Christina for being my primary go to for all problems, academic or otherwise.

I thank the authors of the codes SOFI2D and SOFI3D for making their codes freely available for academic use. My thanks go also to Abers & Hacker for making the *Subduction Factory 4* Excel macro freely available, and to Anna Fry for allowing me to use her Millimin subduction zone modelling code. In this project we have used seismic data from the Global Seismic Network distributed by IRIS. We have also used seismic data from F-net broadband seismic network and earthquake locations from the Japanese Meteorological Agency distributed by NEID. This work was supported by a NERC studentship (grant number NE/H524722/1) and was made possible by the resources that we were allocated on various generations of the UK National supercomputer HECTOR.

Contents

The Seismic Velocity Structure of the Wadati-Benioff Zone – Insights from Guided Waves

Abstract ..... **i**

Acknowledgements ..... **ii**

Contents ..... **iii**

Chapter 1 – Introduction **1**

1.1 Motivation and hypothesis 2

1.2 Agenda 3

Chapter 2 – The Wadati-Benioff zone **5**

2.1 Inferring and imaging low velocity structure in the WBZ 6

2.1.1 Guided waves observations in subduction zones 7

2.1.2 Converted seismic phases in subduction zones 10

2.1.3 High resolution seismic tomography 11

2.1.4 Observations of outer rise normal faulting 13

2.1.5 Summary of observations 14

2.2 Modelling hydration of the WBZ 15

2.2.1 Hydration of the oceanic lithosphere 15

2.2.2 Dehydration of the subducting slab 16

2.3 Summary 22

Part one – Modelling and Measuring Subduction Zone Guided Wave Dispersion

Chapter 3 – Waveform Modelling Using the Finite Difference Method **25**

3.1 The Elastic Case 25

3.2 The Visco-Elastic Case 27

3.3 Boundary Conditions 31

3.3.1 The free surface 32

3.3.2 Absorbing Boundaries 32

3.3.3 Perfectly Matched Layers 32
3.3.4 Exponential Dampening 33
3.4 Source Implementation 34
3.4.1 Source Time Function 34
3.4.2 Explosive Source 34
3.4.3 Double Couple Source 35
3.5 Stability Criterion 36
3.5.1 Temporal stability criterion 36
3.5.2 Spatial stability criterion 36
3.6 Domain Decomposition 37
3.7 Summary 38

Chapter 4 – Constraining Guided Wave Dispersion with Full Waveform Modelling 41
4.1 Measuring Dispersed Waveforms 41
4.1.1 Measuring dispersed first arrivals 42
4.1.2 Waveform Comparison 44
4.1.3 Measuring P-wave coda 45
4.2 Numerical model setup 47
4.2.1 Deterministic Seismic Structure 48
4.2.2 Non–Deterministic Seismic Structure 51
4.2.3 Waveform Modelling in 2D and 3D 54
4.2.4 2D model setup 54
4.2.5 3D model setup 56
4.3 Summary 59

Part two – Guided Waves in Subducted Lithosphere

Chapter 5 –Order of magnitude increase in subducted H2O due to hydrated normal faults within the Wadati-Benioff zone 61
5.1 Introduction 61
5.2 Dispersed P-wave arrivals 63
5.3 P-wave coda analysis 67
5.4 Calculating the degree of slab mantle serpentinisation and hydration 72
5.5 Discussion 73
5.6 Conclusions 75

Chapter 6 – Down Dip Velocity Changes in Subducted Oceanic Crust beneath Northern Japan – Insights from Guided Waves **77**

6.1 Introduction 78

6.2 Guided Wave Observations 80

6.3 Modelling guided waveforms 81

6.3.1 Model setup 81

6.3.2 Constraining Guided Waveforms 83

6.3.Calculating the combined misfit 83

6.4 Determining waveguide velocity structure 84

6.4.1 Waveguide thickness 87

6.4.2 Waveguide velocity 88

6.4.3 Waveform fitting 88

6.5 Attenuation Structure 91

6.5.1 Mantle wedge Q 91

6.5.2 Reduced Q in the LVL 91

6.6 3D Modelling 94

6.6.1 3D Model Setup 94

6.6.2 Benchmarking 2D and 3D models 95

6.7 Variable Down-Dip Velocity Contrast 96

6.7.1 Variable velocity LVL 97

6.7.2 Variable velocity model with fault zones 99

6.8 Calculating MORB Phase Velocities 102

6.9 Discussion 103

6.9.1 Velocity Structure 103

6.9.2 Modelling in 3D 105

6.9.3 Attenuation structure 105

6.10 Conclusions 106

Part three – Summary and Context

Chapter 7 – Discussion and further work **108**

7.1 Hydrated fault zones in the slab mantle 108

7.2 Metamorphic reactions in the subducted oceanic crust 110

7.3 Water delivered to the deep mantle 112

7.4 Intermediate and deep focus seismicity 114

7.5 Other observations 115
7.6 Further work 117
7.6.1 South American observations 117
7.6.2 Scattering analysis 117
7.6.3 Petrological modelling 119
7.7 Summary 119

Chapter 8 – Conclusions **120**
8.1 Fault zone structures in the subducted mantle beneath Northern Japan..... 120
8.2 Hydration of the subducting lithospheric mantle 121
8.3 Depth of phase changes in the subducted oceanic crust 121
8.4 Further work 122

References..... **123**
Appendix – Dispersed P-wave Arrivals in South America **134**

Chapter 1

Introduction

At subduction zones cool dense oceanic lithosphere sinks into the warmer less dense mantle. The presence of subducted lithosphere at depth can be inferred due to the occurrence of intermediate and deep focus earthquakes, referred to as the Wadati-Benioff zone (WBZ). Tomographic images of the upper mantle also resolve the high seismic velocities of the cool subducting lithosphere (e.g. van der Hilst *et al.,* 1991).

Subducted oceanic crust is thought to be hydrated due to hydrothermal circulation close to the mid-ocean ridge where oceanic lithosphere is formed (e.g. Fowler 2005). The lithospheric mantle is also thought to be hydrated due to normal faulting at the outer rise as the plate bends into the subduction zone (e.g. Peacock, 2001). During subduction the pressure and temperature of the oceanic lithosphere increases causing the hydrous mineral assemblages in the crust to breakdown. It is widely proposed that these metamorphic reactions cause the intermediate depth seismicity seen in subduction zones across the globe through dehydration embrittlement (e.g. Kirby *et al.,* 1996a; Hacker *et al.,* 2003a & b), and that water released from these reactions causes melting within the mantle wedge that leads to the volcanic arc seen above the subducting plate (e.g. Grove *et al.,* 2009).

The hydrated mineral assemblages that are predicted to occur in the subducting slab by thermo-petrological modelling are expected to have much lower seismic velocities than the surrounding mantle material (e.g. Helffrich, 1996; Connolly & Kerrick, 2002, Hacker *et al.,* 2003 a & b). Seismic studies in a range of subduction zones have detected this low velocity material from converted seismic phases (e.g. Yuan *et al.,* 2000), and more recently high resolution seismic tomography studies (e.g. Zhang *et al.,* 2004).

It has also been proposed that dispersive arrivals seen in the subduction zone forearc can be explained by this low velocity oceanic crust acting as a seismic waveguide (e.g. Abers, 2000). High frequency seismic energy is retained by the low velocity structure, while lower frequencies travel at the velocity of the surrounding mantle material. The high frequency energy then decouples from the low velocity crustal waveguide due to the bend of the slab, and so is observed at appropriately placed stations in the subduction zone forearc (e.g.

Martin *et al.,* 2003). These seismic phases spend much of their ray path interacting with the low velocity slab, and therefore have the potential to resolve new details of the low velocity structure seen at intermediate depths in subduction zones.

In this study we investigate the resolution of these guided wave phases, and show that guided wave dispersion can not only occur in arrivals from upper plane WBZ seismicity due to low velocity oceanic crust, but can also be seen from lower plane WBZ. We show that dispersive arrivals from the lower plane of the WBZ may be due to low velocity hydrated outer rise normal faults that penetrate the lithospheric mantle. We propose an innovative method for constraining the velocity structure responsible for the guided wave dispersion seen, by comparing the full dispersive waveforms observed in the forearc to synthetic waveforms produced by full waveform simulations.

Using this method we show that upper plane WBZ events are associated with low velocity oceanic crust that becomes less seismically distinct with depth. These observations give the first seismic evidence of dehydration reactions occurring before the onset of full eclogitization, and confirm that dehydration reactions occur within the subducted crust as predicted by thermo-petrological subduction zone models (e.g. Hacker *et al.,* 2003 a & b; Yamasaki & Seno, 2003). Our observations suggest however that low velocity lawsonite bearing assemblages persist to greater depth than has previously been suggested by thermo-petrological subduction zone models or observations of converted seismic phases.

We also show that the subducting lithospheric mantle is hydrated by serpentinised outer rise normal faults. Analysis of the P-wave coda from events in Northern Japan gives an in-situ constraint on the hydration of the lithospheric mantle, increasing the amount of water that is thought to be delivered to the mantle by this subduction zone by an order of magnitude compared to previous studies (e.g. van Keken *et al.,* 2011)

1.1 Motivation and hypothesis

Subduction zone modelling has suggested that hydrous mineral phases in subduction zones not only have a fundamental control on the occurrence of both upper and lower plane WBZ seismicity (e.g. Hacker *et al.,* 2003b), but also have an important role in the global water cycle as subduction transports large amounts of water to the mantle (e.g. van Keken *et al.,* 2011). While established seismic imaging techniques have shown that low velocity hydrous mineral assemblages occur at the depths predicted by these models, these methods

generally lack the resolution to resolve the predicted mineral phase transformations other than the transformation to high velocity eclogite.

The lack of observational benchmarks for these established subduction zone models is perhaps most apparent in the subducted lithospheric mantle. It is widely suggested that the oceanic lithosphere may be highly hydrated by outer rise normal faulting, but there is little observational constraint on the degree of hydration at intermediate depths. This introduces a large degree of uncertainty to current estimates of the amount of water delivered, especially to the deep mantle (e.g. van Keken *et al.,* 2011)

Guided waves spend longer interacting with the subducted oceanic lithosphere than any other seismic phase. Detailed analysis of guided wave arrivals may therefore be more sensitive to these hydrated subduction zone structures than other seismic techniques.

1.2 Agenda

In this project we present a suite of methods for constraining guided wave arrivals. Direct comparison of the dispersive waveforms recorded in the subduction zone forearc with synthetic waveforms produced by full waveform simulations allows the velocity structure of the WBZ to be tightly constrained. These methods provide a new constraint on the structures and mineralogies that are associated with upper and lower plane WBZ seismicity, and give the first in-situ estimates of the hydration of the lithospheric mantle.

This thesis is presented in two main parts:

Part one - Modelling and Measuring Subduction Zone Guided Waves

Part two - Guided Waves in Subducted Lithosphere

This is prefaced with this introduction and a literature review (Chapter 2). In Chapter 2 we first discuss existing observations linked to WBZ structure, and secondly outline the mineralogies and structures that are predicted by thermo-petrological modelling studies.

In Part one of the thesis the methodologies that are used and developed in this project are discussed. Chapter 3 outlines the Finite Difference (FD) method used to produce synthetic waveforms, and Chapter 4 introduces the methods developed for constraining the dispersive arrivals observed from intermediate depth events.

Part two of the thesis focuses on the application of these methods to dispersive arrivals observed in subduction zone forearcs. In Chapter 5 we present dispersive arrivals from events that occur well below the upper plane of the WBZ in Northern Japan. This dispersion is proposed to occur due to low velocity serpentinised dipping outer rise normal faults within the subducting mantle lithosphere. Analysis of the P-wave coda from these events gives a new constraint on the degree of hydration of the mantle lithosphere at intermediate depths, and increases the amount of water estimated to be subducted by this relatively old cool slab by an order of magnitude. This chapter has been accepted for publication in the journal Geology (Garth & Rietbrock, 2014).

In Chapter 6 we present dispersive arrivals recorded in the forearc of Northern Japan from WBZ events at 150 – 220 km depth. Analysis of dispersion from a profile of events from different depths shows that the velocity contrast of the crustal waveguide reduces with depth. This is interpreted as the progressive dehydration of the subducted oceanic crust, and offers the first direct seismological evidence of metamorphic dehydration reactions other than the eclogite transformation. The analysis presented in this chapter suggests that the phase transformations occurring in the Japan subduction zone, including the lawsonite-eclogite transformation occur at greater depths than has previously been suggested. This chapter has been submitted to the Geophysical Journal International.

In Chapter 7 the methodology proposed and results presented are discussed. In particular the significance of these results to our understanding of earthquake processes at intermediate depths, and the amount of water delivered to the mantle are discussed. In this chapter potential areas of further work are also presented. In Chapter 8 the broad conclusions of this work are summarised.

Chapter 2

The Wadati-Benioff zone

Anomalously deep seismicity observed beneath volcanic arcs has long been associated with subducted oceanic material. Kiyoo Wadati first suggested that the plane of deep earthquakes observed beneath Japan may be evidence of *'continental displacement'* as proposed by Alfred Wegener's then highly controversial theory of continental drift (Wadati, 1935). Wadati-Benioff zone (WBZ) seismicity is still used as a primary tool for inferring the geometry of subducting slabs. The most recent and comprehensive example of this is the global slab model, *slab1.0* (Hayes *et al.,* 2010; 2012).

With increasing instrumentation it has become clear that two distinct layers of WBZ seismicity are seen in many subduction zones. This was first noted in Japan (Umino & Hasegawa, 1975; Hasegawa *et al.,* 1978) and has since been shown to be a common feature of subduction zones across the globe (e.g. Brudzinski *et al.,* 2007). The thickness of the WBZ, and hence the separation of the planes of seismicity has been shown to correlate well with the age of the plate (Brudzinski *et al.,* 2007).

How intermediate (60 – 300 km depth) and deep (> 300 km depth) seismicity occurs, where high temperatures and pressures are thought to inhibit brittle failure, is still not fully understood. The mechanisms proposed must be able to explain the occurrence of upper and lower plane WBZ seismicity in the wide range of temperature and pressure conditions found in subduction zones. There are three mechanisms that are considered as potentially viable explanations for intermediate and deep focus seismicity (e.g. Frohlich, 2006). These are,

1. *Dehydration embrittlement*
2. *Self-localised shear instabilities*
3. *Transformational faulting*

Dehydration embrittlement is proposed to cause intermediate depth seismicity as water from metamorphic dehydration reactions increases the pore fluid pressure allowing brittle failure to occur (e.g. Kirby *et al.,* 1996a; Hacker *et al.,* 2003a).

Self-localised shear instabilities are an alternative hypothesis that has been proposed to explain intermediate depth seismicity. This hypothesis does not require the production of fluids, and therefore can potentially occur in the absence of hydrous minerals (e.g. Keleman & Hirth, 2007). Seismicity is proposed to occur as shear instabilities increase the heat locally, reducing the viscosity and producing a self-localising feedback mechanism that allows brittle failure to occur (e.g. John *et al.,* 2009).

Transformational faulting has mainly been suggested as an explanation for deep focus earthquakes. It is proposed that at these depths seismicity occurs due to the phase change of olivine to modified spinel or wadsleyite (e.g. Kirby et al., 1996b; Stein & Stein, 1996). The phase change is proposed to occur in the transition zone in older, quickly subducting and therefore cooler slabs, where meta-stable olivine persists to greater depths. This theory potentially explains why deeper earthquakes are generally associated with subduction zones where cool lithosphere is subducting quickly (e.g. Frohlich, 2006).

As is discussed in the second part of this chapter (section 2.2), it has been widely shown that the occurrence of intermediate depth seismicity correlates well with the expected occurrence of hydrous mineral assemblages in the WBZ (e.g. Hacker *et al.,* 2003b). While transformational faulting and self-localised shear instabilities cannot be ruled out as a potential mechanism by which intermediate depth seismicity may occur, it is widely accepted that dehydration of hydrous minerals can account for the intermediate depth seismicity seen in subduction zones.

Hydrous mineral assemblages proposed to occur in the WBZ provide potential a mechanism for intermediate depth seismicity, a source of water causing mantle melting and arc volcanism, and an explanation for low velocity structures that are seen in the subducting slab. In the first part of this chapter the seismic observations suggesting that low velocity hydrous mineralogies may be present at depth will be discussed. In the second part we will discuss the thermal and petrological modelling methods used to estimate what mineral phases could explain the occurrence of WBZ seismicity, arc volcanism, and the observed low velocity structures.

2.1 Inferring and imaging low velocity structure in the WBZ

Global tomographic studies of the upper mantle show subduction zones as large scale high velocity features, due to the seismically fast cool lithospheric material sinking into the mantle (e.g. van der Hilst *et al.,* 1991). A number of studies however have suggested that

smaller scale low velocity features may be seen on top of subducting slabs (e.g. Helffrich & Abers, 1997). These low velocity structures have been inferred by a range of seismological techniques including the observation of subduction zone guided waves (e.g. Abers, 2000) and converted seismic phases (e.g. Matsubara *et al.,* 1986). With increasing network coverage in many subduction zones these low velocity features have also been imaged by receiver function techniques (e.g. Yuan *et al.,* 2000) and high resolution seismic tomographic studies (e.g. Zhang *et al.,* 2004). In this section these observations are briefly summarised.

2.1.1 Guided waves observations in subduction zones

Observations of dispersed P-wave arrivals (e.g. Abers, 2000), focusing of high frequency energy (e.g. Martin, *et al.,* 2003; Furumura & Kennett, 2005) and extended P-wave coda (Furumura & Kennett, 2005) have widely been attributed to the presence of a low velocity waveguide associated with WBZ events. Dispersed waveforms that have been attributed to these subduction zone waveguide structures have been observed across the globe. Guided wave dispersion occurs as high frequency, short wavelength seismic energy is retained and delayed in the low velocity oceanic crust, while low frequency longer wavelength energy travels in the faster surrounding material.

Generally guided wave dispersion is seen in the subduction zone forearc, where high frequency guided wave energy has decoupled due to the bend of the slab (Martin *et al.,* 2003). Non-decoupled guided wave arrivals have however also been seen at ocean bottom seismometers close to the trench in Northern Japan (Shito *et al.,* 2013).

Body wave dispersion associated with a low velocity waveguide has been observed at many subduction zone across the globe including Northern Japan (e.g. Abers 2000; 2005; Furumura & Kennett 2005), Alaska and the Aleutians (Abers & Sarker, 1996; Abers, 2005), Nicaragua (Abers, 2003), South America (e.g. Martin *et al.,* 2003; Martin & Rietbrock, 2006), the Hellenic arc (Essen *et al.,* 2009) and Southeast Japan (e.g. Hori *et al.,* 1985; Miyoshi *et al.,* 2012). This wide range of observations suggests that the low velocity structure is a common feature in many subduction zones. For dispersion to occur the source must be on or very near to the waveguide (Abers, 2005; Martin & Rietbrock, 2006), suggesting that these low velocity structures may be directly associated with the occurrence of intermediate depth seismicity.

Subduction Zone	Approximate slab dip	Velocity of LVL (km/s)	
		Inferred from GUIDED WAVES	Inferred from other methods
Central Andes	~16° [a]	~ 7.5 [a]	-
Cascadia	~21° [b]	-	-
Japan	~26° [c]	7.72 – 7.95 [e]	6.2 – 7.0 [f]
Alaska	~33° [b]	4.10 – 7.97 [e]	4.6 – 6.1 [g]
Nicaragua	~45° [d]	7.66 – 7.87 [e]	-

Table 2.1 – Comparison of LVL velocities and slab dip, from guided wave and other studies. Figures are taken from the following references, [a] Martin & Rietbrock (2006), [b] Rondenay *et al.* (2008), [c] Kawakatsu & Watada, (2007), [d] Mackenzie et al. (2010), [e] Abers, (2005), [f] Nakajima *et al.* (2009), [g] Ferris *et al.* (2003).

In most cases guided wave dispersion is attributed to a low velocity layer (LVL) of 2 – 8 km thickness that is 5 - 8 % slower than the surrounding material (e.g. Abers 2000; Martin *et al.,* 2003). The variation in waveguide velocity contrast seen in the Pacific subduction zones studied by Abers (2005) correlates well with the dip of the slab, with steeper subduction zones showing a greater velocity contrast. This data is shown in table 2.1, and is compared with velocities inferred from other seismic studies. It is proposed that this greater velocity contrast is due to released fluids being channelled up dip more effectively in steeper subduction zones (Abers, 2005). Abers (2005) also suggested that guided waves from events at greater than 150 km depth may see a smaller velocity contrast than events occurring above 150 km.

One notable exception is arrivals from intermediate depth events in the Tonga subduction zone which show a high frequency first arrival, and delayed low frequency arrivals (e.g. Gubbins & Snieder, 1991). It is proposed that this dispersion occurs due to a high velocity layer of eclogitized crust (Gubbins *et al.,* 1994). It is also possible that the long ray paths of the observed waveforms in this study means that deeper eclogitized slab structure is sampled, causing the high frequency early arrival.

The studies of low velocity subduction zone waveguides outlined above have used a range of approaches to measure and interpret the guided wave dispersion observed. The dispersive nature of guided wave arrivals is quantified by Abers (2000) and subsequent studies by using time frequency analysis. This clearly shows that low frequencies (< 2 Hz) arrive 1 - 2 seconds before the high frequency energy (2 – 8 Hz). This method has been

adopted by several later studies, and averaged dispersion curves have been used to quantify the low velocity waveguides in Pacific subduction zones (Abers, 2005).

Martin *et al.* (2003) also note that the high frequency component of the waveform is delayed, and that guided wave arrivals are associated with a characteristic high frequency peak when the signal is plotted in the frequency domain. Martin *et al.* (2003) use two-dimensional (2D) waveform simulations to show that a low velocity waveguide can explain the guided wave observations made in the South American subduction zone. The resulting waveforms are controlled not only by the velocity and width of the waveguide, but also by the source offset and slab geometry (Martin & Rietbrock 2006). Other works have since used 2D waveform simulations to show that these observations can be explained by energy escaping a low velocity waveguide (e.g. Essen *et al.,* 2009, Miyoshi *et al.,* 2012), and that guided wave energy can be seen by ocean bottom seismometer close to the trench (Shito *et al.,* 2013). The approximate ray paths of these guided wave phases in the slab are shown schematically in figure 2.1.

Furumura & Kennett (2005) show that a single LVL cannot alone account for the extended P-wave coda that is seen in the North of Japan. They use 2D waveform propagation models to explore the seismic structures that may lead to the extended P-wave coda, and conclude that random scatterers, elongated parallel to the slab can cause the extended P-wave coda seen where a LVL is also present.

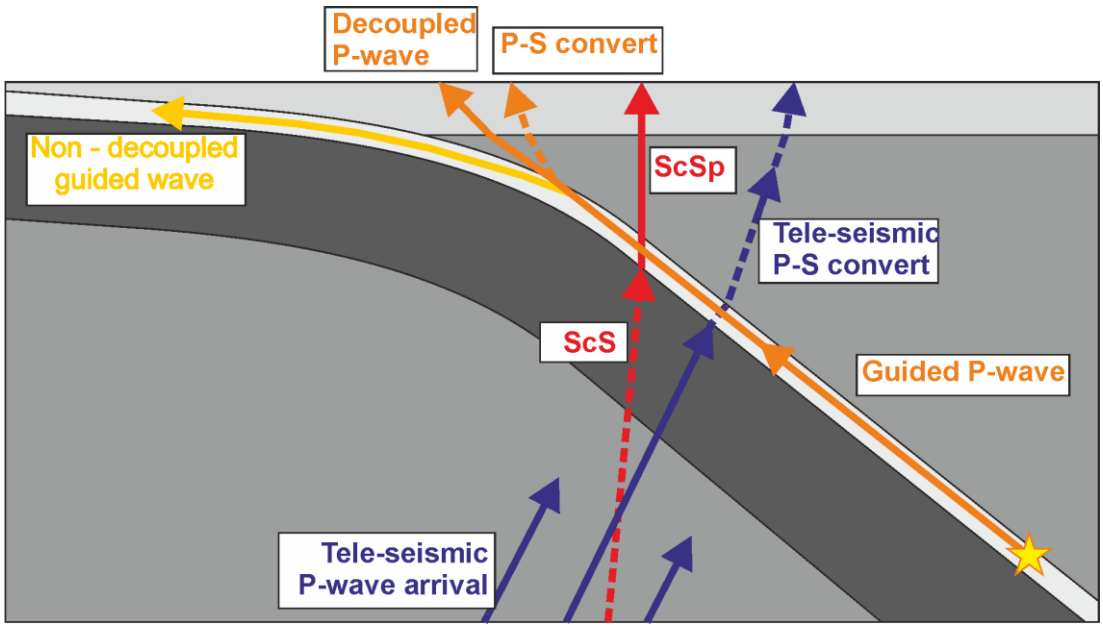

Figure 2.1 – Approximate ray path of guided and converted phases. The schematic figure clearly shows that guided wave phases spend longer interacting with the LVL than any other phase.

Subduction zone waveguide effects have also been investigated using three-dimensional (3D) waveform simulations (e.g. Shapiro *et al.,* 2000, Furumura & Kennett, 2005) but these models generally lack the resolution required to fully model waveguide effects at the required scale length.

2.1.2 Converted seismic phases in subduction zones

Converted seismic phases have been used to infer low velocity structures associated with the subducting slab. P-S conversions were first noted along the Fiji-Tonga trench by Mitronovas & Isacks (1971), who attributed the arrival to a sharp boundary at the top of the slab. Precursors to ScS arrival (ScSp) seen in Japan (Okada, 1971) and South America (Snoke *et al.,* 1977) are thought to occur due to an S-P conversion which is also attributed to a sharp velocity change at the top of the slab.

Matsuzawa *et al.* (1986) showed that P-S conversions in Northern Japan were explained well by a 6 % slow LVL with a thickness of 10 km or less, lying above a high velocity slab that is 6 % faster than the surrounding mantle material. Similar observations in the Eastern Aleutians have shown that P-S conversions here can be explained by a LVL that is approximately 8 % slower than the surrounding material (Helffrich & Abers, 1997).

Teleseismic P-S conversions observed at large temporary and permanent seismic networks have been used to image the velocity structure of subducting slabs at a variety of subduction zones. These receiver function studies can be used to image sharp velocity contrasts in the Earth, and are sensitive to relatively small scale low velocity structures in the subduction zone. The ray path of these converted phases is shown schematically in figure 2.1. In the central Andes receiver function studies using data from a range of dense temporary seismic networks have shown a sharp reflector associated with the intermediate depth seismicity, that is interpreted as a 5 - 10 km thick LVL with an S-wave velocity contrast of ~15 % (Yuan *et al.,* 2000). The conversion signal terminates at ~120 km depth and is interpreted as metastable non-eclogitised mafic crust that becomes fully eclogitised at 120 km depth, and hence is no longer seismically detectable. While much of the intermediate depth seismicity occurs within the LVL, Yuan *et al.* (2000) also note that some seismicity occurs 10 - 20 km below the LVL in the subducted oceanic mantle.

Low velocity structure interpreted to be subducted oceanic crust has also been imaged by receiver function analysis, utilising the dense permanent Hi-Net array in Northern Japan (Kawakatsu & Watada, 2007). Here the velocity decrease with depth, associated with

hydrous minerals in the subducting oceanic crust, persists to a depth of ~100 km, below which a velocity increase with depth is imaged. Kawakatsu & Watada (2007) postulate that as the low velocity oceanic crust becomes less hydrated, the released water forms a layer of low velocity serpentinite above the subducting slab. Therefore an increase in velocity is seen with increasing depth as the underlying oceanic crust has a higher velocity than the proposed layer of low velocity serpentinite. To date however no such structure has been proposed in other subduction zone settings.

Receiver function methods have however suggested the presence of low velocity subducted oceanic crust at a variety of other subduction zones including Alaska & Cascadia (e.g. Rondenay *et al.,* 2008). In general these studies show that the LVL is 5 - 10 km thick, with the exception of the Alaskan subduction zone which is thought to be much thicker possibly due to the subduction of the thicker oceanic crust associated with the subducting Yakutat terrain (Ferris *et al.,* 2003).

These studies show that the LVL persist to 100 - 120 km in most subduction zones, below which it is no longer seismically observable (in receiver function studies) presumably due to the onset of full eclogitization. The exception to this is the Cascadia subduction zone where the LVL is thought to terminate at ~40 km due to the high temperatures of the young subducting crust (Rondenay *et al.,* 2008). The depths to which receiver function methods resolve the oceanic LVL are persistently shallower than the depth to which guided wave studies infer low velocity structure to exist in the same subduction zones, as is summarised in table 2.2. It is also noted that some guided wave studies have suggested that the LVL may be less than the 5 km lower bound of thickness inferred for receiver function studies (e.g. Martin *et al.,* 2003).

2.1.3 High resolution seismic tomography

The increasing coverage of permanent and temporary seismic networks in various subduction zones has also meant that relatively small scale features such as a LVL in the slab can be resolved by tomographic techniques. Zhang *et al.* (2004) made use of the dense seismic network and the two clearly defined planes of seismicity in the Honshu region of Northern Japan to produce a high resolution seismic tomography of the subducting plate. The tomography was produced using a double difference approach that solves for both the absolute travel time and the differential travel time between the two planes of seismicity. This method gives particularly good resolution close to the seismic sources, and hence has been able to resolve new details of the velocity structure of the WBZ.

Subduction zone	Approximate age of subducting plate (Myr)	Depth extent of LVL (km)	
		from RECEVIER FUNCTION studies	from GUIDED WAVE studies
Cascadia	10	40[a]	-
Nicaragua	30	100[b]	150[e]
Alaska	50	120-130[a]	250[f]
Central Andes	60	120[c]	160 - 250[g]
Japan	150	100-120[d]	~250[f]

Table 2.2 – Depth of LVL inferred from different methods. Plate ages are based on Müller *et al.* (2008). Depths inferred from the following references [a] Rondenay *et al.* (2008); [b] Mackenzie *et al.* (2010); [c] Yuan *et al.* (2000); [d] Kawakatsu & Watada (2007); [e] Abers *et al.* (2003); [f] Abers (2005); [g] Martin *et al.* (2003).

Zhang *et al.* (2004) showed a reduced P-wave velocity associated with both the upper and lower planes of seismicity as well as a reduced S-wave velocity associated with the upper plane of seismicity. Similar observations have since been made in the Hokkaido region of Northern Japan using a travel time tomography with an exceptionally large data set (Nakajima *et al.,* 2009). This study also shows reduced P-wave and S-wave velocities in both the upper and lower seismic planes (Nakajima *et al.,* 2009).

Nakajima *et al.* (2009) interpret the lower plane low velocity anomalies as serpentinite or a chlorite bearing Harzburgite. Zhang *et al.* (2004) rule out serpentinite as they do not observe an S-wave velocity anomaly associated with the lower plane of seismicity, and instead propose that a forsterite-enstatite-H_20 formation may cause the reduced P-wave velocities observed. These two studies offer the first direct observations suggesting that hydrous mineral assemblages are present in the lower plane of seismicity. This suggests that dehydration embrittlement could potentially account for lower plane as well as upper plane WBZ seismicity.

Low velocity structure relating to the lower plane of seismicity has been imaged by tomographic studies in Northern Chile (Dorbath *et al.,* 2008) and Central America (Syracuse *et al.,* 2008), although both of these studies lack the resolution to determine if this low velocity structure forms a separate LVL, or is directly related to the lower plane of seismicity. The fact that double LVLs have only been seen in Japan is likely to be due to the excellent network coverage that is found there, as well as the clear separation of the planes of seismicity seen in this relatively old plate. It is therefore entirely possible that these

features may be present at other subduction zones where tomographic studies with the necessary resolution are not currently possible.

2.1.4 Observations of outer rise normal faulting

Outer rise normal faulting potentially has an important control on the hydration of subducting material. Several studies have suggested that the oceanic mantle may be hydrated by outer rise faults allowing lower plane WBZ earthquakes to occur by dehydration embrittlement (e.g. Peacock, 2001). It has also been suggested that this hydration could potentially transport large amounts of water to the mantle (e.g. van Keken *et al.,* 2011).

The surface expression of outer rise normal faulting is apparent in many subduction zones, where fault scarps are seen running roughly parallel to the trench. In Central America these outer rise faults have been imaged by seismic reflection to greater than 20 km depth (Ranero *et al.,* 2003). Tomographic inversion of reflected and refracted waves from this survey show that this outer rise faulting is also associated with a reduction in seismic velocity as the plate bends into the trench (Ranero *et al.,* 2004).

The onset of outer rise faulting has also been shown to correlate with a decrease in heat flow (Grevemeyer *et al.,* 2005), and magnetotelluric studies have shown an increase in conductivity close to the trench in Central America (Worzewski *et al.,* 2012). These observations are thought to represent the onset of hydration and serpentinisation of the oceanic mantle due to the normal faulting occurring at the outer rise.

These observations do not however constrain the depth to which the subducting plate is hydrated at the outer rise. Passive seismic tomography performed offshore Nicaragua shows that the maximum depth at which reduced velocities occur corresponds to the maximum depth at which normal faulting micro-earthquakes are detected (Lefeldt *et al.,* 2012), providing further evidence that hydration at the outer rise occurs due to normal faulting.

It should be noted that many of the studies directly quantifying the hydration of the oceanic mantle at the outer rise have been conducted at the Nicaraguan trench. Geochemical and seismic observations from the Nicaraguan arc have suggested that this subduction zone may be anomalously highly hydrated (e.g. Abers *et al.,* 2003). Therefore while the processes observed here may well apply to other subduction zones the overall hydration of the slab may be anomalously high.

In South and Central America it has been shown that focal mechanisms of outer rise earthquakes have a similar orientation with respect to the oceanic plate as intermediate depth events occurring within the WBZ (Ranero *et al.,* 2005). Ranero *et al.* (2005) therefore propose that outer rise normal faults may be reactivated at depth, accounting for much of the intermediate depth seismicity seen in these subduction zones.

The hypothesis that intermediate and deep focus earthquakes occur on pre-existing faults such as outer rise faults has been tested in several subduction zones using the methods of Warren & Silver (2006) to determine the fault plane of intermediate and deep earthquakes. Warren & Silver (2006) propose that the rupture orientation of intermediate and deep focus earthquakes can be determined by considering the length of the rupture at different stations, as the shortest rupture lengths will be seen where the ray path to the station is approximately parallel to the rupture direction.

Warren *et al.* (2008) confirm that in Central America events at depths between 35 and 85 km depth occur on reactivated outer rise normal faults. Studies using this method in the Tonga-Kermadec subduction zone (Warren *et al.,* 2007) and the Izu-Bonin-Marianas subduction zones (Myhill & Warren, 2012) conclude that pre-existing fault structures do not control the orientation of intermediate and deep fault planes. The relationship between outer rise faulting and intermediate depth seismicity is not fully understood, but appears to be a control on intermediate seismicity in some but not all subduction zones.

2.1.5 Summary of observations

Low velocity structures exist at intermediate depth in many subduction zones, and are widely interpreted as subducted oceanic crust. Earthquakes can occur both within the low velocity oceanic crust and several kilometres below it in the oceanic mantle. Low velocity structures persist to depths of 40 – 250 km depending on the subduction zone. At greater depths these structures are seismically indistinguishable which is interpreted as the onset of full eclogitization. There is however a discrepancy between the depth to which low velocity material is imaged by receiver function methods, and the depths to which it is inferred by guided wave studies, with subduction zone guided wave observations suggesting that the low velocity anomalies may persist to greater depth. Few studies quote the absolute velocity of the LVL, but the compilation of guided wave observations of Abers (2005) suggests that the velocity may correlate with slab dip.

Other low velocity structures have been inferred and imaged such as a layer of serpentinite above the slab (Kawakatsu & Watada, 2007), and a lower LVL associated with the lower plane of seismicity (Zhang *et al.,* 2004; Nakajima *et al.,* 2009). This imaged lower LVL provides an explanation of how intermediate depth seismicity may occur on the lower seismic plane through dehydration embrittlement. A widely proposed explanation of how this hydration of the mantle can occur to these depths is through normal faults that penetrate the oceanic mantle at the outer rise. The fault scarps of normal faults are apparent at the outer rise of many subduction zones and a range of observations have suggested that hydration of the incoming plate may occur here.

2.2 Modelling hydration of the WBZ

As direct observations of the WBZ are limited much of our understanding of processes occurring at these depths is informed by numerical simulations of conditions found during subduction. Thermal models have been used to calculate the temperature and pressure conditions expected in subducting plates at WBZ depths, and petrological modelling has been used to determine the metamorphic phases that may be stable at these conditions. In this section we discuss how various modelling methods have been used to simulate the hydration and dehydration of the subducting oceanic plate.

2.2.1 Hydration of the oceanic lithosphere

It is widely expected that the oceanic crust is hydrothermally altered as oceanic water convects through the crust as it cools, forming features such as black smokers (e.g. Fowler, 2005). This process can only conceivably hydrate the upper few kilometres of the lithosphere. Lower plane WBZ seismicity and associated velocity anomalies however have both been attributed to the presence of hydrous mineral assemblages up to 40 km below the top of the slab in the subducted oceanic mantle.

A number of mechanisms by which the oceanic mantle could be hydrated to these depths have been proposed, the most widely supported of which is that the oceanic mantle is hydrated by outer rise normal faults as the plate bends into the subduction zone (e.g. Peacock, 2001). Seismic reflection surveys have shown that outer rise normal faults penetrate to depths greater than 20 km (Ranero *et al.,* 2003), and the onset of hydration due to outer rise faulting has been inferred due to reductions in seismic velocity (e.g.

Ranero *et al.,* 2004), resistivity (e.g. Worzewski *et al.,* 2011) and heat flow (e.g. Grevemeyer *et al.,* 2005), as summarised in part 2.1.

Numerical simulations of how water interacts with the subducting slab have shown that normal faults forming at the outer rise as the plate bends can act as a fluid pathway, allowing hydration of the subducting oceanic mantle (Faccenda *et al.,* 2009). As the plate unbends a downward pressure gradient on the fault zone forces fluids to greater depths (Faccenda *et al.,* 2012). This mechanism suggests that hydrated mineral assemblages may form along fault zone fluid pathways in the subducting oceanic mantle.

These simulations also show that the water transported along these fault zone fluid pathways may form a hydrated layer within the oceanic mantle, as well as a hydrated layer at the top of the slab (Faccenda *et al.,* 2012). This double hydrated zone has a similar separation to the double seismic zones of older subducting plates. It is also noted that these double hydrated zones bear a striking resemblance to the double low velocity zones seen in high resolution tomographies of Northern Japan (e.g. Zhang *et al.,* 2004; Nakajima *et al.,* 2009). Faccenda *et al.* (2012) propose that the two modelled hydrated zones can account for the two layers of WBZ seismicity seen in many subduction zones, and suggest that the lower layer of WBZ seismicity occurs due to hydro-fracturing as buoyant fluids in the lower hydrated zone percolate up dip. This contrasts with the widely proposed view that lower plane seismicity can be explained by the breakdown of hydrous mineral assemblages in the subducting oceanic mantle (e.g. Peacock, 2001). It has however also been suggested that the breakdown of hydrous minerals formed by outer rise fault hydration can explain the variation in separation of the two planes of WBZ seismicity (e.g. Iyer *et al.,* 2012).

2.2.2 Dehydration of the subducting slab

The breakdown of hydrous minerals is widely proposed as a potential cause of intermediate and deep focus seismicity, and a potential source of fluids that induce melting in the mantle wedge, causing arc volcanism. The presence of hydrous minerals has also been widely suggested as an explanation for the occurrence of low velocity anomalies in the subducting plate. A wide range of studies have therefore investigated whether the presence and breakdown of hydrous mineralogies in the WBZ can explain these features. The methods developed have also been used to quantify the amount of water that is recycled to the mantle through subduction, allowing the role of subduction in the global water cycle to be better understood.

Hydrous mineralogies and intermediate depth seismicity

The three main hypotheses of how intermediate depth seismicity can occur at subduction zones are outlined at the start of this chapter. The most widely proposed and supported of these theories is that intermediate depth seismicity occurs due to dehydration embrittlement, where the breakdown of hydrous mineral assemblages allows brittle failure to occur. This would suggest that hydrous mineral assemblages would be expected to be present, and undergoing dehydration reactions at the depths at which seismicity occurs. Thermal and petrological modelling to determine where hydrous minerals may occur in the subduction zone has therefore been a key tool in assessing the viability of intermediate depth seismicity occurring through dehydration embrittlement.

It is widely proposed that upper plane WBZ seismicity occurs due to the dehydration of meta-basalt (and meta-gabbros) as they transform to eclogite (e.g. Kirby *et al.,* 1996a). It has also been shown that the lower plane of seismicity can be explained by the breakdown of serpentine formed in the subducting oceanic mantle by hydration due to outer rise faulting (Peacock, 2001). Yamasaki and Seno (2003) showed that the dehydration of antigorite and mid-ocean ridge basalt (MORB) can potentially explain the variation in thickness of the WBZ in several pacific subduction zones.

Hacker *et al.* (2003a) considered a suite of compositions found in the subduction oceanic plate, and produced pressure-temperature (P-T) plots for crustal compositions (e.g. MORB), as well as compositions found in the oceanic mantle such as depleted and un-depleted lherzolite, harzburgite and serpentinite. Using this data set Hacker *et al.* (2003b) calculated the occurrence of hydrous mineral assemblages in Pacific subduction zones and showed that intermediate depth seismicity correlates well with where hydrous mineral assemblages are expected to occur in the subducting slabs. Coupled with the seismic observations of low velocity minerals in the subducting slab, this provides strong evidence that intermediate depth seismicity occurs in the presence of hydrous mineral assemblages. It is therefore likely that intermediate depth seismicity in subduction zone occurs due to dehydration embrittlement.

Seismicity on hot and cold subduction zones may be controlled by the breakdown of different minerals. For instance van Keken *et al.* (2012) suggest that beneath Northern Japan the depth of upper plane seismicity below the surface of the subducted slab is controlled by the transformation of blueschist to hydrous eclogite. Abers *et al.* (2013) suggest that in cool subduction zones dehydration occurs due to the lawsonite-eclogite

transition, while in hot subduction zones dehydration occurs due to the zoisite-eclogite transition. Lawsonite breakdown is associated with a net volume increase, while zoisite breakdown is associated with a net volume decrease meaning there is no increase in pore fluid pressure. Therefore zoisite breakdown may not cause seismicity in the crust. Serpentinite breakdown is thought to control seismicity in the subducted oceanic mantle in both settings. This is proposed as an explanation for the observations of Abers *et al.* (2013), who compile high resolution seismic images and accurate earthquake locations to show that intermediate depth seismicity occurs within the oceanic crust in old subduction zones, and beneath it in young subduction zones.

Low velocity mineral assemblages

The wide range of seismic observations of low velocity structure associated with the subducting slab outlined in section 4.1 gives further evidence that there may be hydrous mineral assemblages present at depth in subduction zones. In order to properly interpret the low velocity anomalies that are observed it is important to understand the seismic properties of the candidate mineralogies that can be expected at the depths (e.g. Helffrich, 1996). A number of hypotheses have been proposed to explain the observed low velocity anomalies.

1. The presence of meta-stable gabbro has been considered by several studies. This hypothesis is however widely rejected as the persistence of gabbro would require almost completely anhydrous conditions during subduction, and the predicted velocity contrast for anhydrous gabbro is higher than is observed (e.g. Abers 2005, Connolly & Kerrick 2002).

2. A layer of serpentinised mantle material above the slab has been proposed to explain receiver function images in Northern Japan (e.g. Kawakatsu & Watada, 2007), but is not considered a viable explanation for LVLs imaged by receiver functions in other subduction zones (e.g. Rondenay *et al.,* 2008). Observations of guided waves resulting from LVL structure in subducting slabs do not favour this hypothesis either, as for guided wave dispersion to be seen the source must be on or near to the low velocity waveguide (e.g. Abers, 2005; Martin & Rietbrock, 2006) and it is unlikely that strain would localise within a layer of serpentinite. Serpentinisation is also unlikely to occur homogeneously, and therefore a serpentinised layer of mantle material is unlikely to be an effective waveguide (Abers, 2005). A recent compilation of well-located hypocentres and high resolution

images has also show that intermediate depth earthquake sources occur in the subducting oceanic crust in cool slabs, or below the moho in warmer slabs (Abers *et al.,* 2013). This also suggests that guided wave energy is unlikely to be excited in a LVL above the slab.

3. It has also been suggested that free fluid phases occurring within the slab at intermediate depths may cause the observed velocity decrease. It is however noted that this would require a larger amount of fluids than is expected to occur in the subduction setting (e.g. Abers, 2005).

4. By far the most widely accepted hypothesis to explain the low velocity slab structures is that hydrated phases within the subducted mafic crust persist to depths of 100 – 250 km depending on the subduction conditions (e.g. Connolly & Kerrick, 2002; Hacker *et al.,* 2003b). This hypothesis is discussed in further detail below.

Connolly & Kerrick (2002) note that lawsonite *"has a profound effect on seismic velocities".* Phase diagrams of altered (and un-altered) MORB compositions calculated by free energy minimization show that lawsonite persists to high temperatures (> 700^{o}c at 7.5 GPa) and extremely high pressures (> 9 GPa), and therefore may account for the low velocities seen in the slab at these conditions (Connolly & Kerrick, 2002).

Hacker *et al.* (2003a) perform similar calculations for the bulk compositions of the oceanic crust (e.g. MORB) and mantle (e.g. harzburgite, lherzolite and serpentinite). The predicted velocity of the mineral phases present at intermediate depths are then calculated, showing that low velocity hydrous minerals are expected to occur in the WBZ at a range of subduction conditions (Hacker *et al.,* 2003b). The termination of the LVL is then proposed to correspond to the breakdown of lawsonite. Connolly & Kerrick (2002) propose this is due to the lawsonite-stishovite transition in cool subduction zones, and due to the lawsonite-coesite transition in warmer subduction zones. Hacker *et al.* (2003a & b) however suggest that the termination of the LVL corresponds to the lawsonite-eclogite transition.

These slightly different interpretations may be due to small differences between the altered MORB compositions used by the two studies, but are more likely to be due to the different P-T paths the two studies infer. Connolly & Kerrick (2002) extrapolate the P-T path of Peacock and Wang (1999) for hot and cool subduction conditions, which gives a very high pressure P-T trajectory. Hacker *et al.* (2003b) calculate the thermal models for individual

subduction zones using the methods of Peacock (1990), and suggest a less steep P-T path even for cool subduction zones.

Thermal modelling suggests that the breakdown of lawsonite to eclogite controls the termination of the LVL in warmer subduction zones (e.g. Hacker *et al.,* 2008), and this phase transformation has been shown to correlate well with observations in Cascadia and Alaska (Rondenay *et al.,* 2008). However the termination of the LVL due to other transitions identified by Connolly and Kerrick (2002) cannot be ruled out, especially for cooler subduction settings.

Water delivered to the Earth's mantle

The Earth's oceans are thought to have originally been derived from the juvenile hydrated mantle (e.g. Rüpke *et al.,* 2006). At subduction zones oceanic water contained in hydrous mineral assemblages is returned to the mantle. The water transported to the mantle during subduction is likely to play a major role in the global water cycle, and it is therefore important to understand how much water is transported in subducted hydrous mineral assemblages. The thermal and petrological methods that have been used to determine if intermediate depth seismicity occurs through dehydration embrittlement, and if low velocity anomalies can be explained by hydrous mineral assemblages, can also be used to address the amount of water that is transported during subduction.

Arguably the most complete study of this kind is that of van Keken *et al.* (2011) who take the metamorphic relationships derived by Hacker (2008), and the global compilation of slab thermal models of Syracuse *et al.* (2010) to produce a detailed estimate of the amount of water transported to the mantle at subduction zones globally. Van Keken *et al.* (2011) calculate the water content of oceanic sediments and estimate that the 7×10^8 Tg/Myr of oceanic water is subducted by the oceanic crust. Approximately 10 % of this water is carried in the sediments, and so is likely to be lost at shallow depths (van Keken *et al.,* 2011). The remaining 90 % is carried in crustal basalt and gabbro, and is lost at a range of intermediate depths depending on the thermal conditions of the subduction zone. Overall van Keken *et al.* (2011) propose that ~69 % of water subducted globally by the oceanic crust is lost to the oceanic mantle at depths of less than 230 km, with ~31 % being transported to the deeper mantle. Hydrated crustal rocks break down at shallower depths in hot subduction zone than in cool subduction zones, so water is thought to be transported to greater depth in cooler subduction conditions (van Keken *et al.,* 2011).

In this study van Keken *et al.* (2011) simply approximate the hydration of the subducting oceanic mantle as a 2 km thick layer of serpentinised mantle material that is 2 wt% hydrated, reflecting the large amount of uncertainty that exists in the overall hydration of the subducting oceanic mantle. Van Keken *et al.* (2011) also quote the H_2O flux assuming a fully serpentinised slab mantle, and an un-serpentinised slab mantle highlighting the important role of slab mantle hydration in the global water cycle.

It is proposed that the lithospheric mantle can carry large amounts of water to the deep mantle (e.g. Rüpke *et al.,* 2004; Iyer *et al.,* 2012), and the lack of observational constraint on this hydration is the largest source of error in current models of the global water cycle (e.g. van Keken *et al.,* 2011). Subducting mantle hydration may be particularly important for understanding the amount of water transported to the deep mantle, as it has been suggested that up to 40 % of slab mantle hydration may be delivered to the deep mantle in cool slabs, by high pressure hydro-silicates such as phase-A serpentinite (Rüpke *et al.,* 2004).

The hydration of the lithospheric mantle therefore dominates the water delivered to the deep mantle. Rüpke *et al.* (2004) consider the amount of water subducted by the oceanic mantle, as well as the crust and sediments to calculate the amount of water delivered to the mantle over the age of the Earth, concluding that present day mantle hydration is dominated by recycled oceanic water rather than residual juvenile hydration.

It is not fully understood if water can be delivered to the transition zone through a continuous chain of hydrous silicates. It has however been suggested that not all water released from dehydration reactions is released to the mantle, but some water may be transported to deeper within the slab due to downward pressure gradients on normal faults penetrating the lithospheric mantle (Faccenda *et al.,* 2012). This water may then be transported to the transition zone regardless of the stability of hydro silicates.

Iyer *et al.* (2012) use a reactive flow model to estimate the hydration of the oceanic mantle at subduction zones with a variety of subduction parameters, and benchmark these estimates to observations of hydration at the outer rise in South and Central America. They show that the oceanic mantle is likely to be highly hydrated, and therefore able to transport large amounts of water to the mantle, especially in cooler subduction zones. The amount of water that is estimated to be delivered to the deep mantle by various studies is summarised in table 2.3.

Reference	Young Subduction Zone (e.g. Central Chile)		Old Subduction Zone (e.g. Hokkaido trench)	
	At the trench	Subducted beyond ~ 230 km depth	At the trench	Subducted beyond ~ 230 km depth
Rüpke *et al.* (2004)	-	24	-	36
van Keken *et al.* (2011)				
- No serpentinisation	20.6	0.4	21.5	9.5
- 2 wt% serpentinisation	30.1	0.4	31.1	19.2
- Full serpentinisation	63.8	0.4	65.5	21
Iyer *et al.* (2012)	36 - 135	-	64 - 200	-

Table 2.3 – Comparison of estimates of mineral bound H_2O is the subducting plate. Amounts subducted quoted in Tg/Myr/m of arc. Estimates from Rüpke *et al.* (2004) assume plate subducting at 6 cm/yr. Otherwise plate age and rate of subduction is based on van Keken *et al.* (2011).

2.3 Summary

Low velocity structures imaged by a range of seismic techniques can be explained by hydrous mineral assemblages that occur at the temperature and pressure conditions found during subduction. The upper LVL is thought to consist of meta-stable basaltic material, with the identifiable low velocity phases correlating roughly with the persistence of lawsonite (Connolly & Kerrick, 2002; Hacker *et al.,* 2003a & b).

The patterns of intermediate depth seismicity seen in Pacific subduction zones correlates well with the predicted occurrence of hydrous mineralogies (e.g. Hacker *et al.,* 2003b). This strongly supports the hypothesis that dehydration embrittlement is the dominant mechanism by which intermediate depth seismicity occurs.

The lower LVL structure associated with the lower plane of seismicity (e.g. Zhang *et al.,* 2004) may well correspond to hydration at depth. Simulations of fluid flow during subduction have shown that hydration of the plate at the outer rise, coupled with the bending and unbending stresses of the plate can give rise to double hydrated zones in the subducting plate (Faccenda *et al.,* 2012). These double hydrated zones could explain the reduced velocities associated with the upper and lower planes of seismicity.

The low velocity minerals associated with WBZ seismicity and reduced seismic velocities in the slab also have the potential to transport large amounts of water to the mantle. Thermal petrological models (e.g. van Keken *et al.,* 2011) have given a good approximation of water transported by the upper slab, and it is proposed that the hydrated subducting oceanic mantle transports large amounts of water especially to the deep mantle (Rüpke *et al.,* 2004). The lithospheric mantle is widely thought to be highly hydrated due to outer rise faulting, though the degree of hydration is poorly constrained. This is a major source of uncertainty in current estimates of the total H_2O flux to the mantle (e.g. van Keken *et al.,* 2011).

Finally we highlight three main features of the WBZ that are not fully understood.

1. Thermal petrological modelling (e.g. Peacock *et al.,* 2001) and fluid flow modelling (e.g. Faccenda *et al.,* 2012) suggest that the lower plane of seismicity may occur due to the presence of fluids introduced at these depths by outer rise faulting. There is however currently no observation evidence that these outer rise normal faults occur at intermediate depths.
2. Hydration of the subducting lithospheric mantle due to these outer rise normal faults may also be responsible for a large amount of the water that is delivered to the mantle, and especially the deep mantle. There are however currently no observational constraints on the degree of hydration of the lithospheric mantle at intermediate depths.
3. Though it is widely proposed that the termination of the LVL correlates with the onset of full eclogitization (e.g. Rondenay *et al.,* 2008) the depth at which is inferred to occur by receiver function methods differs from the depths inferred from guided wave studies. There also little seismic evidence of the velocity changes associated with other phase changes in the subducting slab.

In this thesis detailed analysis of arrivals from WBZ events is able to put new observational constraints on the velocity structures seen in the WBZ. This allows new inferences on the mineralogies associated with WBZ seismicity that deliver water to the deep mantle to be made.

Part one

Modelling and Measuring Subduction Zone Guided Wave Dispersion

Chapter 3

Waveform Modelling Using the Finite Difference Method

In this thesis numerical models are used to simulate dispersed and scattered P-wave arrivals from Wadati-Benioff zone events, which are observed globally in subduction zone forearcs. Synthetic waveforms are produced using the finite difference (FD) method to simulate both elastic and visco-elastic properties of the subduction zone structure. Modelling is carried out with two and three dimensional (2D and 3D) models using the staggered grid FD method implemented in sofi2D and sofi3D (Bohlen, 2002).

In this chapter the formulation of the FD method is described, with particular emphasis on the methods that are relevant to this study. Firstly the elastic case is considered, before introducing the formulation of the visco-elastic case. The formulation of the free surface, and absorbing boundary conditions used are then summarised. The source implementation and stability criteria of the method are then described. The specific model setup and variables used are described in Chapter 4.

3.1 The Elastic Case

The FD technique used in this study follows the method of Virieux (1986), who applied a FD scheme developed to simulate crack propagation (Madariaga, 1976) to model P-SV waves in an elastic medium. Rather than solving for the wave equation, Virieux (1986) used the constituent equations, the equation of motion and Hooke's law, to give a first order FD description of the system. The velocity-stress scheme proposed by Virieux (1986) can be expressed for the 2D elastic case by the following set of partial differential equations. The terms used in the formula below are summarised, along with all other variables introduced at the end of the chapter in table 3.1.

$$\frac{\partial v_x}{\partial t} = \frac{1}{\rho}\left(\frac{\partial \sigma_{xx}}{\partial x} + \frac{\partial \sigma_{xz}}{\partial z}\right)$$

$$\frac{\partial v_z}{\partial t} = \frac{1}{\rho}\left(\frac{\partial \sigma_{xz}}{\partial x} + \frac{\partial \sigma_{zz}}{\partial z}\right)$$

$$\frac{\partial \sigma_{xx}}{\partial t} = (\lambda + 2\mu)\frac{\partial v_x}{\partial x} + \lambda\frac{\partial v_z}{\partial z} \tag{3.1}$$

$$\frac{\partial \sigma_{zz}}{\partial t} = (\lambda + 2\mu)\frac{\partial v_z}{\partial z} + \lambda\frac{\partial v_x}{\partial x}$$

$$\frac{\partial \sigma_{xz}}{\partial t} = \mu\left(\frac{\partial v_x}{\partial z} + \frac{\partial v_z}{\partial x}\right)$$

The velocity-stress scheme introduced by Virieux (1986) was implemented using second-order Taylor coefficients on a staggered grid. This method was modified for a fourth-order staggered grid by Lavander *et al.* (1988). The fourth-order staggered grid means that a given wavelength is in effect sampled twice as many times, and therefore a coarser grid spacing can be used for a given resolution frequency. The geometry of the 2D fourth-order staggered grid for the velocity-stress scheme described by Lavander *et al.* (1988) is summarised in figure 3.1a. In this project a fourth-order staggered grid is used in all model setups. In order to model wave propagation in 3D using a FD scheme the velocity and stress in the y-direction must be introduced. The velocity-stress FD scheme for the 3D case is shown below following Graves (1996).

$$\frac{\partial v_x}{\partial t} = \frac{1}{\rho}\left(\frac{\partial \sigma_{xx}}{\partial x} + \frac{\partial \sigma_{xy}}{\partial y} + \frac{\partial \sigma_{xz}}{\partial z}\right)$$

$$\frac{\partial v_y}{\partial t} = \frac{1}{\rho}\left(\frac{\partial \sigma_{xy}}{\partial x} + \frac{\partial \sigma_{yy}}{\partial y} + \frac{\partial \sigma_{yz}}{\partial z}\right)$$

$$\frac{\partial v_z}{\partial t} = \frac{1}{\rho}\left(\frac{\partial \sigma_{xz}}{\partial x} + \frac{\partial \sigma_{yz}}{\partial y} + \frac{\partial \sigma_{zz}}{\partial z}\right)$$

$$\frac{\partial \sigma_{xx}}{\partial t} = (\lambda + 2\mu)\frac{\partial v_x}{\partial x} + \lambda\left(\frac{\partial v_y}{\partial y} + \frac{\partial v_z}{\partial z}\right)$$

$$\frac{\partial \sigma_{yy}}{\partial t} = (\lambda + 2\mu)\frac{\partial v_y}{\partial y} + \lambda\left(\frac{\partial v_x}{\partial x} + \frac{\partial v_z}{\partial z}\right) \tag{3.2}$$

$$\frac{\partial \sigma_{zz}}{\partial t} = (\lambda + 2\mu)\frac{\partial v_z}{\partial z} + \lambda\left(\frac{\partial v_x}{\partial x} + \frac{\partial v_y}{\partial y}\right)$$

$$\frac{\partial \sigma_{xy}}{\partial t} = \mu\left(\frac{\partial v_z}{\partial y} + \frac{\partial v_y}{\partial x}\right)$$

$$\frac{\partial \sigma_{xz}}{\partial t} = \mu\left(\frac{\partial v_x}{\partial z} + \frac{\partial v_x}{\partial x}\right)$$

$$\frac{\partial \sigma_{yz}}{\partial t} = \mu\left(\frac{\partial v_y}{\partial x} + \frac{\partial v_z}{\partial y}\right)$$

3.2 The Visco-Elastic Case

While the elastic case is useful for modelling the velocity structure we know that the Earth does not deform entirely elastically, and that some seismic wave energy is taken up through viscous deformation. This is potentially important in subduction zones where the seismic quality factor Q can vary from as little as 30 in the mantle wedge compared to 1000 in the cool subducting lithosphere (e.g. Tsumura *et al.*, 2000; Rychert *et al.,* 2008).

The viscous deformation is introduced to the FD model by considering a series of Maxwell bodies, or dashpots, as shown in figure 3.2. This approach introduced by Emmerich & Korn (1987) takes L parallel Maxwell bodies (η_L) in series with a spring (k_L) to describe the viscous rheology. The elastic rheology is described by a single spring (k_0) in parallel with the Maxwell bodies, giving a visco-elastic body that is described as a generalised standard linear solid (GSLS) (Emmerich & Korn, 1987; Bohlen, 2002). From these bodies we can then define the stress relaxation time ($\tau_{\sigma l}$) and the strain relaxation time ($\tau_{\varepsilon l}$) following Bohlen (2002),

$$\tau_{\sigma l} = \frac{\eta_l}{\kappa_l}, \quad \& \quad \tau_{\varepsilon l} = \frac{\eta_l}{\kappa_0} + \frac{\eta_l}{\kappa_l} \tag{3.3}$$

Q is constant over the frequency range of seismic waves that are considered in this study, but a single Maxwell body does not give a Q that is constant in the frequency domain. A series of Maxwell bodies can however be used to approximate a constant Q in the frequency domain of interest. The frequency dependent seismic quality factor of a GSLS is given by the following equation (Emmerich & Korn, 1987; Blanch *et al.,* 1995; Bohlen, 2002),

$$Q(\omega, \tau_{\sigma l}, \tau) = \frac{\left(1 + \sum_{l=1}^{L} \frac{\omega^2 \tau_{\sigma l}^2}{1 + \omega^2 \tau_{\sigma l}} \tau\right)}{\left(\sum_{l=1}^{L} \frac{\omega \tau_{\sigma l}}{1 + \omega^2 \tau_{\sigma l}^2} \tau\right)} \tag{3.4}$$

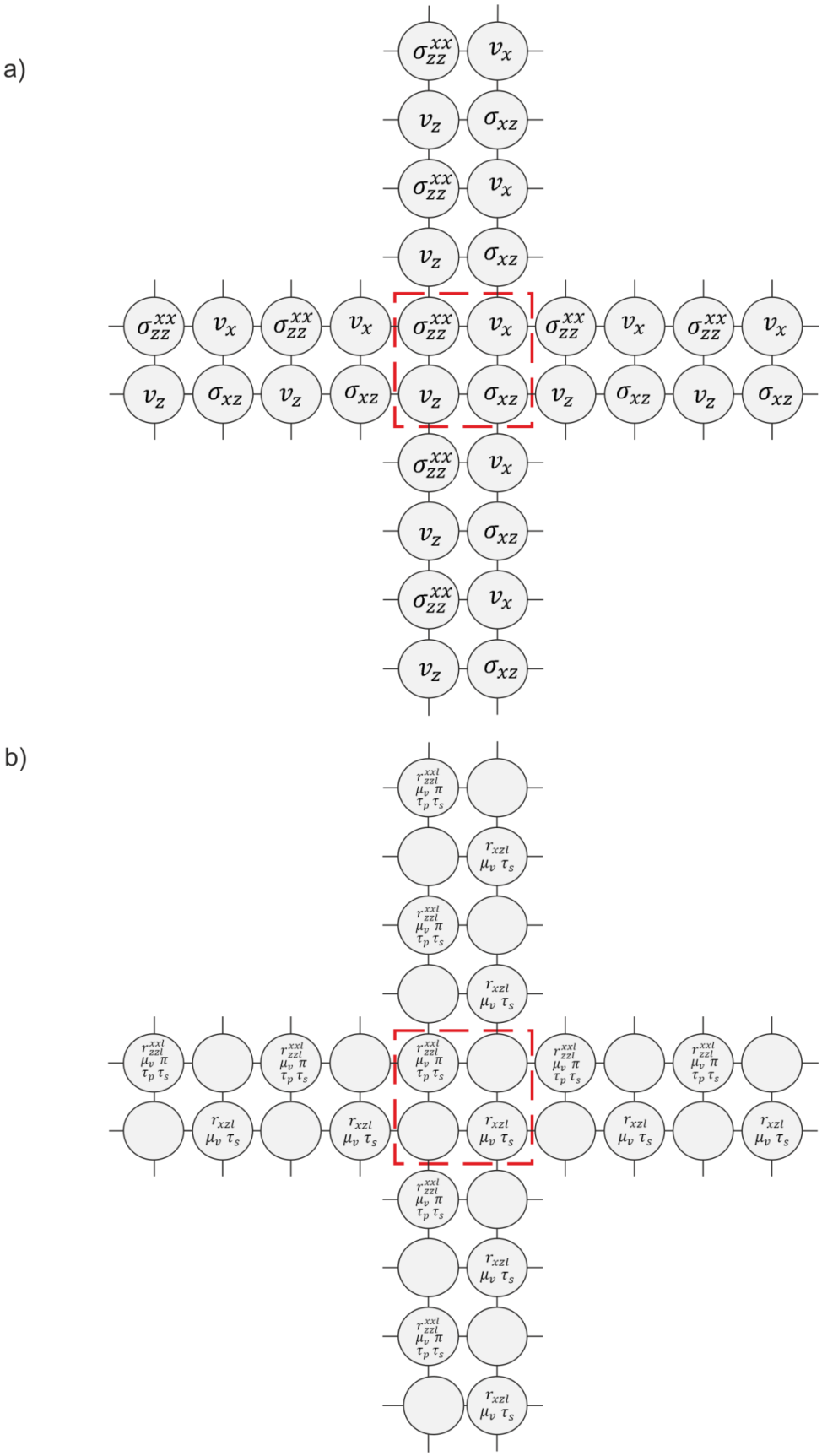

Figure 3.1 – Staggered grid for 2D FD scheme. a) The elastic variable distributed on the grid. b) The viscoelastic variables distributed on the staggered grid.

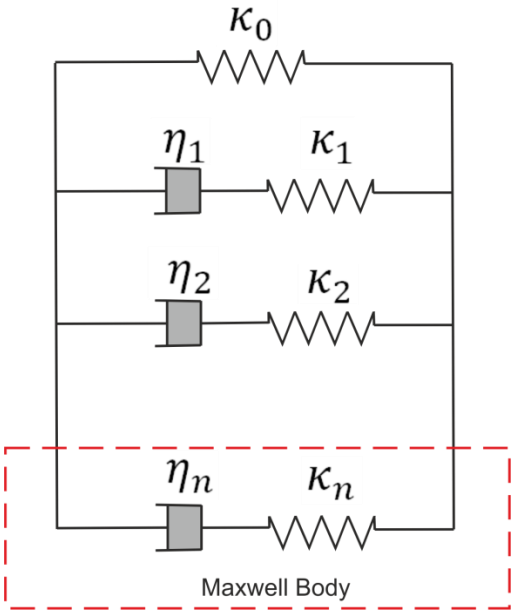

Figure 3.2 – Approximation of a visco-elastic body using L Maxwell bodies. Modified from Emmerich & Korn, (1987) and Bohlen, (2002).

where τ is defined following Blanch *et al.* (1995) as,

$$\tau = \frac{\tau_{\varepsilon l}}{\tau_{\sigma l}} - 1 \tag{3.5}$$

The variable τ was introduced by Blanch *et al.* (1995) to reduce the amount of memory required as well as the number of calculations needed to simulate a Maxwell body. Varying the value τ allows a given value of Q to be determined, while the frequency range for which Q is approximated is controlled by the stress relaxation times ($\tau_{\sigma l}$) (Blanch *et al.,* 1995). In a medium where the P-wave and S-wave quality factor Q_p and Q_s respectively are different, τ is defined for both P and S waves. The stress relaxation time is however the same for both Q_p and Q_s. Therefore the visco-elastic properties of a given medium can be described by the parameters τ_p, τ_s and $\tau_{\varepsilon l}$, where,

$$\tau^p = \frac{\tau_{\varepsilon l}^p}{\tau_{\sigma l}} - 1$$

$$\tau^s = \frac{\tau_{\varepsilon l}^s}{\tau_{\sigma l}} - 1 \tag{3.6}$$

In order to model the response of these viscous bodies in the FD model, we must incorporate these variables into the FD scheme. This is done by introducing the variables π and μ_v, which are the relaxation moduli for P-waves and S-waves respectively. The variable

π is analogous to the term $(\lambda + 2\mu)$ in the elastic case, while μ_v is analogous to the Láme parameter μ. The values of π and μ_v are defined below following Bohlen (2002).

$$\pi = v_{po}^2 \rho \, \mathcal{R}e^2 \left(\sqrt{\frac{1}{1 + \sum_{l=1}^{L} \frac{i\omega_0 \tau_{\sigma l}}{1 + i\omega_0 \tau_{\sigma l}} \tau^p}} \right) \tag{3.7}$$

$$\mu_v = v_{so}^2 \rho \, \mathcal{R}e^2 \left(\sqrt{\frac{1}{1 + \sum_{l=1}^{L} \frac{i\omega_0 \tau_{\sigma l}}{1 + i\omega_0 \tau_{\sigma l}} \tau^s}} \right) \tag{3.8}$$

Where $\mathcal{R}e$ is the real part of the expression, ω_0 is the centre frequency of the model domain, and v_{po} and v_{so} are the P and S wave velocities at this frequency respectively (Bohlen, 2002). These variables are then incorporated into the 2D FD scheme following Robertsson *et al.* (1994) as shown below. The velocity terms remain the same as in the elastic case (equation 3.1), but the stress variables are modified. The memory variables r_{xx} , r_{zz} and r_{xz} are also introduced and correspond to the stress variables σ_{xx}, σ_{zz} and σ_{xz} respectively. The distribution of the extra variables considered in the 2D visco-elastic case is shown in figure 3.1b.

$$\frac{\partial v_x}{\partial t} = \frac{1}{\rho} \left(\frac{\partial \sigma_{xx}}{\partial x} + \frac{\partial \sigma_{xz}}{\partial z} \right)$$

$$\frac{\partial v_z}{\partial t} = \frac{1}{\rho} \left(\frac{\partial \sigma_{xz}}{\partial x} + \frac{\partial \sigma_{zz}}{\partial z} \right)$$

$$\frac{\partial \sigma_{xx}}{\partial t} = \pi \frac{\tau_{\varepsilon l}^p}{\tau_{\sigma l}} \left(\frac{\partial v_x}{\partial x} + \frac{\partial v_z}{\partial z} \right) - 2\mu_v \frac{\tau_{\varepsilon l}^s}{\tau_{\sigma l}} \frac{\partial v_z}{\partial z} + r_{xx}$$

$$\frac{\partial \sigma_{zz}}{\partial t} = \pi \frac{\tau_{\varepsilon l}^p}{\tau_{\sigma l}} \left(\frac{\partial v_x}{\partial z} + \frac{\partial v_z}{\partial x} \right) - 2\mu_v \frac{\tau_{\varepsilon l}^s}{\tau_{\sigma l}} \frac{\partial v_x}{\partial x} + r_{zz} \tag{3.9}$$

$$\frac{\partial \sigma_{xz}}{\partial t} = \mu_v \frac{\tau_{\varepsilon l}^s}{\tau_{\sigma l}} \left(\frac{\partial v_x}{\partial x} + \frac{\partial v_z}{\partial z} \right) + r_{xz}$$

$$\frac{\partial r_{xx}}{\partial t} = -\frac{1}{\tau_{\sigma l}}\left(r_{xx} + \pi\left(\frac{\tau_{\varepsilon l}^{p}}{\tau_{\sigma l}} - 1\right)\left(\frac{\partial v_x}{\partial x} + \frac{\partial v_z}{\partial z}\right) - 2\mu_v\left(\frac{\tau_{\varepsilon l}^{s}}{\tau_{\sigma l}} - 1\right)\frac{\partial v_y}{y}\right)$$

$$\frac{\partial r_{zz}}{\partial t} = -\frac{1}{\tau_{\sigma l}}\left(r_{zz} + \mu_v\left(\frac{\tau_{\varepsilon l}^{p}}{\tau_{\sigma l}} - 1\right)\left(\frac{\partial v_x}{\partial x} + \frac{\partial v_z}{\partial z}\right) - 2\mu_v\left(\frac{\tau_{\varepsilon l}^{s}}{\tau_{\sigma l}} - 1\right)\frac{\partial v_x}{x}\right)$$

$$\frac{\partial r_{xz}}{\partial t} = -\frac{1}{\tau_{\sigma l}}\left(r_{xz} + \mu_v\left(\frac{\tau_{\varepsilon l}^{s}}{\tau_{\sigma l}} - 1\right)\left(\frac{\partial v_x}{\partial z} + \frac{\partial v_z}{\partial x}\right)\right)$$

3.3 Boundary Conditions

The FD model used here is a block model, and so we must consider how to treat boundaries. The top of the model is described as a free surface, as is the case on Earth. The bottom and sides of the model however are described as absorbing boundaries, which do not reflect seismic energy, and so a pseudo-infinite medium is simulated. Two methods of implementing an absorbing boundary are discussed below,

1. Perfectly Matched Layers (PML)
2. Exponential Dampening

Both methods effectively dampen the wavefield in an absorbing layer that simulates the infinite boundary as shown in figure 3.3. The formulation of the free surface, as well as both methods of approximating an absorbing boundary condition are considered below.

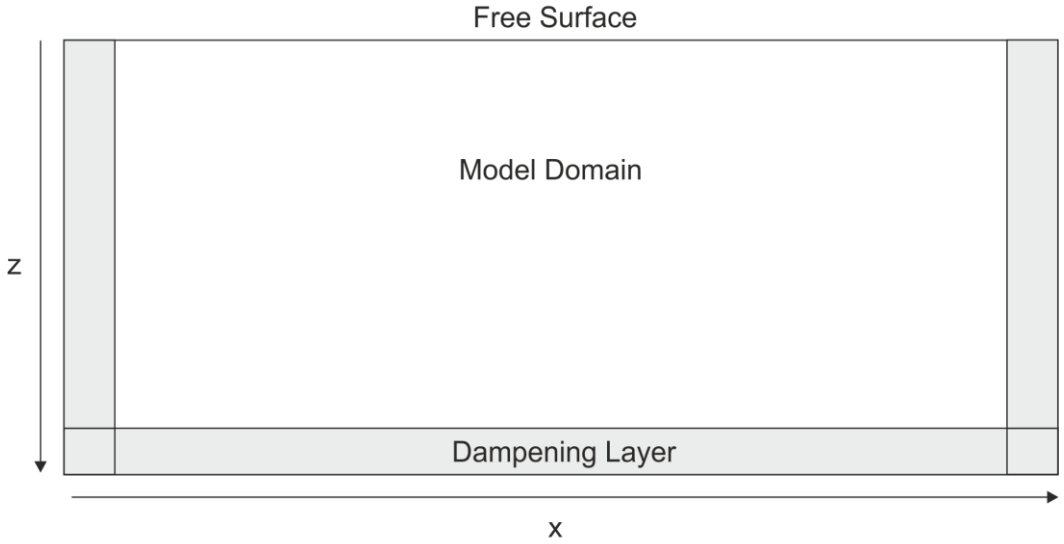

Figure 3.3 – Model boundaries of FD model. Top boundary is described as a free surface. Side boundaries have a dampening layer of thickness n_l. The dampening layer is either an exponential dampening layer or a PML.

3.3.1 The free surface

At the top of the model (*z = 0*) a free surface is implemented following Lavender *et al.* (1988) where the vertical stress components (τ_{zz} and τ_{xz}) at the top of the model are mirrored across the top surface ($z = 0$). The horizontal stress component (τ_{xx}) is not modified. In order to allow for the staggered grid implementation the stresses are considered to be symmetrical about the surface (z = 0). In the case of a fourth-order FD scheme, as is used here, this means that there are two nodes above the surface (Bohlen, 2002).

3.3.2 Absorbing Boundaries

An important feature of a seismic wave propagation model is to prevent reflections from the model boundaries, hence simulating an infinite medium. A variety of methods for absorbing seismic energy at the edges of the model domain have been proposed. They include exponentially dampening the velocity and stress values within the absorbing layer as proposed by Cerjon *et al.* (1985), using PMLs to introduce a large dampening factor (e.g. Collino & Tsogka, 2001), or other methods that are not explored in this project such as implementing a very low Q at the model boundaries (e.g. Bohlen, 2002).

The PML method has been shown to be the most effective method by far for absorbing a wave indenting the boundary at a near perpendicular angle. However the classical PML formulation (Collino & Tsogka, 2001), and even the more recent convolutional PML implementation are less effective at dampening waves that are incident on the absorbing boundary at very shallow angles, referred to as 'grazing waves'. The widely used method of introducing an exponential dampening term in the absorbing layer (Cerjon *et al.,* 1985) is less effective at absorbing a wave at normal incidence, but is more effective at absorbing a grazing wave as the energy is simply reduced at every time step. This is of particular importance in 3D modelling as is discussed in Chapter 4.

3.3.3 Perfectly Matched Layers (PML)

The PML method works by matching the velocity and density of the PML with that of the model interior, so that no artificial reflection is seen from the interface. Therefore a very large damping parameter can be introduced, allowing the PML to be relatively thin compared to other absorbing boundary conditions. In theory, for a perfect solution of the wave equation this boundary should be perfectly invisible to an incident wave. However in practice, due to the FD approximation of the constituent equations some reflection is seen.

For this reason the PML must be at least 10 nodes thick. This is however still much thinner than other non-reflecting boundaries, and so can significantly reduce the computational cost of the absorbing boundaries.

PMLs were originally introduced for modelling Maxwell's equations (Berenger, 1994), and were adapted for use in a Virieux velocity stress FD scheme by Collino & Tsogka (2001). This formulation splits the particle velocities into the motion perpendicular and parallel to the boundary being considered. The particle motions perpendicular to the boundary are then dampened, while the particle motions parallel to the boundary are not modified. While this PML implementation is highly effective in comparison to previous techniques at dampening an incident wave it has two draw backs. 1) Splitting the formulation of velocity and stress increases the number of variables needed, and so the computational costs. 2) Grazing waves that are incident on the boundary at very shallow angles are not adequately dampened (Komatitsch & Martin, 2007).

Convolutional PMLs (cPMLs) however do not require the velocity and stress variables to be split into the parallel and perpendicular components, reducing the overall computational costs and improving the dampening of a grazing wave. This improved PML method has been applied to the elastic (Komatitsch & Martin, 2007) and visco-elastic case (Martin & Komatitsch, 2009), and is implemented in the version of SOFI3D used for waveform modelling in this work.

In this project PMLs have been explored as boundary conditions in the hope that this more efficient boundary condition would allow a more tightly constrained model area to be simulated, hence reducing the computational costs. As we used 3D corridor models (discussed in Chapter 4), many of the reflections seen were grazing waves. Exponential dampening methods have therefore proved effective at dampening these grazing side reflections. Implementing cPMLs in 3D has however proved problematic.

3.3.4 Exponential Dampening

The more established method of dampening the wave field at the absorbing boundaries of the model is to introduce a dampening parameter throughout the boundary layer as described by Cerjan *et al.* (1985), and widely implemented (e.g. Graves, 1996; Bohlen 2002). At all points within the dampening layer the particle velocity and stress are multiplied by the value Dx where,

$$D_x = e^{(-a^2x^2)} \quad , \tag{3.10}$$

where x is the distance within the layer, and a is given by,

$$a = \sqrt{\frac{log A_0}{n_l}} \quad , \tag{3.11}$$

where A_0 is the amplitude by which the wave is reduced (Bohlen *et al.,* 2011). In the model setup used $A_0 = 0.92$, giving an 8% reduction in particle velocity and stress for each time step. The width of the absorbing layer for this type of absorbing boundary condition is typically 30 nodes or greater (Bohlen *et al.,* 2011).

3.4 Source Implementation

The FD scheme shown in equation 3.1 of this chapter can be modified to include a body force term allowing source implementation via body forces. In this project however the source is input to the stress field following Virieux (1986). For simplicity an explosive source is used in many of the models. A double couple source is used however in some instances, particularly in the scattering analysis models where it is important that S-waves are excited at the source. The implementation of an explosive and double couple source is described below. The amplitude of both of these source mechanisms varies with time and are described by the source time functions discussed below.

3.4.1 Source Time Function

Two source functions are used in this project, both of which are essentially spike sources designed to give an approximately flat spectral range. The resulting waveform is then low pass filtered to the model resolution to remove grid dispersion effects at higher frequencies. Any source spectrum can then be applied to the waveform that is produced. In general in this project the source spectrum is simulated by passing the waveform through a second-order Butterworth filter, where the corner frequency of the filter represents the source corner frequency. The source time functions used are shown in figure 4a, and the unfiltered amplitude spectra of these sources are shown in figure 4b.

3.4.2 Explosive Source

For an explosive source the stress terms are modified at time (t) , and are given below in the vertical and horizontal directions for the 2D case,

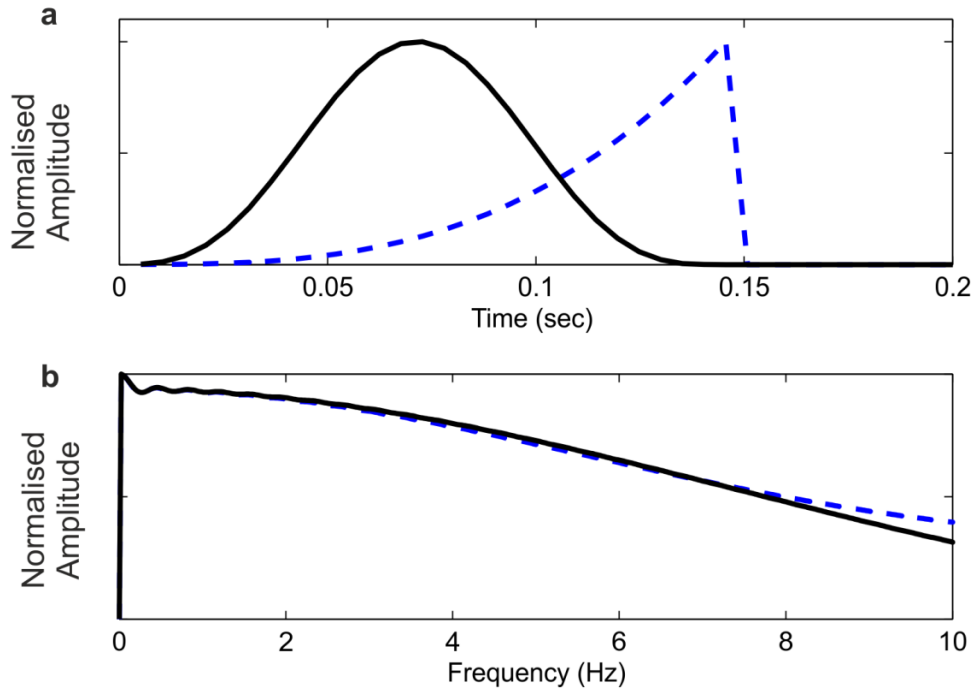

Figure 3.4 – Source time function. The sine wavelet and slip patch source models are shown by the solid black and dashed blue lines respectively **a)** in the time domain and **b)** the frequency domain.

$$\frac{\partial \sigma_{xx}}{\partial t} = S_t$$

$$\frac{\partial \sigma_{zz}}{\partial t} = S_t \tag{3.12}$$

For the 3D case the source wavelet is also applied in the y-direction,

$$\frac{\partial \sigma_{yy}}{\partial t} = S_t \tag{3.13}$$

An explosive source only excites P-waves, and so is used in models where only the first arrivals of the P-wave are of interest.

3.4.3 Double Couple Source

The double couple source is a more realistic approximation of an earthquake source, where the fault plane orientation is given. Unlike the explosive source both P and S-waves are excited as there are shear stresses as well as compressional stresses at the source. The double couple source is also excited in the stress field as proposed by Coutant *et al.* (1995) following the precedence of Virieux (1986). For the 2D case the stresses are given by,

$$\frac{\partial \sigma_{xx}}{\partial t} = -S_t \sin(2\theta_s)$$

$$\frac{\partial \sigma_{zz}}{\partial t} = S_t \sin(2\theta_s) \tag{3.14}$$

$$\frac{\partial \sigma_{xz}}{\partial t} = S_t 4 \sin(2\theta_s + 90)$$

where $\theta_s$is the source angle. For 2D simulations the source can be explained by this one parameter, which represents the dip of the fault on which the simulated earthquake occurs.

3.5 Stability Criterion

To check that the FD model is stable we must ensure that the grid spacing (dh) and time step (dt) are appropriate for the velocity and frequency range that is being modelled. These variables depend on the maximum frequency that we wish to accurately model (f_{max}) and the seismic velocities that we want to use. Below the temporal stability criterion (the Courant criteria) and the spatial stability criterion are described.

3.5.1 Temporal stability criterion

We must ensure that the time step is small enough that a wave travelling at the maximum velocity in the model ($v_{p_{max}}$) can travel from one node to the next in a single time step. This is known as the Coutant criterion, and if it is not satisfied then the modelled wave tends to infinity within a few time steps. The Courant criteria is shown below,

$$dt \leq \frac{dh}{h\sqrt{n_{dim}} v_{p_{max}}} \tag{3.15}$$

where $n_{dim}$is the number of spatial dimensions of the model. Note that dt therefore must be smaller in a 3D model than in a 2D model. The variable h is dependent on the FD order used, and $h = 7/6$ for the fourth-order FD model using Taylor coefficients as used in this project.

3.5.2 Spatial stability criterion

Grid dispersion occurs when the nodes of a model are too coarsely spaced. This means that at a given time, a wavelength is not sampled enough times along its length. As has been discussed the number of times a wave must be sampled per wavelength (n) reduces if a higher order FD model is used. In this work we have used fourth-order Taylor coefficients,

therefore n = 8 to 10 (Bohlen *et al.*, 2011; Moczo, 1998). The grid spacing is then given by the following equation,

$$dh \leq \frac{v_{s_{min}}}{n\, f_{max}} \tag{3.16}$$

Where v_{smin} is the minimum S-wave velocity in the model. The minimum grid spacing must therefore be $^1/_8$ to $^1/_{10}$ of the minimum wavelength.

3.6 Domain Decomposition

To run FD simulations at the resolutions needed for this project requires a large amount of computational resources. In order to run both the 2D and 3D models the simulations must be run in parallel on several processors. In this project both the 2D and 3D simulations are run on the UK national supercomputer HECTOR.

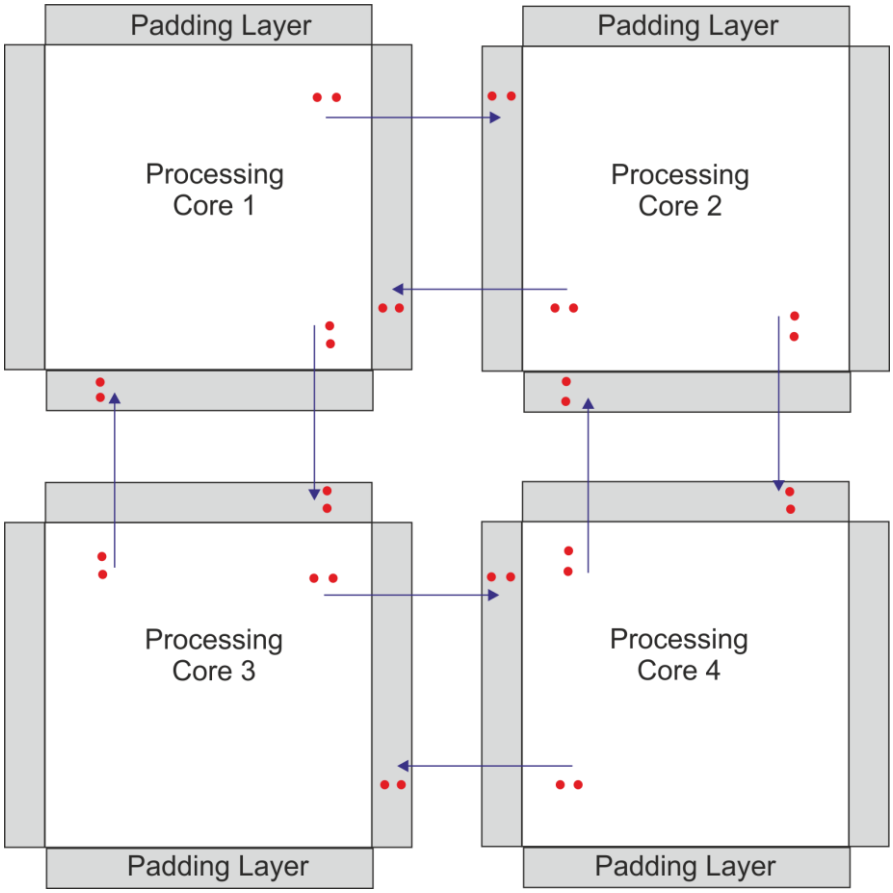

Figure 3.5 – Domain Decomposition. The model domain is broken up into several equal areas. The padding layer exchanges the particle velocities, stresses and other variables from one processor core to another using MPI (Message passing interface). As a fourth-order FD scheme is used, the variables from two model nodes must be passed between domains. This figure is modified from Bohlen *et al.* (2002).

The 2D model setup was run on phase 1, 2a, 2b and 3 of HECTOR. Phase 3 of HECTOR allowed for 3D models to be run at useful resolutions. Hector phase 3 consists of 2816 compute nodes, each with 32 cores and 2 Gb of memory. The model setups described in Chapter 4 are optimised for this computer architecture.

The numerical models used (SOFI2D and 3D) are written for use in parallel. The model domain is separated into several parts with an equal model area (in 2D, or volume in 3D). Each part of the model is then run on a separate processor. This is referred to as domain decomposition. As the model setups used do not run on a single HECTOR compute node, the variables from the edge of each model section must be communicated to the neighbouring sections, using a message passing interface (MPI). The fourth-order staggered grid implementation that is used means that there must be two model nodes in the 'padding layer' that is communicated to neighbouring sections at the end of each time step. A schematic diagram of the domain decomposition with the padding layer is shown in figure 3.5.

3.7 Summary

The FD method outlined above produces full and realistic synthetic waveforms that can be used to test the response of seismic waves to a given elastic or visco-elastic structure. The stability criteria described in section 3.5 show that the grid spacing and time step reduce if higher frequencies are accurately modelled for a given velocity model. This effectively increases the amount of calculations required, and so the computational cost of a model run. Introducing effective absorbing boundary conditions and memory variables to simulate the viscous deformation also increases the number of calculations and amount of memory required. Therefore the methods presented in this chapter allow the full synthetic waveform to be produced, but there is a trade-off between the computational costs of a model, and the boundaries in which the model is realistic.

Symbol	Meaning
$\boldsymbol{v_z}, \boldsymbol{v_x}$ & $\boldsymbol{v_y}$	Velocity in the vertical (z) and horizontal (x and y) directions respectively.
$\boldsymbol{\sigma_{zz}}, \boldsymbol{\sigma_{xx}}$ & $\boldsymbol{\sigma_{yy}}$	Stresses in the z, x and y directions respectively
$\boldsymbol{\sigma_{xz}}, \boldsymbol{\sigma_{xy}}$ & $\boldsymbol{\sigma_{yz}}$	Stresses between the xz, xy and yz planes respectively
$\boldsymbol{\lambda}$ & $\boldsymbol{\mu}$	Láme's parameters
$\boldsymbol{\rho}$	Density
$\boldsymbol{k_0}$	Elastic moduli of the media
$\boldsymbol{k_l}$	Elastic part of Maxwell body l
$\boldsymbol{n_l}$	Viscous part of Maxwell body l
$\boldsymbol{L}$	Number of Maxwell bodies
$\boldsymbol{\tau_{\sigma l}}$ & $\boldsymbol{\tau_{\varepsilon l}}$	Stress relaxation time & strain relaxation time respectively
$\boldsymbol{Q}$	The quality factor
$\boldsymbol{\omega}$	Angular frequency
$\boldsymbol{\tau}$	Defined following Blanch *et al.* (1995) as shown by equation 3.5
$\boldsymbol{\tau^p}$ & $\boldsymbol{\tau^s}$	τ parameter for P & S-waves
$\boldsymbol{\pi}$	Analogous to the elastic term $(\lambda + 2\mu)$ for the visco-elastic case
$\boldsymbol{\mu_v}$	Analogous to Láme's parameter μ for the visco-elastic case
$\boldsymbol{\omega_0}$	Centre frequency of the modelled wave
$\boldsymbol{r_{zz}}, \boldsymbol{r_{xx}}$ & $\boldsymbol{r_{xz}}$	Memory variables for 2D visco-elastic formulation corresponding to the stress terms σ_{zz}, σ_{xx} & σ_{xz} respectively
$\boldsymbol{D_x}$	The dampening parameter (different for exponential or PML absorbing boundary)
$\boldsymbol{a}$	See equation 3.10 and 3.11.
$\boldsymbol{A_0}$	Exponential dampening amplitude
$\boldsymbol{s_t}$	Source time function
$\boldsymbol{\theta_s}$	Source angle for a double couple source
$\boldsymbol{dh}$	Grid spacing

$\boldsymbol{dt}$	Time step
$\boldsymbol{v_{pmax}}$	Maximum p-wave velocity in the model domain
$\boldsymbol{v_{smin}}$	Minimum s-wave velocity in the model domain
$\boldsymbol{f_{max}}$	Maximum frequency resolved by the model set up
$\boldsymbol{n}$	Number of times wavelength is to be sampled (8-10 for a 4^{th} order FD scheme)
$\boldsymbol{h}$	Variable dependent on the FD scheme used. This is used to calculate the minimum time step ($^{7}/_{6}$ for a 4^{th} order FD scheme)
$\boldsymbol{n_{dim}}$	Number of dimensions of the model (2 or 3 dimensional models used)

Table 3.1: Definition of terms used in Chapter 3 equations.

Chapter 4

Constraining Guided Wave Dispersion with Full Waveform Modelling

Subduction zone guided waves spend longer interacting with subducted oceanic lithosphere than any other seismic phase. Therefore these waves have the potential to tell us a large amount about the seismic structure of the WBZ. In order to resolve this structure, observed dispersed waveforms that have sampled the subducted slab are directly compared with synthetic waveforms, allowing a more detailed picture of the subducting slab to be inferred.

In the first part of this chapter the methods used to constrain subduction zone guided wave dispersion are introduced. The method by which these observations are compared to synthetic seismograms is then described, for both the dispersive first arrivals and the extended P-wave coda. The second part of this chapter then describes the setup of the numerical model that is used to produce the synthetic waveforms that are compared to the dispersed first arrival and extended P-wave coda.

4.1 Measuring Dispersed Waveforms

As has already been discussed dispersed P-wave arrivals observed in the forearc of subduction zones across the globe have been attributed to low velocity subducted oceanic crust that acts as a waveguide (e.g. Abers, 2000; Martin *et al.,* 2003). Several groups have taken different approaches to measure and quantify the observed dispersion as discussed in Chapter 2.

To summarise, Abers (2000; 2005) observes waveguide effects at a wide range of subduction zones, and focuses on observing the relative delay of the higher frequency energy using a spectrogram. Martin *et al.* (2003) and subsequent papers, model the subduction zone waveguide and use the characteristic signal of the guided wave in the frequency domain to constrain the waveguide structure. Furumura & Kennet (2005) note that dispersed arrivals in Northern Japan are also associated with an extended P-wave

coda, and use this coda to suggest that the subducting slab contains large velocity variations. In this thesis all three of these approaches are used and combined to give a broader measure of the velocity structures that cause the observed dispersion. Combining these methods allows us to better resolve the velocity structures associated with WBZ seismicity.

4.1.1 Measuring dispersed first arrivals

The relative arrival times of different frequencies of the dispersed waveform onset are measured using a spectrogram following Abers (2000; 2005). The method used was originally proposed to measure surface wave dispersion (Dziewonski *et al.,* 1969), but has also been applied to body wave dispersion arising from subduction zone guided waves by Abers (2000; 2005).

The signal is filtered through a bank of zero phase Gaussian band pass filters with centre frequency (f_c) increasing from 0.25 Hz in increments of 0.25 Hz. Spectrograms are plotted between 0.25 Hz and the maximum frequency. The maximum frequency can be 5, 8, 12 or 16 Hz depending on the sampling frequency of the observed waveform, and also the resolution of the model that produced the synthetic waveform. The relative arrival times of the different frequency bands are then normalised to the 0.5 Hz frequency band, as this is the lowest frequency band that is consistently stable in the observed dispersed waveform (Abers, 2005).

The Gaussian band pass filter is implemented using the method of Abers (2000; 2005), and is described in the frequency domain by the following equation,

$$A(f) = e^{\left(\frac{-a(f-f_c)^2}{f_c}\right)} \tag{4.1}$$

Where, f = Frequency

$A(f)$ = The amplitude response of the filter at frequency f.

f_c = Centre frequency of the Gaussian band pass filter

a = Tuning factor, which in affect controls the bandwidth of the Gaussian filter.

A tuning factor between 4 – 8 gives a clear dispersion.

The relative amplitude of a given frequency can be shown by plotting the velocity spectrum of the waveform. The velocity spectrum of the signal is taken for the same window of waveform that the spectrogram is applied to (i.e. the first few seconds of arrivals).

Taking a window of the first arrivals of the P-wave is an important step for plotting a spectrogram of the dispersed waveform onset in the observed waveforms. If a window is not taken then the maximum amplitude of arrival for a given frequency band can occur in the strong P-wave coda, or for more shallow events even in the S-wave. For the spectrogram to produce a sharp dispersion curve the later arrivals must therefore be removed. The P-wave first motion is manually picked, and the initial window is taken, with 5 seconds before the first arrival and 9 seconds after the first arrival. A 1 second cosine taper is applied. The size of the window is then refined to remove later arrivals, and produce a reasonable dispersion curve.

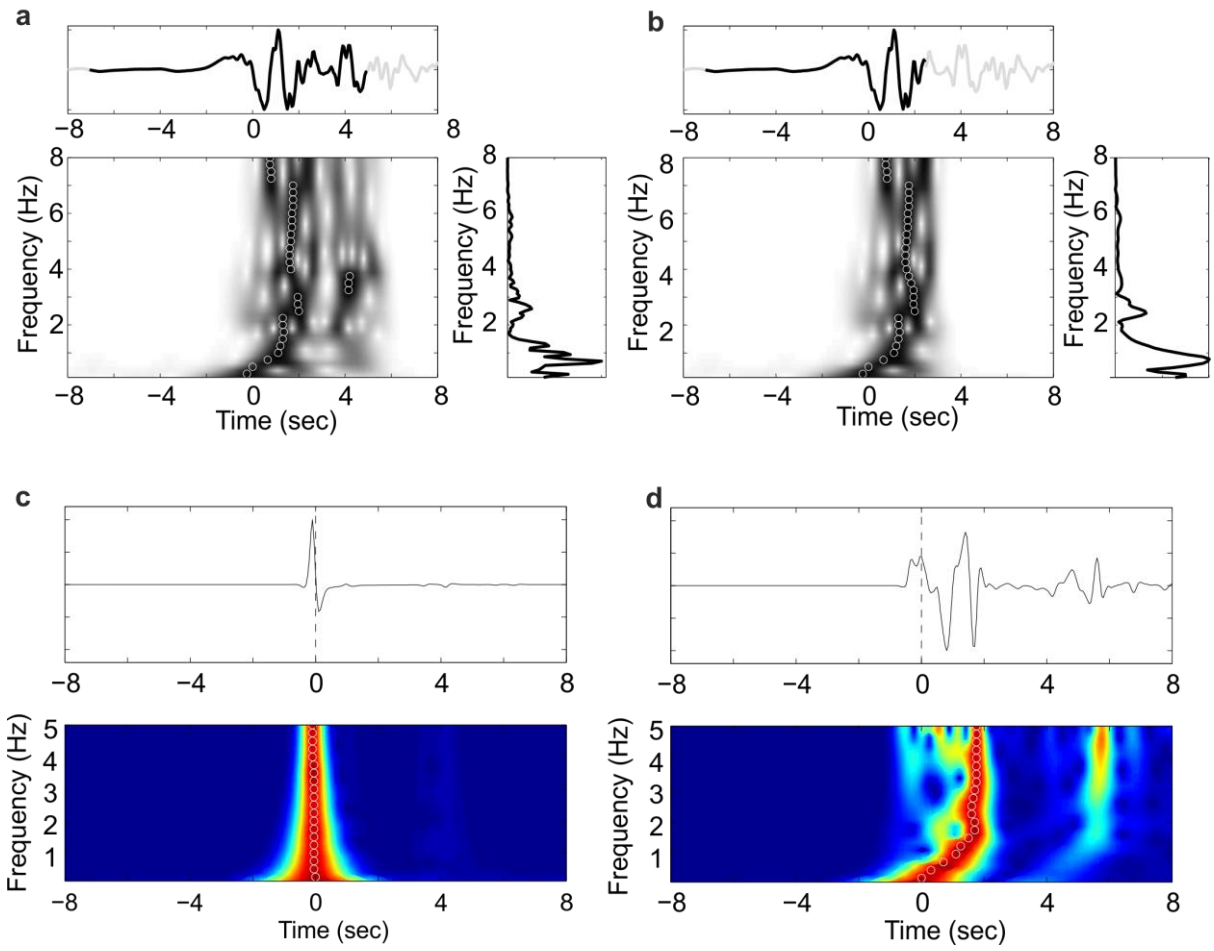

Figure 4.1 – Spectrograms of observed and synthetic subduction zone guided waves. **a)** Observed spectrogram with 12 second window. **b)** Same spectrogram with a refined window to remove later arrivals. In both a and b the top panel shows the raw waveform, shown in black inside the window . The portion outside of the window (including the taper) is shown in grey. The bottom left panel shows the spectrogram, with the arrival of the peak amplitude shown by a white circle. The bottom right panel shows the velocity spectra. **c)** Non-dispersive synthetic waveform produced from FD model. **d)** Synthetic dispersed waveform produced by a modelled subduction zone waveguide.

Figure 4.1 shows the comparison of an observed waveform plotted as a spectrogram with a refined (figure 4.1a) and unrefined window (figure 4.1b). The spectrogram of a dispersed and undispersed synthetic waveform is also shown in figure 4.1c and 4.1d, respectively.

4.1.2 Waveform Comparison

In order to constrain the velocity structure that is responsible for the dispersion observations that are presented in later chapters, the arrivals are simulated using the finite difference (FD) waveform propagation modelling method introduced in the Chapter 3. The synthetic waveforms that are produced are then compared directly to the observed waveforms.

The relative timing of the arrival of different frequency bands of the waveform is constrained using the spectrogram. The synthetic waveform is processed in exactly the same way as the recorded waveforms and are filtered by the same bank of Gaussian band pass filters as the observed waveform. The arrival time of the peak energy of a given frequency band is plotted over the observed spectrogram to allow for a direct comparison. The velocity spectra of the synthetic waveform is also plotted with that of the observed waveform, allowing the relative amplitude of a given frequency band to be directly compared (see figure 4.2).

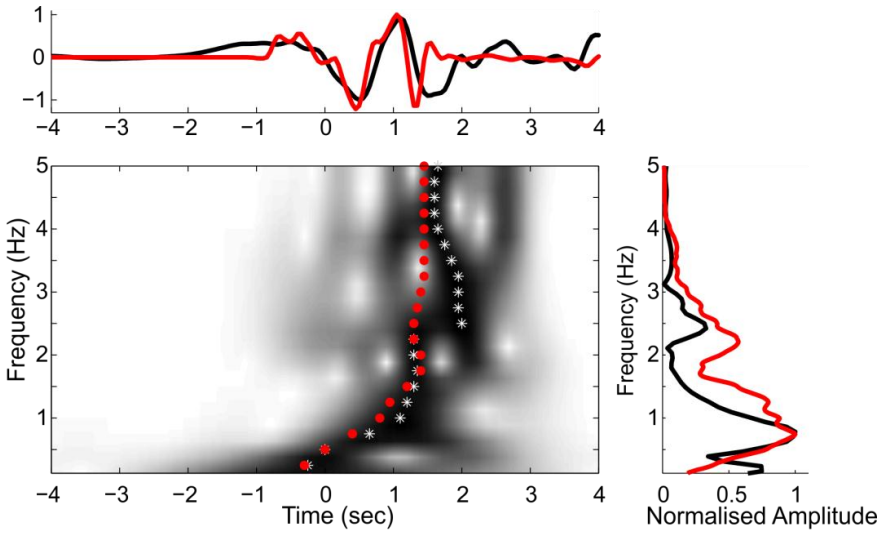

Figure 4.2 – Example of a fitted waveform from Northern Japan (see Chapter 6). In all panels the observed waveform is shown in black and white and the modelled waveform is shown red. The bottom left panel shows an example of the comparison between the observed and synthetic spectrogram. The grey scale shows the amplitude of the recorded wave, and white stars show the arrival time of the maximum amplitude of a given frequency. The arrival of maximum amplitude of a given frequency band in the synthetic waveform is shown by the red circles. The bottom right panel shows the comparison of the velocity spectra. The top panel shows the comparison of the observed and modelled waveform, low pass filtered at 2 Hz.

In fault zone waveguide experiments it is noted that there are clear trade-offs between the velocity and width of the fault waveguide, the position of the source within the waveguide, and quality factor of the fault zone (e.g. Ben-Zion, 1998). Resolution tests of waveguide velocity and width presented in chapter 6 show that similar trade-offs apply in subduction zone waveguides. However constraining the waveform in both the time and frequency domain reduces these potential trade-offs, as is discussed in further detail in chapter 6.

If the waveform is constrained in these two ways then the low pass filtered synthetic waveform can be directly compared to the low pass filtered observed waveform as shown in figure 4.2. The waveform is generally reasonably well matched up to 2 – 2.5 Hz. Resolution tests with a wide range of waveguide widths, velocities, source positions and slab structures can then be used to constrain the structure that is causing the dispersed first arrivals. The role of attenuation and the significance of modelling waveguide structure in 3D are also discussed in chapter 6.

4.1.3 Measuring P-wave coda

The method described above allows for the first arrivals of a dispersed waveform to be tightly constrained, which in turn has the potential to give new insight to the velocity structures responsible for the observed dispersion. This method however only constrains the first few seconds of arrivals and much of the waveform is still neglected. This is particularly significant in the subduction zone setting as it has previously been noted that the dispersed arrivals from WBZ events are also associated with an extended P-wave coda (Furumura & Kennett, 2005).

It is likely that this coda is caused by fine scale velocity structure, and therefore may be sensitive to subduction zone structures that are below the resolution of established seismic imaging techniques. Therefore a method for constraining this P-wave coda is needed, in order to give an indication of the bulk properties of the small scale scattering structures that cause the observed extended P-wave coda. The method developed in this project is described below.

The Coda Ratio

To quantify the P-wave coda at a given station the ‘coda ratio’ is introduced. This is calculated for high frequency arrivals at a given station, allowing the relative amplitude of the P-wave coda to be compared at different stations. The coda ratio for a given waveform is defined as the total displacement in the first four seconds of signal divided by the total

displacement 4 - 8 seconds after the first arrival. The first arrival (or first motion) is manually picked and the waveform is high pass filter (at > 3 Hz).

$$Coda\ Ratio = \frac{Total\ Displacement\ in\ the\ 2^{nd}\ Window\ (4-8\ seconds)}{Total\ Displacement\ in\ the\ 1^{st}\ Window\ (\ 0-4\ seconds)}$$

This can be summarised as,

$$Coda\ Ratio = \frac{\sum_{t=4}^{t=0} |v_{high}(t)|}{\sum_{t=8}^{t=4} |v_{high}(t)|} \tag{4.2}$$

Where v_{high} = The high pass filtered velocity signal

t = Time after the first motion

An example of the high pass filtered waveforms at several stations for an intermediate depth WBZ event is shown, along with the windows used in figure 4.3.

The Averaged Coda Decay

It has been noted the amplitude of the P-wave coda from events within the WBZ of Northern Japan is stronger at stations that are close to the trench (Furumura & Kennett, 2005). In order to constrain the WBZ velocity structure that is thought to cause this coda, we calculate the spatial coda decay for intermediate depth events within the WBZ. The spatial coda decay with distance from the trench (referred to as the coda decay from here onwards) is a measure of the amplitude of the P-wave coda relative to the first arrivals for each seismometer in a profile that transects the subduction zone forearc. This allows the relative strength of the coda at various distances from the trench to be quantified.

For a given event the coda ratio is calculated for the high pass filtered waveform at each station on the profile. The coda decay is then normalised to the station with the maximum coda ratio. The normalised coda decay from the several intermediate depth WBZ events can then be averaged. This method of averaging the normalised coda decay for several events removes source specific effects such as the orientation of the source focal mechanism, to produce an averaged coda decay. The averaged coda decay then gives a bulk measure of the scattering media that produces the extended P-wave coda that is observed. The measure of coda decay that is produced can then be compared to the coda decay that is produced by synthetic models of WBZ scattering structure. The methods by which the scattering media is simulated are outlined in the second half of this chapter.

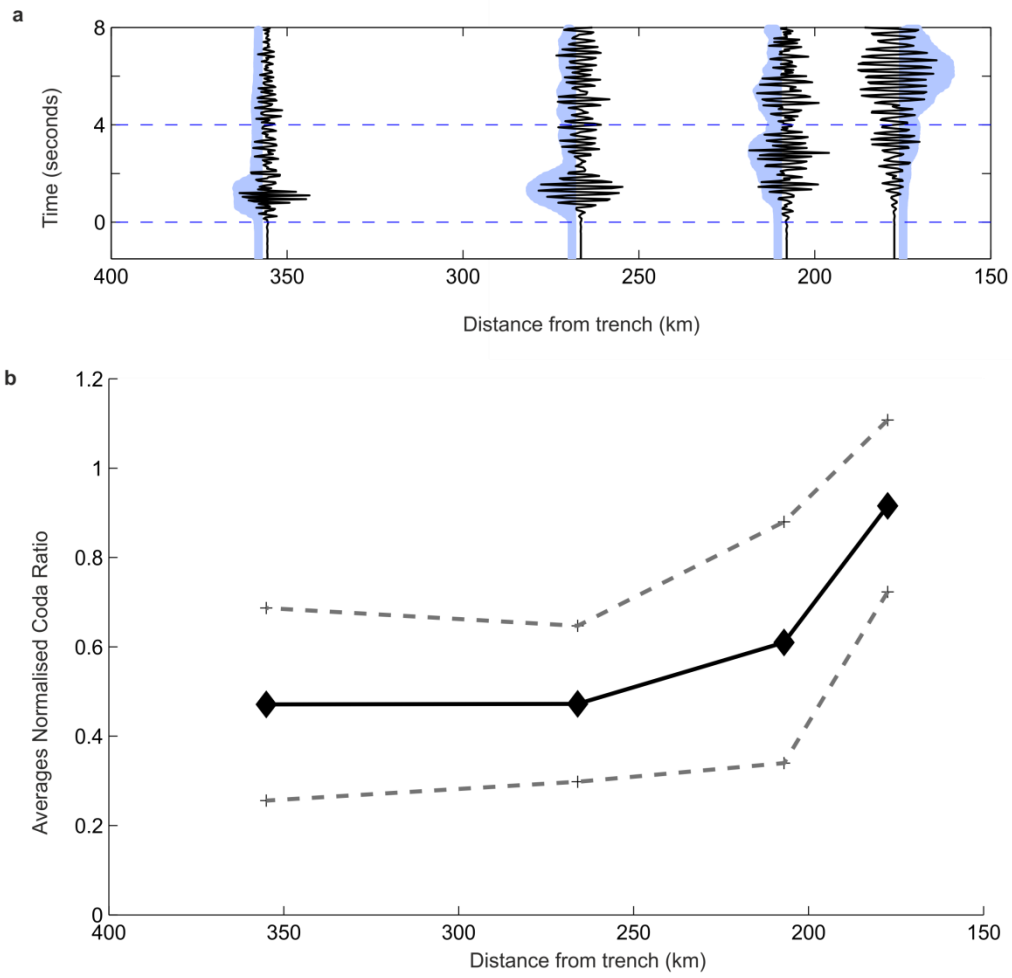

Figure 4.3 – Coda analysis. **a)** Black lines show the high frequency (> 3 Hz) arrivals at stations HSS, HID, KMU and ERM (left to right) in the Japanese for arc. The coda envelope for each station is shown in the blue-grey colour. **b)** The average normalised coda decay at the stations given above, plotted for seven events at depths of 70 – 150 km in the WBZ below Northern Japan.

4.2 Numerical model setup

In the first half of this chapter the methods that are used to measure and constrain the dispersion observed in subduction zone forearcs are introduced. The methodology used in this thesis relies upon these observations then being directly compared to synthetic waveforms produced by the modelling techniques described in chapter 3. The second part of this chapter describes the specific model setups used to model the elastic and visco-elastic media in 2D and 3D, for both deterministic kilometre-scale velocity structures and finer-scale non-deterministic scattering structures.

4.2.1 Deterministic Seismic Structure

Specific kilometre-scale features of the WBZ structure can be described by a deterministic seismic model. This allows features of the seismic structure to be varied allowing the waveform produced to be compared to the observed waveform.

Velocity structures

The basic subduction zone model with a low velocity layer of oceanic crust above a layer of high velocity cool lithosphere is the starting point for the modelling, and is shown in figure 4.4a. This represents the low velocity layer (LVL) structure that has previously been proposed to act as a waveguide for seismic waves, causing the dispersion observed in subduction zone fore arcs (e.g. Abers 2000; 2005; & Martin *et al.,* 2003). The geometry of the slab must be carefully modelled as the bend of the slab allows the high frequency seismic waves that are retained in the subduction zone waveguide to decouple from the LVL (Martin *et al.,* 2003).

The slab geometry used is partly based on *slab1.0* (Hayes *et al.,* 2012). This slab model is particularly well refined for the interface between the subducting and overriding plate. At these depths this model is partly based on the orientation of focal mechanisms from the global centroid moment tensor (CMT) catalogue. At greater depths *slab1.0* is defined by the EHB (Engdahl, van der Hilst, & Buland, 1998) catalogue of teleseismically relocated earthquakes.

The modelled slab geometry is therefore closely based on *slab1.0* at depths of < 50 km. At greater depths the slab geometry is based on the local seismicity catalogue produced by the Japanese Metrological Agency (JMA). These locations are likely to be more accurate than those of the global catalogue as they are based on arrivals recorded at a large number of local stations, and are located using a local velocity model.

In general a given event below 30 km is given a deeper location in the JMA catalogue than in the global earthquake catalogue. This phenomenon has been noted at several subduction zones and is most likely due to the fact that local earthquake catalogues will use a regional velocity model, rather than a global velocity model, for their locations (Syracuse & Abers, 2006). In a subduction zone setting the regional velocity is likely to be faster on average than the global 1D velocity model used for the EHB Earthquake locations.

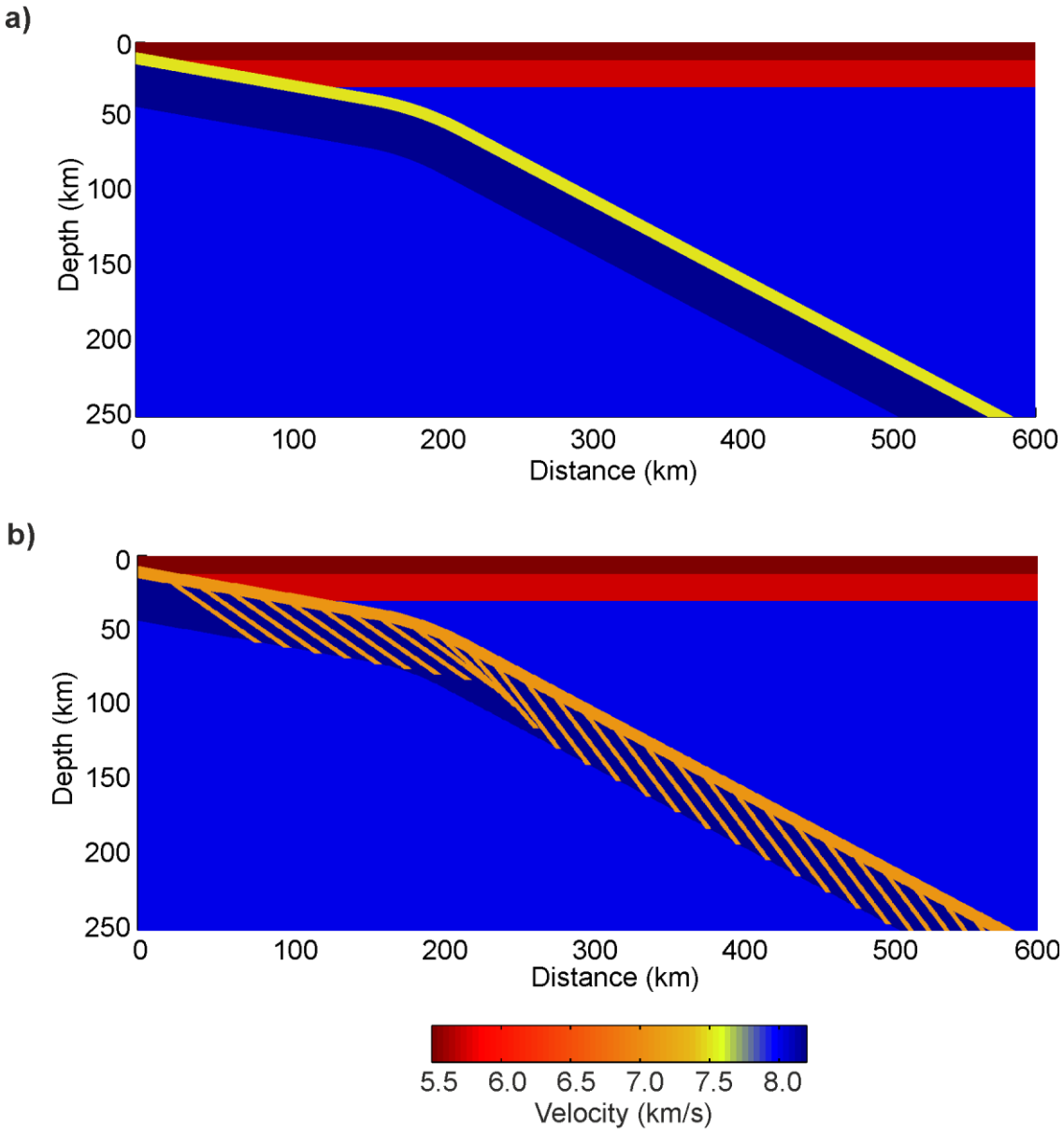

Figure 4.4 – Deterministic velocity models. **a)** The velocity model used for simulating guided wave dispersion due to an upper LVL in Northern Japan. **b)** The velocity model for Northern Japan including regularly dipping faults, that can also act as a waveguide.

The velocities used in the numerical model for the mantle material, the fast subducting lithosphere and the overriding crust are informed from the high resolution local tomographic models of Zhang *et al.* (2004) and Nakajima *et al.* (2009). The velocity and width of the LVL are varied considerably in the resolution models described in the observation chapters (Chapter 5 and 6) in part two of the thesis.

The dipping fault zone structure shown in figure 4.4b is introduced to explain dispersive events that occur well below the layer of low velocity oceanic crust. The geometry of the

faults follows the structures produced by the modelling of Faccenda *et al.* (2009; 2012), and the faulting angles of reactivated outer rise faults (e.g. Ranero *et al.,* 2005). The velocity and width of the fault zones, as well as the precise dip of a given fault zone is however determined from a range of possible values by a number of resolution tests that are compared to the observed waveforms as is described in chapter five.

Attenuation Structure

Previous studies have shown that there are wide variations in the seismic quality factor (Q) in subduction zones (Tsumura *et al.,* 2000). Studies of crustal fault zone waveguides have shown that there are potentially large trade-offs between the velocity, width and seismic quality factor of the wave guide structure. It is therefore important that the numerical model used can simulate variations in Q within the subduction zone structure. This is done using the visco-elastic rheology introduced in Chapter 3.

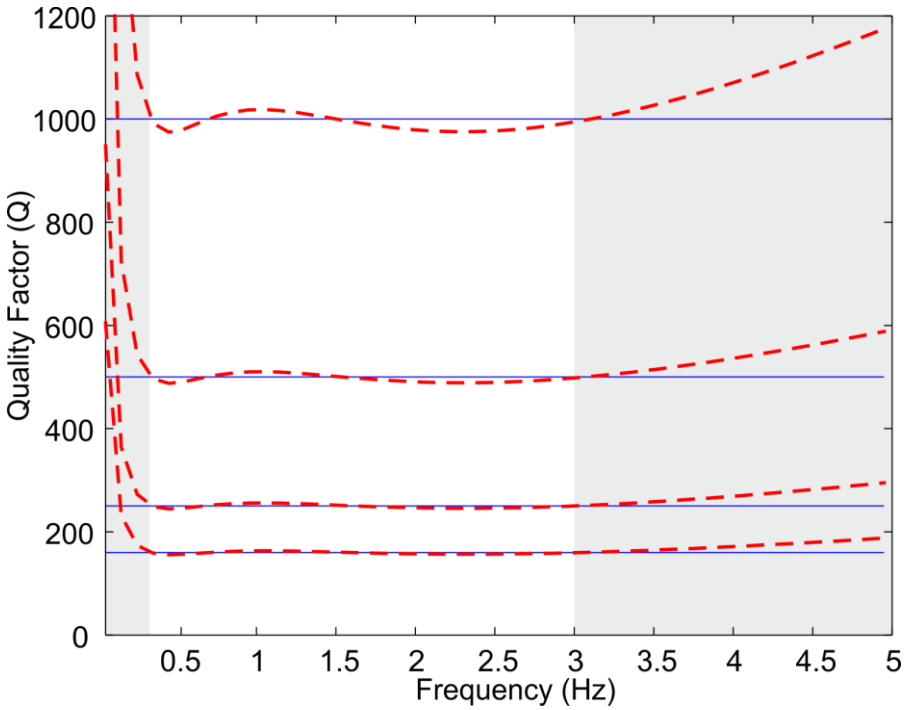

Figure 4.5 – Approximations of a constant Q. The values of Q to be approximated are shown by the solid blue line. The actual value of Q approximated by two Maxwell bodies is shown by the dashed red line. The Q approximation is refined by a least squares inversion in the range 0.25 – 3 Hz. The grey areas show the Q approximation at frequencies outside the band for which the GSLS is optimised.

Value of Q	τ	Relaxation Frequencies
1000	0.00165	0.3380 3.0917
500	0.0033	0.3387 3.1008
250	0.0066	0.3403 3.1191
160	0.0104	0.3422 3.1399

Table 4.1: Values used for estimation of different values of Q.

For the range of frequencies of seismic wave considered in this study, Q is assumed to be constant in the frequency domain. A pseudo-constant Q is approximated using L Maxwell bodies. In our model setup only two Maxwell bodies ($L = 2$) are used. This keeps the computational costs of these models to a minimum and also gives a good estimation of Q in the frequency range of interest (0.25 – 3.0 Hz).

The value of τ and the two relaxation frequencies are approximated using a least squares inversion, following the methodology proposed by Bohlen (2002). A range of Q values are inverted for, based on the attenuation tomography of Tsumura *et al.* (2000). The values of τ and the relaxation frequencies are shown in table 4.1, and the responses of the model at different values of Q are shown in figure 4.5.

4.2.2 Non–Deterministic Seismic Structure

While large kilometre-scale features can be modelled deterministically, as described in the section above, smaller-scale features are neglected by these models. When the coda of the P-wave arrival is being considered however, the waveform is sensitive to velocity perturbations on all scales. Smaller-scale features cannot be directly resolved and therefore cannot be modelled realistically by a deterministic velocity model. We therefore need to simulate the scattering media that causes the extended P-wave coda. We use a non-deterministic method that includes short wavelength velocity perturbations that other imaging methods are not directly sensitive to.

Modelling Scattering Media

The non-deterministic part of the velocity structure is introduced using a random scattering media, with a velocity $(\vec{r})$, defined by the equation below ,

$$v(\vec{r}) = v_0 + \delta v(\vec{r}) = v_0 \left(1 + \xi(\vec{r})\right) \tag{4.3}$$

Here the average velocity of the media is given by v_0 and the fluctuating part of the velocity at a given point is given by $\delta v(\vec{r})$, where $\vec{r}$ is the spatial vector, following Yoon (2005). The

fluctuating part of the velocity field is described using an auto-correlation function (ACF), which in effect gives the similarity of a medium parameters (i.e. v_p, v_s and ρ) with respect to the spatial vector $\vec{r}$.

Several types of ACF can be used to produce a random scattering media. Figure 4.6 shows a comparison of random media produced by a Gaussian, exponential and Von Kármán ACF. The Gaussian ACF appears smooth compared to the other two methods as it is relatively depleted in short wavelength variations. For this reason an exponential or von Kármán ACF is generally used to simulate a random scattering media in seismology. In this project a von Kármán ACF is used following Furumura & Kennet (2005).

In order to infer the scattering structure that leads to an extended P-wave coda we want to be able to test scattering media with a range of velocities, elongations and orientations. The methods by which these scattering media are produced are outlined below. The range of scale lengths in the random scattering media is described by the correlation length (c_l). Elongation of the scatterers is introduced by modifying the spatial vector by introducing the terms x_{mag} and y_{mag} , which give the elongation in the x-direction and y-directions respectively. The degree of elongation is then described by the aspect ratio A_r, where,

$$A_r = \frac{x_{mag}}{y_{mag}} \tag{4.4}$$

For a non-elongated scattering media the spatial vector is given by,

$$\vec{r} = \sqrt{\frac{x^2 + y^2}{c_l}} \tag{4.5}$$

While for the elongated scatterer the spatial vector is given by,

$$\vec{r} = \frac{\sqrt{\left(x^2 \,.\, x_{mag}\right) + \left(y^2 \,.\, y_{mag}\right)}}{c_l} \tag{4.6}$$

The spatial vector is then incorporated into the von Kármán ACF, which is given by,

$$a = \frac{2^{(1-\kappa)}}{e^{\Gamma(\kappa)}} \vec{r}^{\kappa} \, \mathrm{K}(\vec{\mathrm{r}}) \tag{4.7}$$

Where κ = the Hurst number

K = the modified Bessel function

Γ = the gamma function

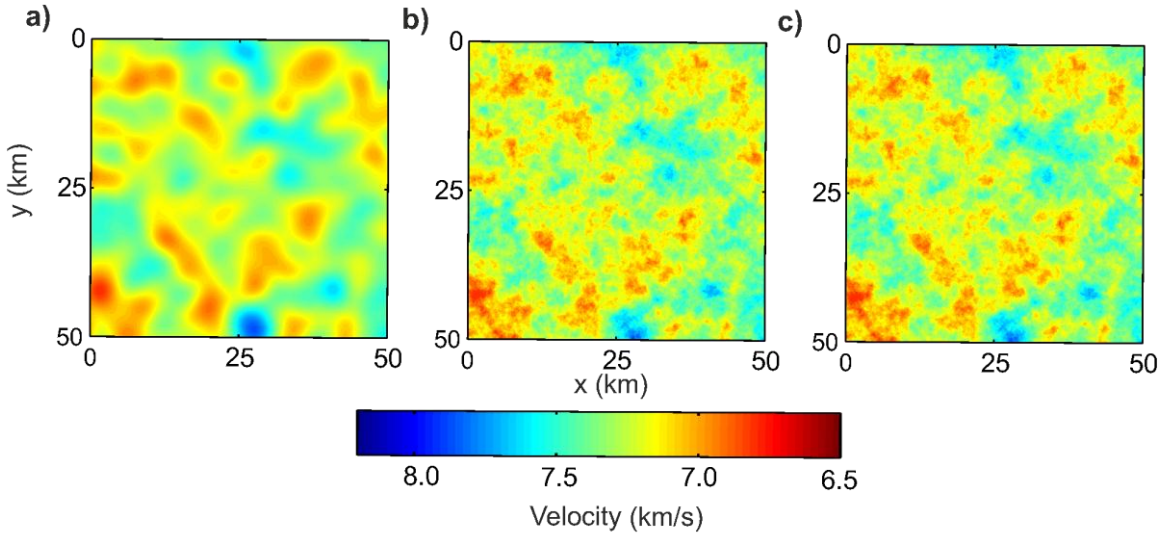

Figure 4.6 – Scattering media produced by different ACFs. Scattering media produced from **a)** a Gaussian ACF, **b)** an exponential ACF and **c)** a von Kármán ACF.

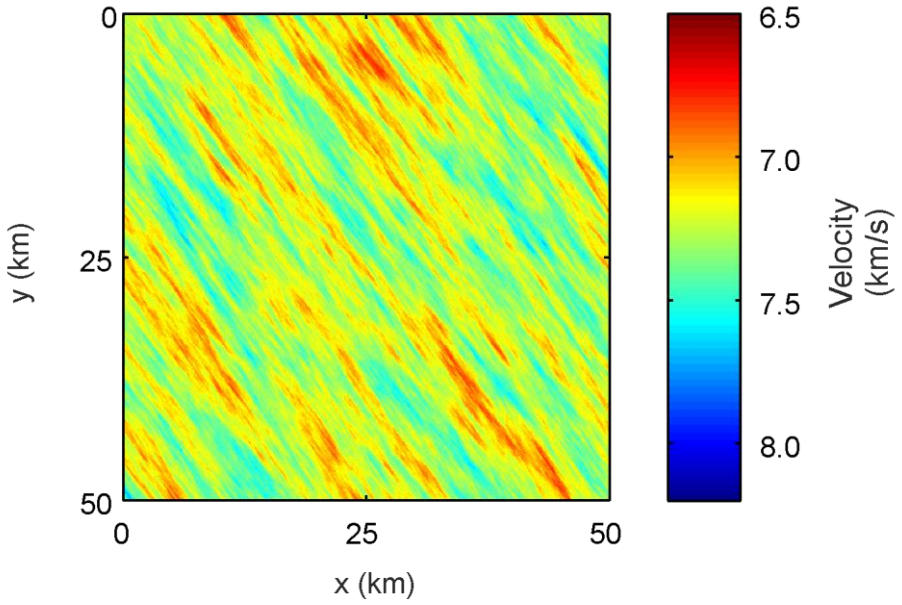

Figure 4.7 – Orientated elongated Von Kármán scattering media. The scattering media shown has an aspect ratio of 0.25, and the scatterers are orientated at 55° to the horizontal axis.

The random media is produced by taking the Fourier transform of the ACF shown above to give the amplitude spectrum of the ACF. The phase spectrum is then multiplied by a random cosine and sine phase respectively, to produce a modified phase spectrum. The inverse Fourier transform of this modified amplitude spectra is then taken to give the normalised random fluctuations. These fluctuations are then scaled to the required standard deviation to give the fluctuating part of the model, $\delta v(\vec{r})$, and multiplied by the

average velocity, v_0 , to give the random media with velocity $v(\vec{r})$ (Bohlen, 1998; Yoon, 2005)

The random media produced by this method will be elongated if an aspect ratio has been applied. However the scatterers have not been orientated. The desired orientation is then applied to the elongated scattering media by rotating the coordinate system of the random media. An example of an elongate rotated scattering media is shown in figure 4.7.

4.2.3 Waveform Modelling in 2D and 3D

Subduction zones are often simplified to a 2D system for modelling purposes. While this reduces the computational costs, and therefore allows greater complexity to be considered, it also means that along strike variations are generalised and 3D effects are ignored.

The waveform fitting and coda decay resolution tests require a large amount of models to be run. These models must also be run at relatively high resolution in order to be able to accurately simulate seismic waves up to at least 5 Hz. Therefore these models are run in 2D as the computational cost of running all these models in 3D would be far too high. To give an indication of the relative costs of modelling a subduction zone system in 2D and 3D figure 4.8 shows the number of calculations that are needed for a 90 second simulation, at various frequencies in 2D and 3D. At the relevant frequencies the 3D model is far more expensive. 3D effects may however be important, especially in relation to waveguide structures. For this reason the seismic structures that are resolved by the 2D modelling are tested using the more computationally expensive 3D models. With the computational resources available for this project we are able to benchmark 3D models with a resolution of up to 2.5 Hz. Both the 2D and 3D models are run in parallel, with the model domain split over several processors as described in chapter 3. The specific parallel setups of the 2D and 3D models are described below.

4.2.4 2D model setup

Both elastic and viscoelastic 2D models are used to test the seismic structures that may account for the observed dispersed waveforms. These models are run at a variety of different resolutions depending on the observation, and to reduce the overall computational cost. Waveguide simulations for the observations from Northern Japan (Chapters 5 & 6) are run using 2D models with 5 Hz resolution. This is because there is generally minimal energy in the recorded seismograms above 5 Hz, as the source corner frequency of a clearly recorded intermediate depth events is generally well below this.

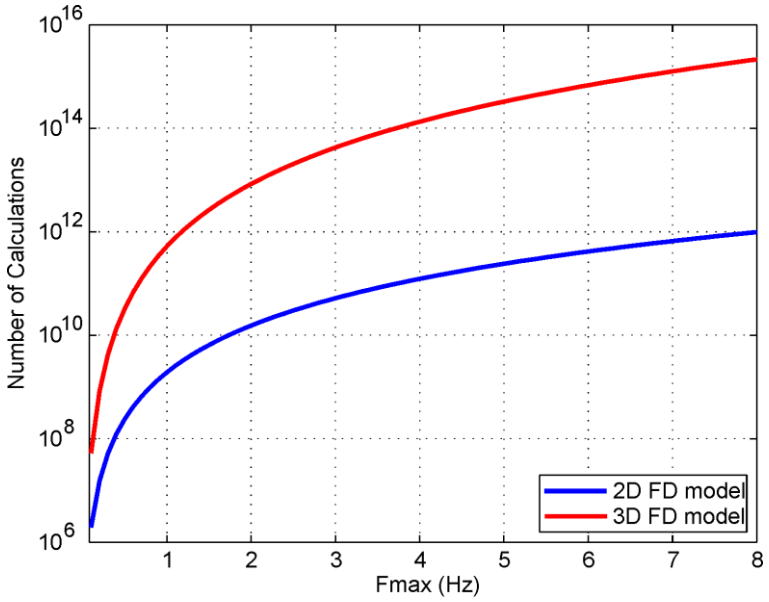

Figure 4.8 – The relative cost of 2D and 3D FD models. This figure shows the number of calculations needed for a 2D and 3D subduction zone corridor model setup based on the stability criteria given by equations 3.24 and 3.25, where F_{max} is the maximum frequency resolved by the model. The model dimensions are based on the model setups described in tables 4.2 and 4.3.

In the appendix of the thesis preliminary simulations of waveguide dispersion in South America are shown. The delayed arrivals are at higher frequencies in this case, and so these models are run to 12 Hz resolution. The specific 2D model setups for both subduction zones are shown in table 4.2. The cost of a model on phase 3 of HECTOR is given in terms of KAus (1000 allocation units). One KAu is equivalent to 250 hours on one core (32 nodes) on phase 3 of HECTOR.

Model Resolution	**5.0 Hz**	**12.0 Hz**
Dh	75	25
dt	0.0052	0.00184
No. of grid points in x direction	10080	28000
No. of grid points in y direction	3500	14000
Model Length in x (km)	756.00	700
Model Length in y (km)	261.50	350
No. of processors in x	16	16
No. of processors in y	10	16
KAus per job (Elastic)	0.138	4.57
KAus per job (Visco-Elastic)	0.266	-

Table 4.2: 2D model setups.

4.2.5 3D model setup

As has been discussed, 3D models are far more computationally expensive that 2D models. Modelling waveguide effects to useful frequencies requires a large amount of parallel computing resources. These resources have become available with phase 3 of the UK national super computer HECTOR. To limit the cost of the 3D models as much as possible the subduction zone is modelled as a 'corridor model'. This means that the model domain is just over the length of the ray path in the x-direction, and just over the depth of the source in the z-direction. The width of the modelled corridor is then as small as possible in order to reduce the computational costs. The corridor model setup is shown in figure 4.9. This model setup however introduces the following additional possible sources of error.

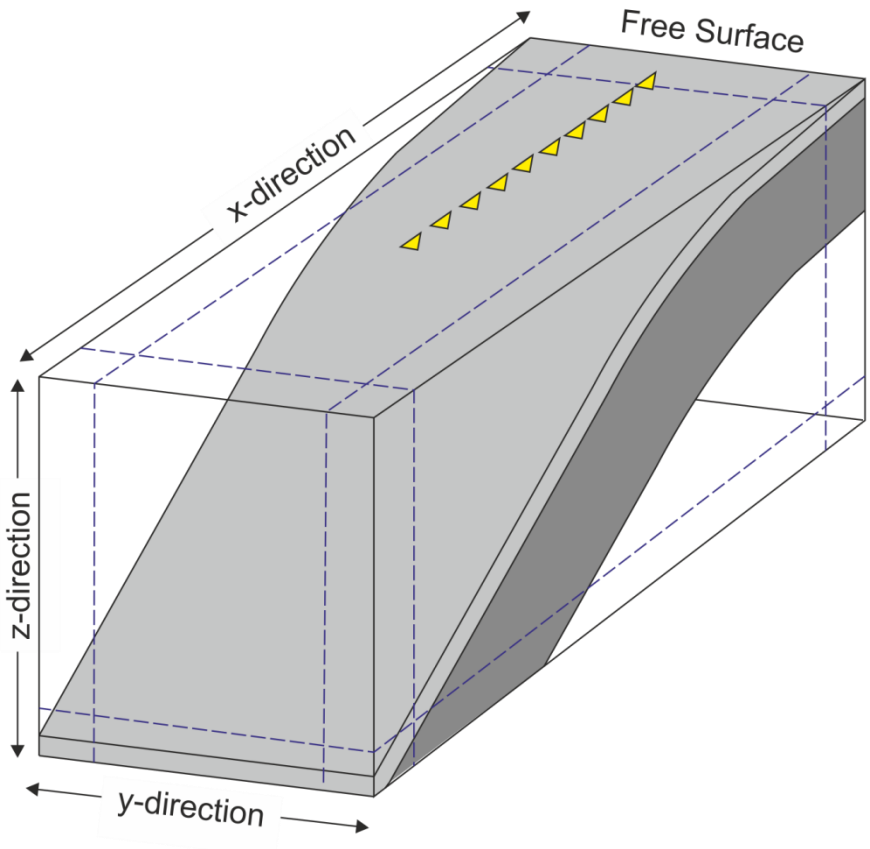

Figure 4.9 – 3D corridor model setup. Model dimensions in the x-direction and z-direction are slightly greater than the length of the modelled ray path, and event depth respectively. The model is as narrow as possible in the y-direction. The modelled high velocity slab and low velocity waveguide is shown in dark and light grey respectively. Blue dashed lines show the absorbing boundary layers, and the free surface at the top of the model is labeled. Yellow inverted triangles denote the approximate locations of the seismometers, equally spaced at the same y-offset as the source, close to the centre of the model.

1. Reflections from the model boundaries in the y-direction may affect the first few seconds of P-wave arrival
2. If the y-direction is of the same order of magnitude as that of the low frequency component of the wave field, then the lowest frequency may interact with the dampening model boundaries. This may affect both the velocity and the amplitude of the low frequency first arrivals

Both of these problems could potentially be overcome by making the model wider in the y-direction. This would however increase the computational cost of the model and so reduce the frequencies that can accurately be modelled on the HPC facilities that are currently available. In practice the first potential source of error is overcome by introducing an effective absorbing boundary on the y limits of the model.

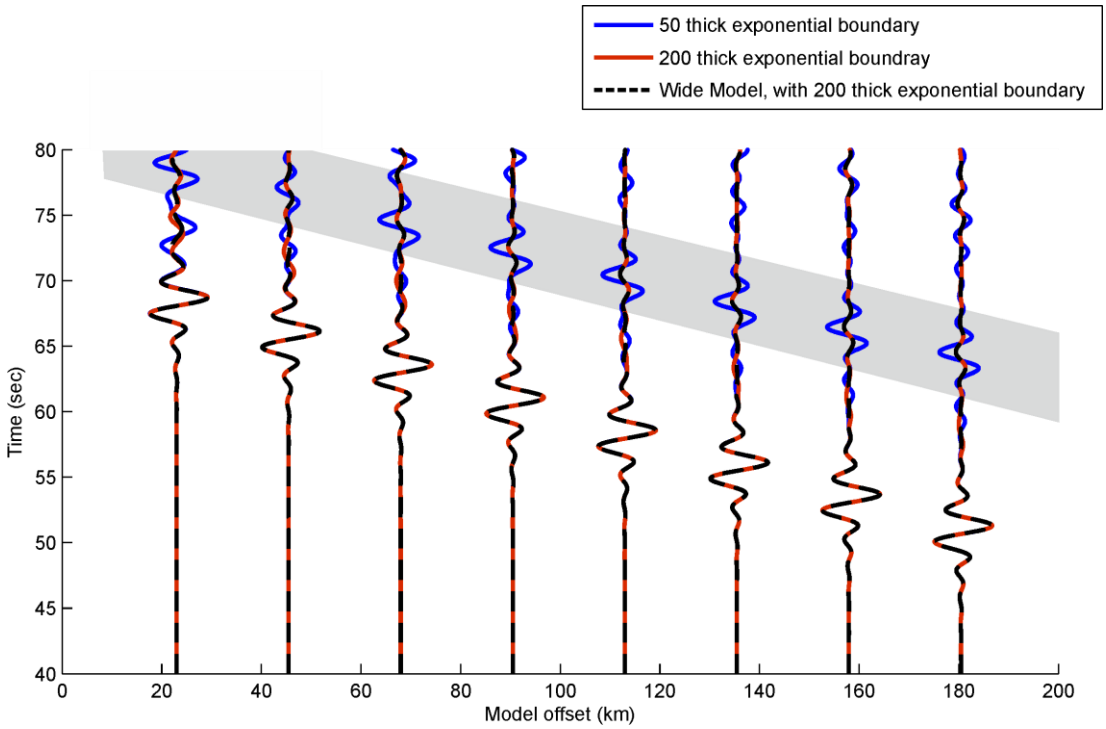

Figure 4.10 – Comparison of waveforms from 3D homogenous corridor models. Blue waveforms are from a 1728 node (259.2 km) wide corridor model with 50 node (7.5 km) thick exponential dampeners. The waveforms shown in red are from a 1728 node wide corridor model, with exponential dampeners that are 200 nodes (30 km) thick. This is benchmarked to a 3456 node (518.4 km) wide corridor model with 200 node exponential dampeners. Side reflections are highlighted in grey, and are seen most clearly as strong blue arrivals (e.g. at ~65 seconds at 180 km model offset, and ~72 seconds at 90 km offset).These models show that side reflections can be adequately reduced in amplitude by the exponential dampening boundary condition. Increasing the width of the corridor model does not affect the first motions, suggesting that the 1728 node wide corridor model is adequate for are up dip guided wave simulations.

Model Width	259.2 km	518.4 km
Dh	150	150
dt	0.009	0.009
No. of grid points in x-direction	4212	4212
No. of grid points in y-direction	1728	3456
No. of grid points in z-direction	2000	2000
Model Length in x (km)	631.8	631.8
Model Length in y (km)	259.2	518.4
Model Length in z (km)	300.0	300.0
No. of processors in x	18	18
No. of processors in y	8	16
No. of processors in z	10	10
KAus per job (Elastic)	~90.3	~180.6

Table 4.3: 3D model setup. Model setup is accurate to 2 Hz at subduction zone velocities. Cost of models in KAus based on model runs on Hector phase 3.

The width of the modelled corridor is determined by the need to keep the side reflections out of the time window that is being analysed. Figure 4.10 shows the waveforms produced by a homogenous corridor model. Increasing the width of the exponential boundary from 50 to 200 nodes thickness greatly reduces the amplitude of the side reflections. The amplitude of the side reflections in this setup is less than 10 % of the true signal.

To ensure that the time window analysed is not affected by the width of the corridor model we compare the 3D homogenous models with different widths in the y-direction. Comparisons between models that are 259.2 km (1728 nodes) and 518.4 km (3456 nodes) wide in the y-direction are shown in figure 4.10. As there is no difference in the first 5 seconds of arrival, and little difference thereafter, we conclude that no significant artefacts will be introduced due to the corridor width in the 259.2 km thick 3D corridor model when a 30 km (200 node) thick exponential boundary condition is used.

4.3 Summary

In this chapter a set of methods for measuring dispersed waveforms and comparing them to synthetic waveform have been introduced. By tightly constraining the first arrivals of the dispersed waveform, and also constraining the relative amplitudes of the P-wave coda the waveform is constrained more fully than in previous work. These methods can then be applied to dispersed waveforms observed in the subduction zone forearc, to give new insights into the WBZ structure associated with these events.

Part two

Guided Waves in Subducted Lithosphere

Chapter 5

Order of magnitude increase in subducted H_2O due to hydrated normal faults within the Wadati-Benioff zone

Abstract

It is widely proposed that the oceanic mantle is hydrated by outer-rise normal faults, and carries large amounts of water to the deep mantle. The extent of oceanic mantle hydration is however poorly constrained by existing observations, and is a major source of uncertainty in calculating the total water delivered to the mantle. Full waveform modelling of dispersed P-wave arrivals from events deep within the WBZ of Northern Japan shows that hydrated fault zone structures are present at intermediate depths. Analysis of the P-wave coda associated with events 5 – 35 km below the top of the slab gives an overall indication of the bulk hydration of the subducting oceanic mantle, and can be explained by 17.4 - 31.1 % serpentinisation. This suggests that a layer of up to 40 km thickness is 2.0 - 3.5 wt% hydrated, subducting 170.4 - 318.7 Tg/Myr of water per metre of arc beneath Northern Japan. This represents an order of magnitude increase in the estimated H_20 flux in this arc, and implies that over the age of the Earth up to 3.5 oceans of water could be subducted along the Kurile and Izu-Bonin arcs alone. These results offer the first direct measure of lower lithosphere hydration at intermediate depths, and show that re-gassing of the deep mantle is far more vigorous than has previously been suggested.

5.1 Introduction

Double Wadati-Benioff Zone (WBZ) seismicity has been observed across the globe (Brudzinski *et al.,* 2007), and it is widely thought that the lower plane of seismicity is

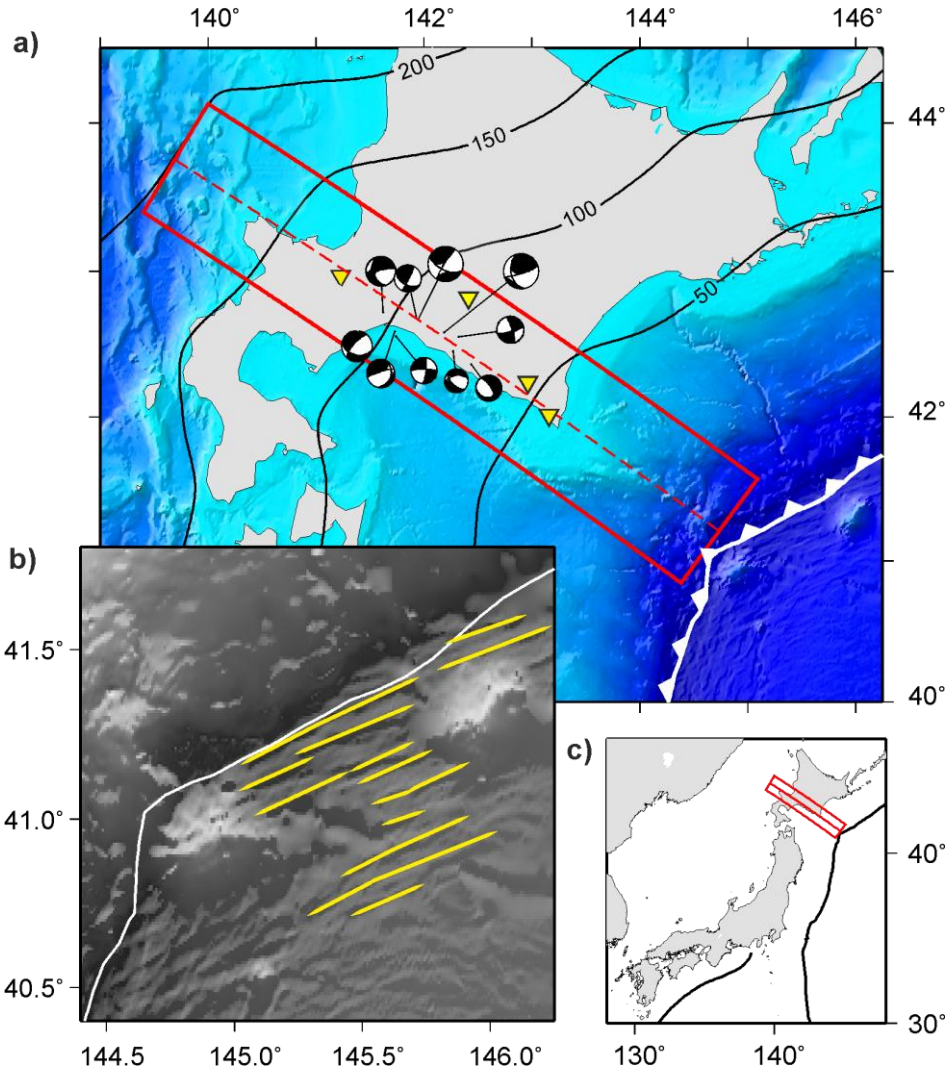

Figure 5.1 – Summary map. **a)** The focal mechanisms (black and white) of earthquakes used in the full waveform analysis, with the stations used shown by yellow triangles. **b)** Zoomed in image of outer rise fault scarps, highlighted in yellow in the Japan subduction zone trench. Bathymetry from Gebco08 model. **c)** Location map, red box shows the profile area described in this study.

associated with breakdown of hydrous minerals (e.g. Peacock & Wang, 1999; Hacker *et al.,* 2003b). Outer rise normal faulting has been proposed as a pathway for hydration of the oceanic lithosphere (e.g. Ranero *et al.,* 2003), and is apparent in many subduction zones across the globe due to the surface expression of fault scarps in the oceanic trench (figure 5.1). At several subduction zones the reactivation of outer rise normal faults at intermediate depths has been shown (e.g. Ranero *et al.,* 2005). In Central America the onset of outer rise faulting corresponds with a reduction in seismic velocity (Grevemeyer *et al.,* 2007), heat flow (Grevemeyer *et al.,* 2005) and resistivity (Worzewski *et al.,* 2011) of the

incoming plate and is interpreted as the onset of hydration and serpentinisation of the oceanic lithosphere. Geodynamic modelling suggests that bending and unbending of the subducted lithosphere causes a downward pressure gradient in the outer rise faults, forcing water into the deeper parts of the slab (Faccenda *et al.,* 2009; Faccenda *et al.,* 2012) and it is proposed that these hydrated faults may carry large amounts of water to the mantle (e.g. Iyer *et al.,* 2012).

The amount of water subducted globally in the crust and sediments is relatively well understood (van Keken *et al.,* 2011), but the overall extent of hydration due to normal faulting remains poorly constrained. Mantle lithosphere hydration due to normal faulting is potentially a major component of the global H_2O cycle, explaining the inferred hydrous transition zone (e.g. Lawrence & Wysession, 2006), with significant implications for the rate of convection (Hirth & Kohlstedt, 1996) and melt production (e.g. Hirschmann, 2006) in the deep mantle.

5.2 Dispersed P-wave arrivals

To investigate the hydrated structure of the slab mantle we analysed dispersed P-wave arrivals from events that occur well below the surface of the slab. The dispersion is noted at seismic stations in the forearc of Northern Japan, and is only observed at stations close to the trench. These events occur at between 100 and 150 km depth, and are 5 - 35 km below the slab surface. The dispersion is measured using a spectrogram as shown in figure 5.2a. The high frequency arrivals (> 2 Hz) are delayed by approximately 1.5 seconds relative to the low frequency arrivals (< 0.5 Hz). The relative delay of the higher frequencies is shown for 8 events in the lower WBZ in figure 5.2b. The associated spectrograms for 5 of these events are shown in figure 5.3.

Dispersive P-wave arrivals similar to these observations have been observed in Northern Japan, and subduction zones across the globe, from events occurring at depths of greater than 100 km (Abers, 2000; Abers, 2005; Martin *et al.*, 2003). The dispersion is attributed to a layer of low velocity oceanic crust that acts as a waveguide. High frequency (short wavelength) energy is retained and delayed in subducted low velocity oceanic crust, while lower frequency (long wavelength) seismic energy travels at the faster seismic velocities of the surrounding mantle. These dispersion observations however are all inferred to occur in

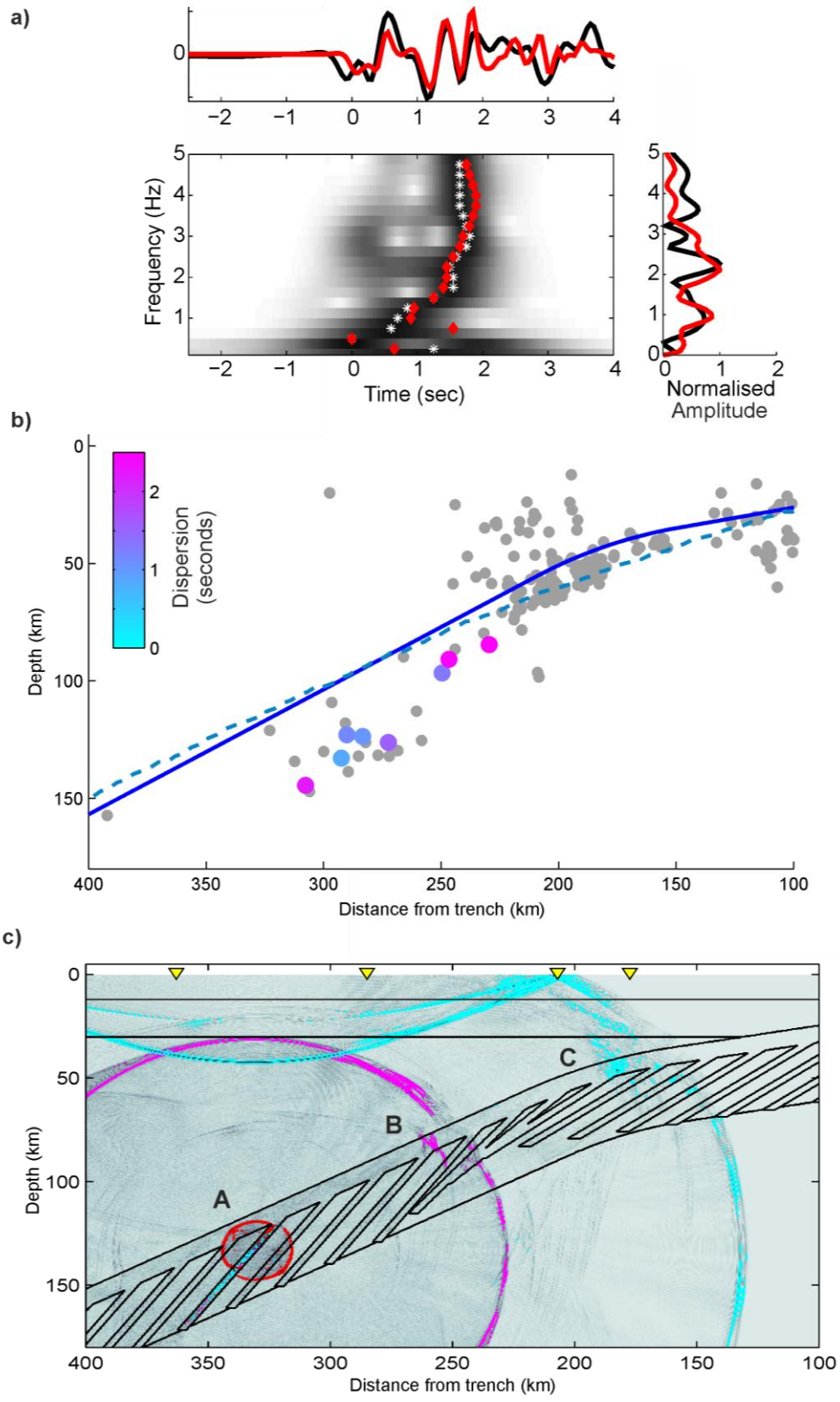
a)
Frequency (Hz)
Time (sec)
Normalised Amplitude
b)
Dispersion (seconds)
Depth (km)
Distance from trench (km)
c)
A
B
C
Depth (km)
Distance from trench (km)

Figure 5.2 – Dispersive waveform modelling. **a)** Waveform fit of dispersive P-wave arrival recorded at station ERM. The recorded waveform (black) is compared to the synthetic waveform (red) in a spectrogram (bottom left) and in the frequency domain (bottom right), allowing comparison of the full waveform < 2.5 Hz (top). **b)** The blue and pink events show the delay of the 2 Hz frequency band compared to the arrival of the 0.5 Hz frequency band for 8 events at depths of 70 - 150 km. Grey events show the background seismicity on the profile shown in figure 5.1. The modelled subduction interface and the slab1.0 model (Hayes *et al.,* 2012) are shown as a solid dark blue line, and dashed light blue line respectively. The dispersed events are well below both these slab models, and within the local double WBZ seismicity. **c)** Snapshots of the waveform model at 1, 12 and 24 seconds shown in red, pink, and light blue respectively. The high frequency energy from the source is trapped in the low velocity fault zone (A), before being transferred to the low velocity oceanic crust (B) and decoupling to be observed at the surface (C).

the upper plane of seismicity. For seismically slow crust to act as an effective waveguide the source must be on or near to the low velocity layer (LVL) (Martin *et al.* 2003; Martin & Rietbrock, 2005; Abers, 2005), although it has been shown that S-P conversions from sources very close to the crust may travel within the LVL as guided waves (Horleston & Helffrich, 2012). The events analysed here however occur well below the slab surface, implying that a layer of low velocity oceanic crustal material cannot explain the observed dispersive P-wave arrivals. Our modelling also shows that the presence of a lower low velocity zone as has been inferred by detailed tomographic studies of Northern Japan (Zhang *et al.,* 2004; Nakajima *et al.,* 2009) cannot explain the data. The geometry of this lower layer means that guided waves generated in this layer do not decouple deep enough to be seen at the surface. We also note that as these events do not occur in a single plane, it is unlikely that they can be described by a single low velocity layer.

We propose that events occurring deep in the slab with dispersive P-waveforms are explained by serpentinised outer rise normal faults that act as low velocity waveguides penetrating deep into the slab. We simulate the waveforms arising from these events occurring on a low velocity fault structure as shown in figure 5.2c. The low velocity fault zone retains high frequency energy from an event that occurs upon it, while low frequency energy is not retained and travels at the faster velocities of the surrounding cool slab material (A). The retained high frequency energy is then transferred to the low velocity oceanic crust and travels up dip in the crustal waveguide (B). This high frequency energy then decouples from the crustal waveguide due to the bend of the slab (C). Hence the dispersed arrivals are only seen at stations close to the trench where the delayed high frequency energy has decoupled from the crustal waveguide (Martin *et al.,* 2003).

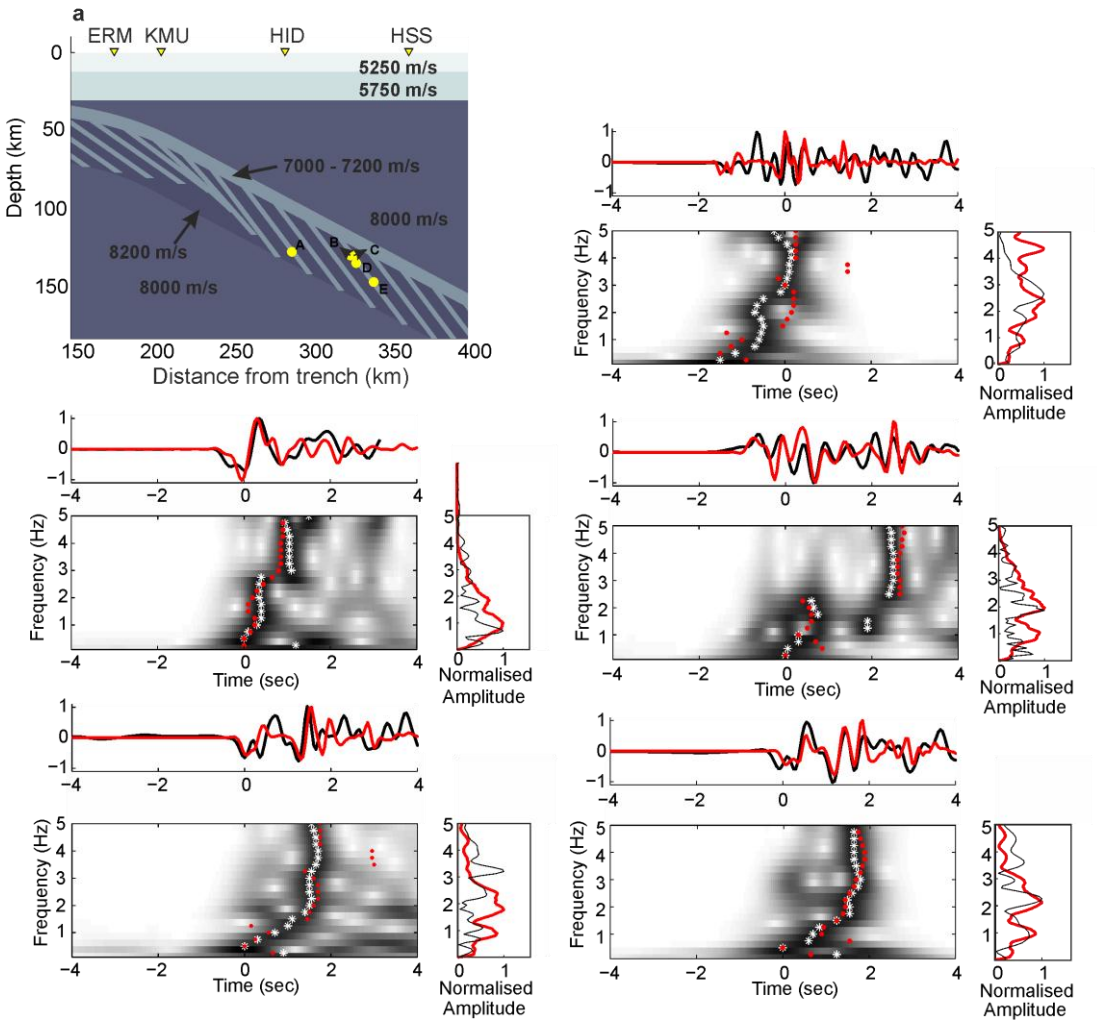

Figure 5.3 – Full waveform fits for five dispersive events observed in Northern Japan. **a)** Shows the location of the events with yellow circles, lettered A – E. The position of the stations used are shown by inverted yellow triangles. The modelled and observed waveforms shown are all recorded at the station ERM. The grey colour scale shows the velocity structure, and the velocities of different areas are labelled. **b)-f)** Shows the spectrogram (bottom left), displacement spectra (bottom right) and waveform (top) of each event recorded at the station ERM (black and white colours). Each of these waveforms is directly compared to the modelled waveform (red) as described in the main text.

Synthetic waveforms produced by our simulations are directly compared to the dispersive waveforms observed on the Japanese forearc as shown in figure 5.2a. The synthetic and observed spectrograms (bottom left) are compared to constrain the relative arrival time of different frequency bands. The displacement spectra of the synthetic and observed signal (bottom right) are matched to constrain the relative amplitude at different frequencies. Constraining the signal in these two ways means that the waveform (low pass filtered at 2.5 Hz) can be directly modelled (figure 5.2a).

This methodology is used to test a variety of velocity models, and the waveform fits for the five events modelled in this way are also shown in figure 5.3b-f. Our waveform modelling shows that the observed dispersions can be explained by a fault zone of 2 - 3 km width with a velocity of 7.0 - 7.2 km/s (12 - 15 % slower than the surrounding mantle material). Models outside this range of fault widths and velocities do not produce reasonable fitting waveforms. The modelled fault zones have an apparent dip of 25° to the slab surface (figure 5.3a). The apparent dip corresponds to a true dip of ~39° on a profile that is perpendicular to the scarp of the outer rise normal faults. This is similar to the fault angle that is seen for outer rise normal faulting and reactivated normal faults in studies of South and Central America (Ranero *et al.,* 2005).

While these observations provide a good constraint on the structure of individual serpentinized faults in the subducted slab, and confirm the link between intermediate depth seismicity and outer rise faulting these observations cannot be used to estimate the overall extent of slab hydration due to outer rise faulting.

5.3 P-wave coda analysis

To directly investigate the levels of hydration of the subducting mantle lithosphere we analyse the extended high frequency P-wave coda associated with WBZ events observed in the forearc. While only some events clearly show the characteristic dispersed first arrivals, all events of depth 100 - 150 km on this profile recorded at the station ERM between 2000 - 2010 are associated with an extended P-wave coda. Extended P-wave coda has previously been noted for much deeper events in Northern Japan (Furumura & Kennet, 2005). To quantify this observation we calculate the amplitude of the P-wave coda relative to the first arrival, using the method outlined in chapter 4. We observe that the magnitude of the high frequency P-wave coda reduces compared to the first arrivals with distance from the trench (figure 5. 4).

Full waveform models are used to assess the amount of coda produced by different models of slab mantle hydration. No coda is observed in synthetic waveforms based on velocity models that only have a single simple low velocity layer. Only weak coda are generated for models with several regularly spaced low velocity fault zones as used for the deterministic dispersion models for selected events. We therefore represent the hydrated fault zone structure as a random media described by a von Kármán function with varying average

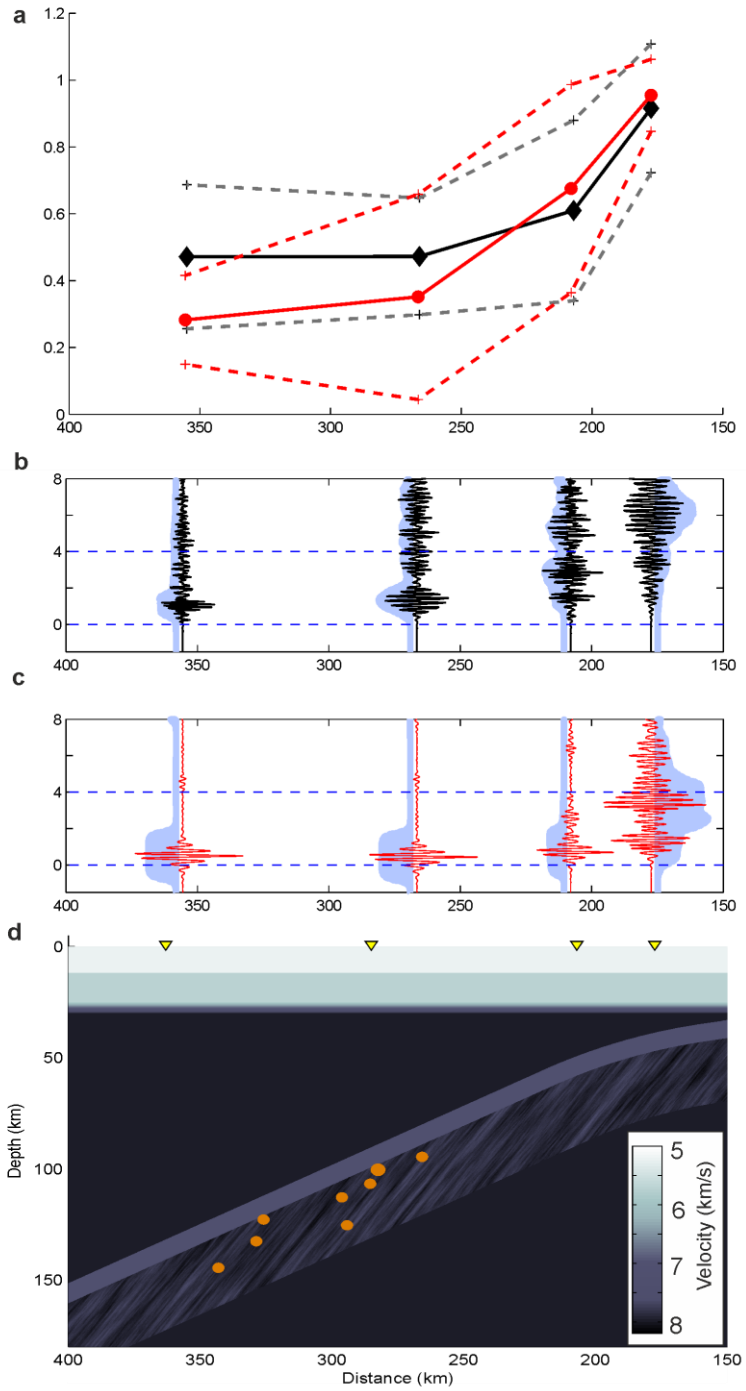

Figure 5.4 – Scattering analysis **a)** for all events with the observed coda decay (black) compared to the modelled coda decay (red). The plot shows the average coda ratio normalised to the maximum coda ratio for a given event. **b)** Observed high frequency (> 3.0 Hz) P-wave arrivals with extended coda (back) with the coda envelope plotted in light blue. **c)** Synthetic P-wave arrivals (high pass filtered at 3.0 Hz) from numerical model incorporating elongated random scatterers in the WBZ. **d)** Velocity model that produces the best fitting coda decay shown in figures above. The events for which extended coda is measured and modelled are shown by orange circles, with the stations at which the coda is observed by a yellow triangle.

velocity, size distribution, and degree of elongation. This stochastic model provides low velocity scatterers at a range of scale lengths, rather than the single scale length seen in the deterministic models used before. Previous work has attributed extended P-wave coda arrivals from deep subduction zone events in Northern Japan to scatterers elongated parallel to the slab (Furumura & Kennett, 2005), although there is no widely accepted geological interpretation for this structure.

We propose that this extended P-wave coda observed in this study can be explained by dipping low velocity normal fault structures that form a scattering media. The correlation length and aspect ratio of the fault zone scattering media is varied. Modelling shows that the coda decay is relatively insensitive to the shape of scatterer (figure 5.5). Other scattering models, such as scattering in the mantle wedge or over-riding crust cannot account for the observed extended P-wave coda (figure 5.6). The amplitude of the coda can only be reproduced where the source is directly in the scattering media, and so S to P conversions contribute to the strength of the P-wave coda. This gives further evidence that WBZ events deep within the slab are associated with low velocity hydrated scattering structure. Further modelling shows that scatterers elongated parallel to the slab, as proposed by Furumura & Kennett (2005), can describe the observed P-wave coda. The waveform modelling presented in this chapter shows that hydrated normal faults are present at these depths, so we therefore assert that dipping low velocity fault zone structures may be responsible for the observed P-wave coda. We also note that the dipping fault model produces a stronger P-wave coda than slab-parallel scatterers.

In summary our analysis shows that a wide range of scattering structures could potentially account for the observed coda decay, including elongate scatterers parallel to the dip of the slab (figure 5.5). Since elongated structures in the orientation of dipping faults produce the strongest coda, and correlate with dipping structures shown from guided wave dispersion, we propose that dipping fault zone structures cause the observed extended P-wave coda.

While the spatial coda decay along the profile is relatively insensitive to the orientation of the scattering structure, we show that the coda ratio is sensitive to the velocity contrast of the scattering media (figure 5.7). Average velocities for the slab mantle are tested in the range of velocities between 6.8 km/s (highly serpentinised peridotite) and 8.2 km/s (dry deep peridotite). The velocity of the scatterers varies so that the standard deviation from the average velocity is 1 %. An average velocity contrast of 8.03 km/s clearly does not

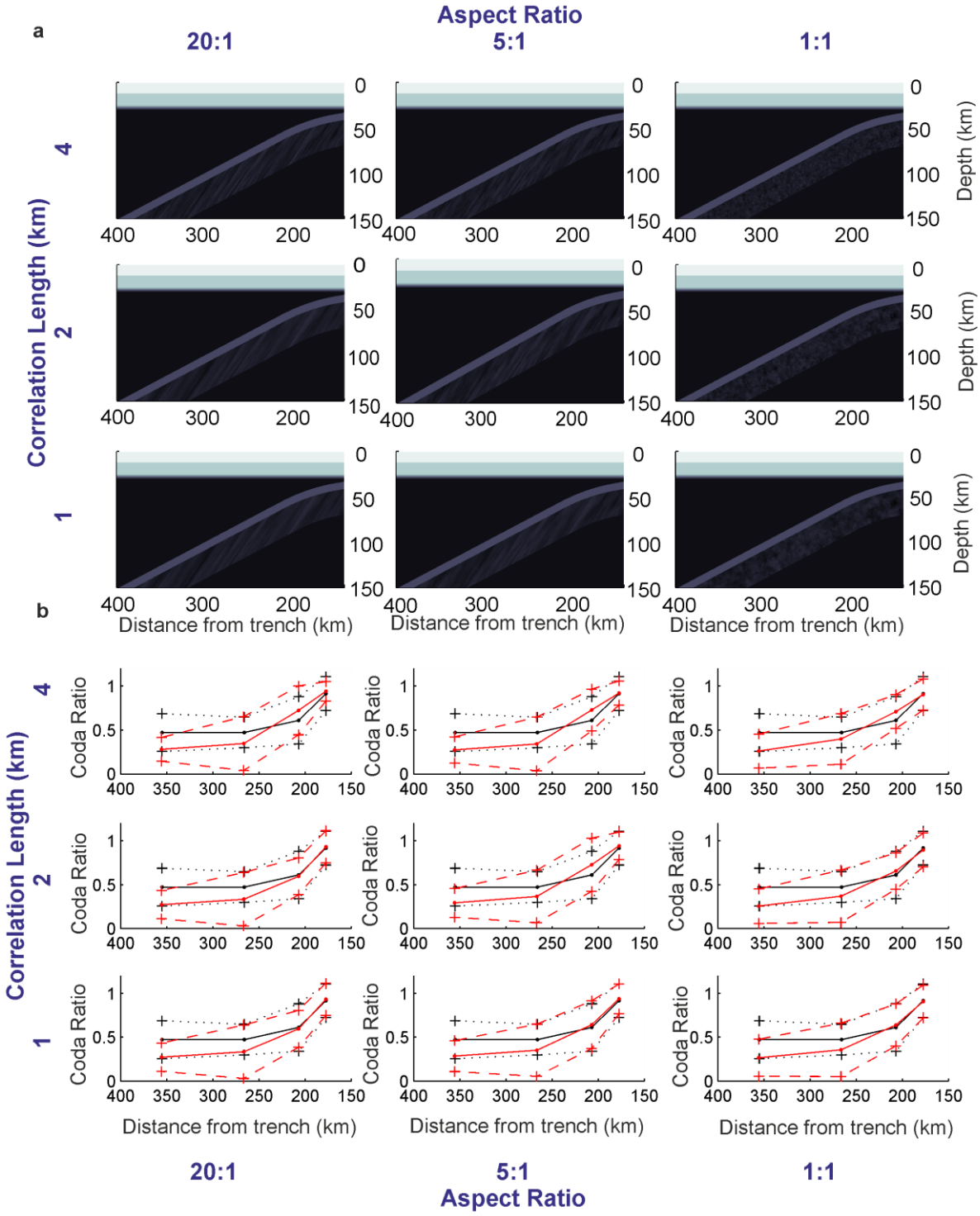

Figure 5.5 – Scattering model resolution. **a)** The velocity models used showing different correlation lengths and aspect ratios of scattering media. **b)** The decay in coda ratio for each of these models (red), compared to observed coda decay (black).

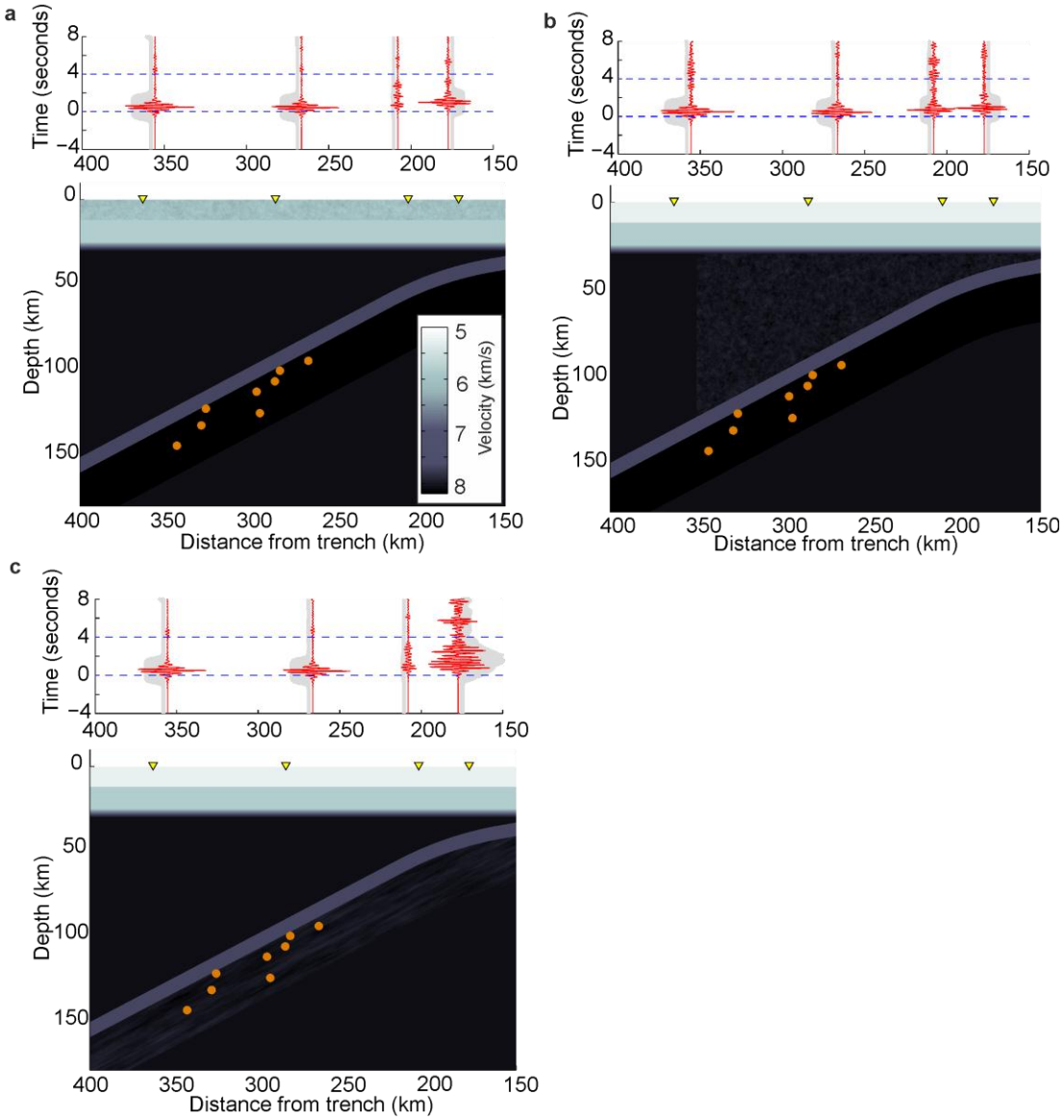

Figure 5.6 – Alternative scattering models. **a)** Shows a velocity model with scattering in the upper crust. The high passed (>3 Hz) waveforms shown in red above show that this model cannot explain the degree of coda that is produced. **b)** Scattering media in the mantle wedge does not produce significant coda either. **c)** Scatterers parallel to the dip of the slab can account for the coda (e.g. Furumura & Kennett, 2005) but we propose that dipping fault zone structures are a better candidate.

describe the coda decay close to the trench adequately, while an average velocity of 7.5 km/s produces a coda decay of larger amplitude.

Modelling a range of scattering media average velocities shows that the average velocity for the WBZ scattering media is 7.76 +/- 0.18 km/s. Higher or lower average velocities do not account for the observed decay in coda amplitude.

5.4 Calculating the degree of slab mantle serpentinisation and hydration

This average velocity allows the degree of serpentinisation to be calculated if the velocity of serpentinite and mantle periodite material is known at these temperature and pressure conditions. The velocity and hydration of serpentinite used in the calculations of bulk serpentinisation are calculated using the *Subduction Factory 4* excel macro (Hacker & Abers, 2004). Pressure conditions are calculated using the densities of the PREM model and temperature conditions are calculated using a 2-dimensional finite element model (Fry, 2010) which gives similar temperatures to published profiles of Northern Japan (e.g. Hacker *et al.,* 2003b, Syracuse *et al.,* 2010). An average velocity of 8.2 km/s is assumed for the mantle peridotite based on high resolution tomography of the area (Nakajima, *et al.,* 2009) and numbers given in petrological modelling (Connolly & Kerrick, 2002).

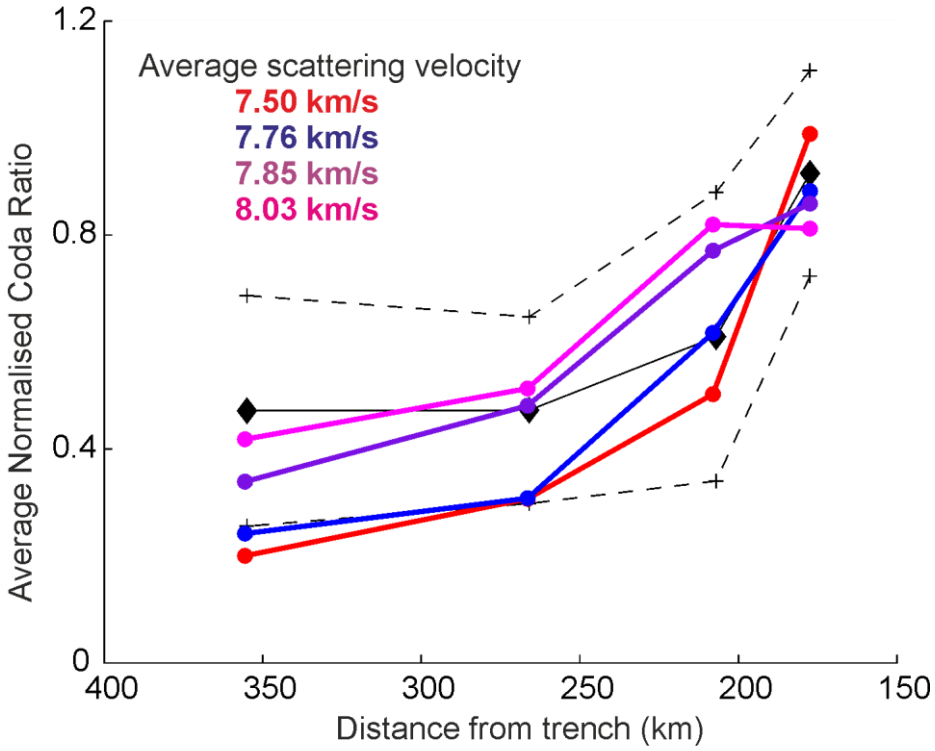

Figure 5.7 – Velocity sensitivity of scattering media. Coda ratio decay is show for models with an average velocity of 7.5, 7.76, 7.85 and 8.03 in red, blue, purple and pink respectively. The lowest average velocity (red) over exaggerate the decay, while the highest average velocity(blue) does not adequately describe the decay close to the trench. Average velocities in the range of 7.68 – 7.85 km/s describe the decay within error.

At the pressure (1.5 – 4.8 GPa) and temperature (250 - 500^{o}c) conditions present in the slab mantle beneath Northern Japan we calculate that serpentinite has a velocity of 6.19 - 6.51 km/s. Given that the average velocity of the slab mantle is 7.625 - 7.85 km/s this gives a range of serpentinisation values of between 17.4 - 31.1%. Assuming the wt% of H_20 of serpentinite at these pressure-temperature conditions is 11.3 % (Hacker & Abers, 2004), this translates to an overall slab mantle hydration of 57 - 107 kg/m3. The subduction rate at this arc is approximately 7.5 cm/yr (van Keken *et al.,* 2011). This implies that 170.4 - 318.7 Tg/Myr of water per metre of trench is subducted at this trench. Taken with the estimate of van Keken *et al.* (2011) for total water subducted in the upper slab (i.e. in the oceanic crust and sediments) this gives an overall amount of 191.9 - 340.2 Tg/Myr of water per metre of trench subducted beneath Northern Japan. The slab mantle hydration accounts for 89 - 94% of this overall budget. If this amount is extrapolated along the Kurile and Izu-Bonin arcs where oceanic lithosphere of > 120 Ma is subducting (approximately 3380 km), we show that this system could subduct up to 3.5 oceans over the age of the Earth. This suggests hydration of the lower lithosphere has a major role to play in the re-gassing of the lower mantle.

5.5 Discussion

Based on the analysis of dispersive P-wave arrivals and high frequency P-wave coda we suggest that the velocity structures in the lower subducting lithosphere are serpentinized peridotite along dipping faults of various scale length. Serpentinite has been shown to be stable at the pressure and temperature conditions found at this depth (Hacker *et al.,* 2003a) and has a predicted P-wave velocity of 6.19 - 6.51 km/s, and a hydration of 11.3 wt% H_20 (Hacker & Abers, 2004).

The dispersion observations presented above provide direct seismic evidence of the presence of serpentinized normal fault structures at depth, and confirm that lower plane WBZ seismicity is associated with these hydrous mineral assemblages. The measured velocity contrast of these faults would imply that they are 50 - 71% serpentinised. These observations suggest that outer rise normal faults are a viable pathway for deep slab hydration.

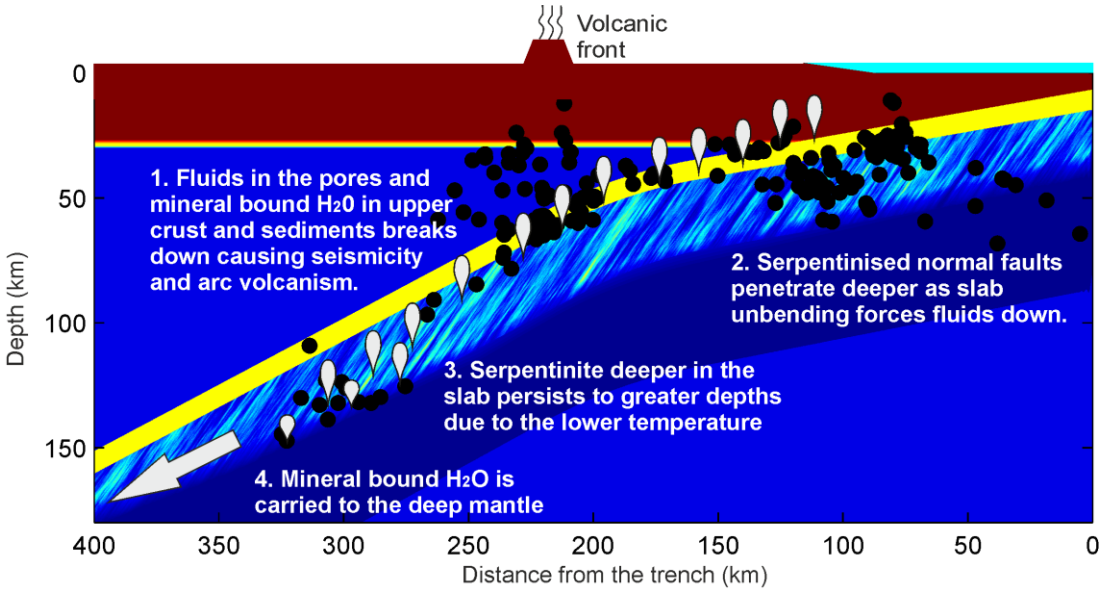

Figure 5.8 – Summary of subduction zone structure inferred for waveform modelling of dispersed P-wave arrivals. Hydration of the slab mantle is described by a von Kármán function, which provides large scale elongate structures representing the normal fault structures inferred. Smaller scale structures are required to provide observed P-wave coda. Fault depth increase with distance from the outer rise due to downward forcing of fluids Faccenda *et al.* (2009; 2012). Water is released from the slab mantle at much greater depths than it is released from the sediments and oceanic crust. As much as 35 % of the slab mantle hydration may be delivered to the deep mantle by a slab of approximately this age and convergence rate (Rüpke *et al.,* 2004). The depth of penetration of these hydrated fault zone structures is controlled by the temperature at which serpentinite is stable. As the slab is heated at depth the stability field of serpentinite becomes restricted to the slabs cool core.

The scattering models used to simulate the extended P-wave coda give a better constraint on the overall low velocity structure, and hence the hydration of the subducted lithosphere. Using the velocities for serpentinite calculated above we estimate that the mantle lithosphere is 17.4 - 31.1% serpentinised. Given the water content of serpentinite at these pressure and temperature conditions (Hacker & Abers, 2004) this would give an overall hydration of the mantle lithosphere as 2.0 - 3.5 wt% H_20.

The scattering media is interpreted as a hydrated fault zone structure related to WBZ seismicity and therefore we assume that the depth extent of the scattering media in the slab is defined by the thickness of the WBZ beneath Northern Japan (~40 km) (figure 5.8). This would translate to 170.4 - 318.7 Tg/ Myr of water per metre of arc being subducted in the mantle lithosphere at the Hokkaido trench. This represents an order of magnitude

Reference	Description	H_2O flux due to mantle lithosphere (Tg/Myr/m)
Rüpke *et al.* (2004)	120 Myr plate subducting at 6cm/yr	22.8
van Keken *et al.* (2011)	Assuming 2 wt% serpentinisation of 2km thick layer of mantle lithosphere	9.6
Iyer *et al.* (2012)	Extrapolating the inference from South and Central America to a Japan subduction zone conditions	60.0 – 187.5
This study		170.4 - 318.7

Table 5.1 – Summary of H_2O transported in the hydrated mantle lithosphere during inferred from this study and compared to the values from previous studies.

increase in the amount of water predicted to be subducted by earlier models (van Keken *et al.,* 2011; Rüpke *et al.,* 2004) (see table 5.1).

5.6 Conclusions

We have shown that serpentinized normal faults are present at 50 – 150 km depth, and are directly linked to lower plane WBZ seismicity. This suggests that the lower plane of WBZ may be associated with the breakdown of serpentinite as suggested by Peacock (2001).

Additionally, we have quantified the volume of mineral bound H_20 in the mantle lithosphere due to hydration from outer rise faulting. We show that the mantle lithosphere is the most significant contributor to subducted water, transporting more than ten times as much water as the oceanic crust and sediments put together. As the mantle lithosphere is the major contributor of water to the deep mantle (Rüpke *et al.,* 2004) much of this water may be carried beyond the volcanic arc, potentially explaining seismically inferred high water content in the mantle transition zone (e.g. Lawrence & Wysession, 2006).

While constraining the amount of water carried by the oceanic mantle in other subduction zones is important to ultimately understand the true amount of water subducted globally over the Earth's history, extrapolating the high volumes of water subducting here to the globe suggests that much more water is recycled to the mantle through subduction than previously thought. These high volumes of deeply subducted water have significant

implications for the rate of convection (e.g. Hirth & Kohlstedt, 1996) and melt production (e.g. Hirschmann, 2006) in the deep mantle. This may not only explain the Earth's inferred 'missing water' (Jacobsen & van der Lee, 2006) but also affect our understanding of how plate tectonic mode convection and continental crust formation developed on Earth.

Chapter 6

Down Dip Velocity Changes in Subducted Oceanic Crust beneath Northern Japan – Insights from Guided Waves

Abstract

Dispersed P-wave arrivals observed in the subduction zone forearc of Northern Japan suggest that low velocity subducted oceanic crustal waveguide persists to depths of at least 220 km. First arrivals from events at 150 – 220 km depth show that the velocity contrast of the waveguide reduces with depth. High frequency energy (> 2 Hz) is retained and delayed by the low velocity crustal waveguide while the lower frequency energy (< 0.5 Hz) travels at faster velocities of the surrounding mantle material. The guided wave energy then decouples from the low velocity crustal waveguide due to the bend of the slab and is seen at the surface 1 – 2 seconds after the low frequency arrival. Dispersive P-wave arrivals from WBZ earthquakes at 150 – 220 km depth are directly compared to synthetic waveforms produced by 2D and 3D full waveform finite difference simulations. By comparing both the spectrogram and the velocity spectra of the observed and synthetic waveforms we are able to fully constrain the dispersive waveform, and so directly compare the low pass filtered observed and synthetic waveforms. Using this full waveform modelling technique we are able to tightly constrain the velocity structures that cause the observed guided wave dispersion. Resolution tests using 2D elastic waveform simulations show that the dispersion can be accounted for by a 6 – 8 km thick low velocity oceanic crust, with a velocity contrast that varies with depth. The velocities inferred for this variable low velocity oceanic crust can be explained by lawsonite bearing assemblages, and suggest that low velocity minerals may persist to greater depth than previously thought. 2D simulations are benchmarked to 3D full waveform simulations and show that the structures inferred by the 2D approximation produce similar dispersion in 3D. 2D visco elastic simulations show that including elevated attenuation in the mantle wedge can improve the fit of the dispersed waveform. Elevated attenuation in the LVL can however be ruled out.

6.1 Introduction

Low velocity layers (LVL) at the top of the slab at intermediate depths have been observed at many subduction zones. In Northern Japan these low velocity structures have been inferred by a number of seismic observations such as guided wave dispersion (e.g. Abers, 2000; 2005), converted seismic phases (e.g. Matsubara *et al.,* 1986; Kawakatsu & Watada, 2007) and high resolution seismic tomographies (e.g. Nakajima *et al.,* 2009). It is thought that this LVL consists of hydrous basaltic oceanic crust (e.g. Helffrich, 1996) that becomes less seismically distinct as the crust dehydrates, eventually leading to the lawsonite-eclogite transformation after which the oceanic crust is no longer seismically distinguishable from the surrounding mantle material (e.g. Connolly & Kerrick, 2002; Hacker *et al.,* 2003a).

The breakdown of low velocity hydrous mineral assemblages is also associated with the occurrence of Wadati-Benioff zone (WBZ) seismicity. High frequency seismic energy from earthquakes that occur within the low velocity structure is retained through total internal reflections at the top and bottom of the LVL, while lower frequency energy travels at the faster velocities of the surrounding material. The high frequency guided wave is therefore delayed, causing a characteristic dispersion that is observed at many subduction zones (e.g. Abers, 2000; Martin *et al.,* 2003). Guided wave dispersion is then seen in the forearc as the high frequency energy decouples from the low velocity crustal waveguide due to the bend of the slab (Martin *et al.,* 2003). Arrivals from these intermediate depth earthquakes are also associated with an extended P-wave coda which has been noted in Northern Japan (Furumura & Kennet 2005; Garth & Rietbrock, 2014) and Tonga (Savage, 2012) which are associated with low velocity scatterers in the slab mantle. It is proposed that this extended P-wave coda is due to hydrated outer rise normal faults that act as seismic scatterers (Savage, 2012; Garth & Rietbrock 2014).

As guided waves spend most of their ray path interacting with the low velocity oceanic crust they have the potential to tell us a large amount about the seismic properties of the subducted crust. Here we present dispersive arrivals from WBZ seismicity that occurs at 150 - 220 km depth, observed in the forearc of Northern Japan. We show that the dispersion observed can be caused by a LVL at the top of the slab, and investigate the sensitivity of guided wave dispersion from events of different depths to down dip velocity changes within the LVL. We also use visco-elastic full waveform simulations to investigate the effect of elevated attenuation in the subduction zone system on guided wave observations.

Synthetic waveforms are produced using two dimensional (2D) waveform models that are benchmarked to three dimensional (3D) models of guided wave propagation.

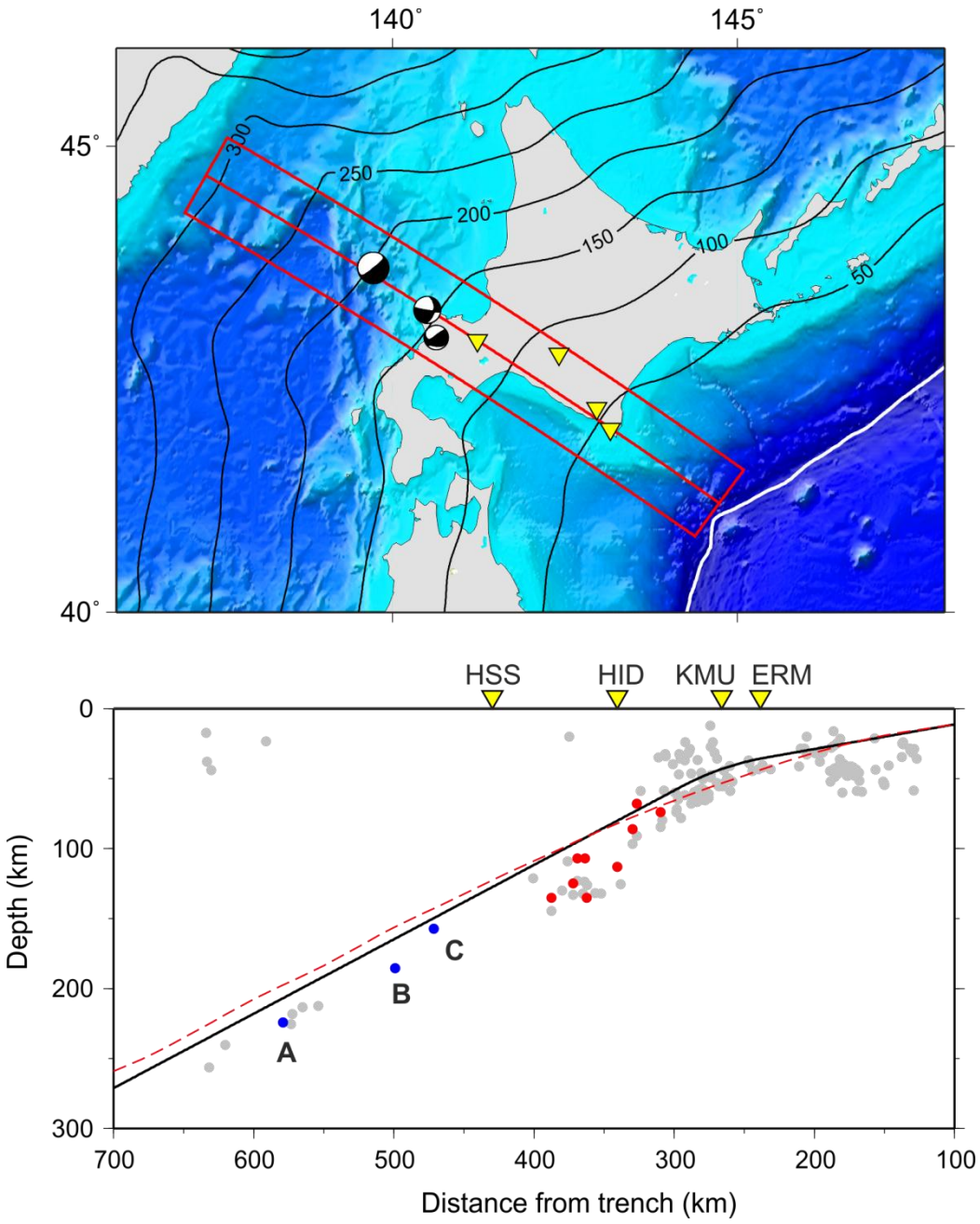

Figure 6.1 – Map and profile. **a)** Stations locations shown in yellow. The profile and the profile area are red. Slab contours shown in black are from *slab1.0* (Hayes *et al.,* 2012). White line shows the position of the trench. **b)** Seismicity from JMA catalogue is shown in grey. Red circles show the intermediate depth seismicity that is associated with hydrated fault zone presented by Garth & Rietbrock (2014). Blue circles show the upper plane WBZ events seen at 150 – 220 km depth that are analysed in this paper. The dashed red line shows *slab1.0* model for the centre of the profile shown. Black line shows model used in the waveform simulations.

6.2 Guided Wave Observations

It has previously been noted that arrivals from intermediate depth events in Northern Japan observed at stations close to the Hokkaido trench are dispersive (e.g. Abers, 2000; Furumura & Kennett, 2005). Dispersive arrivals have also been seen from events occurring well below the slab surface at depths of less than 150 km (Garth & Rietbrock, 2014). In this study arrivals from WBZ events at depths greater than 150 km occurring on the profile shown in figure 6.1 are observed at stations along this profile in the forearc of Northern Japan. The profile consists of broadband stations from the Global Seismic Network (GSN), (station ERM) as well as broadband stations from the Japanese F-net array (stations KMU, HSS and HID).

The background seismicity from the Japan Meteorological Agency (JMA) seismic catalogue is shown in grey in figure 6.1b. Events in the depth range of 150 - 250 km, that are clearly recorded at the station ERM are analysed. Events in this depth range that are not analysed are either too low magnitude to be clearly recorded at ERM, or occurred while the station ERM was offline.

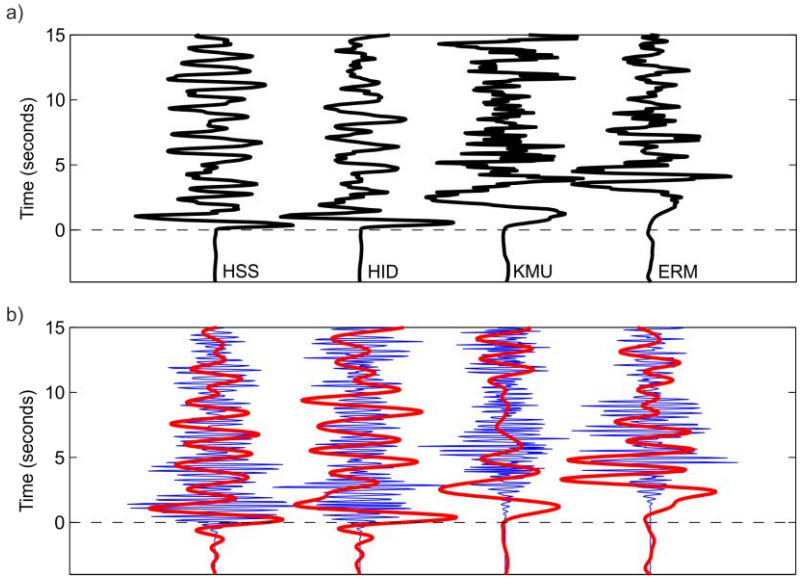

Figure 6.2 – Dispersive arrival observed at GSN and F-net stations on the profile shown in figure 1. **a)** The unfiltered arrivals shown in black. **b)** The signal high pass filter at > 2.5 Hz (blue) and low pass filtered at < 0.75 Hz (red).

The arrivals from the intermediate depth event labelled A in figure 6.1 are shown for all stations on this profile in figure 6.2. Dispersion is seen most clearly at the stations that are closest to the trench (i.e. ERM and KMU). Low frequency energy that is not retained in the low velocity waveguide arrives 1 - 2 seconds before the high frequency guided wave energy that has decoupled from the crustal waveguide due to the bend of the slab. The high and low pass filtered waveforms recorded at these stations (shown in figure 6.2b) clearly indicate that the low frequency arrival is earlier in comparison to the high frequency arrival. Further from the trench, un-dispersed arrivals are seen, as waves arriving at these stations have spent minimal time interacting with the low velocity waveguide.

6.3 Modelling Guided Waveforms

The interaction of dispersed waveforms observed at the surface with the waveguide is complex. We therefore use full waveform modelling to simulate the dispersed arrivals that arise from subduction zone waveguide structures.

Simulations of smaller scale seismic waveguides such as fault zones have shown that a number of key parameters can trade off with each other; i.e. several different waveguide structures can give approximately the same waveforms. Theses parameters include waveguide velocity contrast, width, position of the source within the waveguide, and attenuation characteristics of the waveguide (e.g. Ben-Zion *et al.,* 1999). These trade-offs may also apply to larger scale waveguides such as subduction zone waveguides and therefore must be understood in order to accurately interpret the observed arrivals. By modelling the full waveform we attempt to reduce these trade-offs.

6.3.1 Model setup

Synthetic waveforms are produced using SOFI 2D and 3D (Bohlen, 2002), which implements the staggered grid velocity-stress finite difference (FD) technique described in chapter 3.Modelling is mostly carried out using elastic 2D models which have a relatively low computational cost. These 2D simulations are then benchmarked to the far more computationally expensive 3D simulations. Elevated attenuation in the subduction zone is approximated using 2D visco-elastic FD models. Attenuation is approximated using two Maxwell bodies in parallel with a spring (e.g. Emmerich & Korn 1987; Bohlen, 2002) as described in Chapter 3. Both the 2D and 3D models are run on multiple processors on the UK national supercomputer HECTOR.

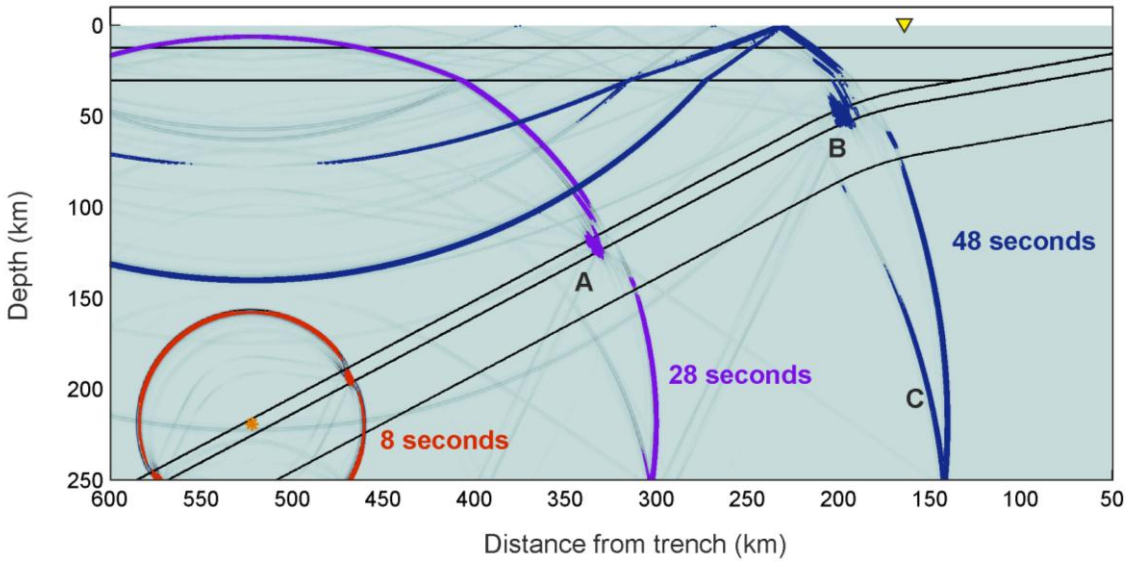

Figure 6.3 – Snapshots of waveforms produced from an explosive source at the optimum position for event A. Waveform is show at 8, 28, and 48 seconds in red, purple and blue respectively. The velocity model boundaries are shown in black, and the source position is shown by the orange star. The position of the station ERM is shown by the yellow triangle. The high frequency guided wave is shown at **A,** and decouples from the low velocity wave guide due to the bend of the slab at **B.** Side reflections shown at **C** arrive well after the first arrival.

The velocity model used in the FD simulations is informed by high resolution tomography of the subducting slab beneath Northern Japan (e.g. Nakajima *et al.,* 2009; Zhang *et al.,* 2004). The attenuation characteristics are based on the attenuation tomography of Tsumura *et al.,* (2000). These tomographic studies give reasonable values for the velocities and quality factor (Q) of the surrounding mantle and overriding crust. However the characteristics of the subduction zone low velocity crustal waveguide at depth are not resolved by these studies. The velocity and Q of the waveguide structure are therefore constrained by a series of parameter studies and comparison of the resulting synthetic waveforms with the observed waveforms.

The point at which the guided wave decouples from the subduction zone waveguide is affected by the bend of the slab (e.g. Martin & Rietbrock, 2006), therefore the geometry of the slab must be carefully constrained. The slab geometry is informed from *slab1.0*, the global catalogue of slab geometries of Hayes *et al.,* (2012) as well as local seismicity from the JMA catalogue. *Slab1.0* is particularly well constrained close to the oceanic crustal interface and so informs the model used at shallow depths. At greater depths the slab geometry is informed by the JMA catalogue seismicity which consistently plot below the *slab1.0* model. At these depths *slab1.0* is based on hypocentres from global earthquake

catalogues. Local catalogues generally plot the WBZ deeper due to the faster local velocity models that are used for the earthquake location (e.g. Syracuse & Abers, 2006). A comparison of *slab1.0*, the JMA catalogue seismicity and the model used in this study is shown in figure 6.1b. The velocity model used is show in figure 6.3, along with snapshots of the wavefield as the guided wave travels up dip.

6.3.2 Constraining Guided Waveforms

The synthetic waveforms are directly compared to the recorded waveforms. The FD model setup used is accurate to 5 Hz at the velocities that are considered. An explosive source is excited in the waveform simulation with a spike source, to give a full waveform spectrum. The synthetic waveforms are then low pass filtered with a zero phase second order Butterworth filter to simulate the source corner frequency. The source corner frequency applied is between 2 – 4 Hz, and is dependent on the magnitude of the event being considered.

The dispersive waveform is analysed at the station closest to the trench (ERM) where dispersion due to the decoupled guided wave is observed most clearly. The body wave dispersion is constrained using a spectrogram as proposed by Abers (2000; 2005). The waveform is also constrained in the frequency domain using the velocity spectra of the signal as proposed by Martin *et al.,* (2003), as it has been show that the velocity spectra of the signal is sensitive to the waveguide structure (e.g. Martin & Rietbrock, 2006). Combining these two approaches allows us to tightly constrain the waveguide structure, and reduce potential trade-offs between waveguide parameters such as width and velocity contrast. We show that if the arrivals are constrained in these two ways then the low passed waveform can be directly compared. This method of constraining the dispersive arrivals allows a range of waveguide parameters to be tested.

6.3.3 Calculating the combined misfit

In order for the waveform match to be quantitively assessed we calculate the misfit between the synthetic waveforms and the waveforms recorded at the station ERM. As has been discussed we constrain the guided waveform using several approaches to reduce the trade-offs between guided wave velocity, width and source position. Therefore, we calculate the misfit between the observed and synthetic waveforms for the spectrogram, velocity spectra, and the low pass filtered waveform and then calculated a combined misfit. The combined misfit is calculated with a 50 % weight to the spectrogram and 33.3 % velocity spectrum normalised misfit, and a 16.6 % weight to the normalised waveform

misfit. This is done for each of the LVL velocity models that are tested to give a range of possible LVL parameters. An example of the spectrogram, velocity spectrum, waveform and combined misfit for event A is shown in figure 6.4.

6.4 Determining Waveguide Velocity Structure

Dispersed arrivals are sensitive to velocity and width of the waveguide as well as the position of the source within the waveguide. These features of the subduction zone waveguide are therefore varied in a parameter study to constrain its structure.

The velocity and width of the waveguide control the amount of time a trapped wave spends in the waveguide, and therefore these two parameters trade off with each other. In subduction zone setting some of these trade-offs can however be minimised. For instance, the velocity of the mantle and subducting lithosphere are well constrained by tomographic studies. The range of possible waveguide velocity contrasts, and therefore waveguide velocities is reduced. The number of viable waveguide velocities and width combinations is also reduced by considering both the relative delay, and the relative amplitude of a given frequency using the method described in section 6.3.2.

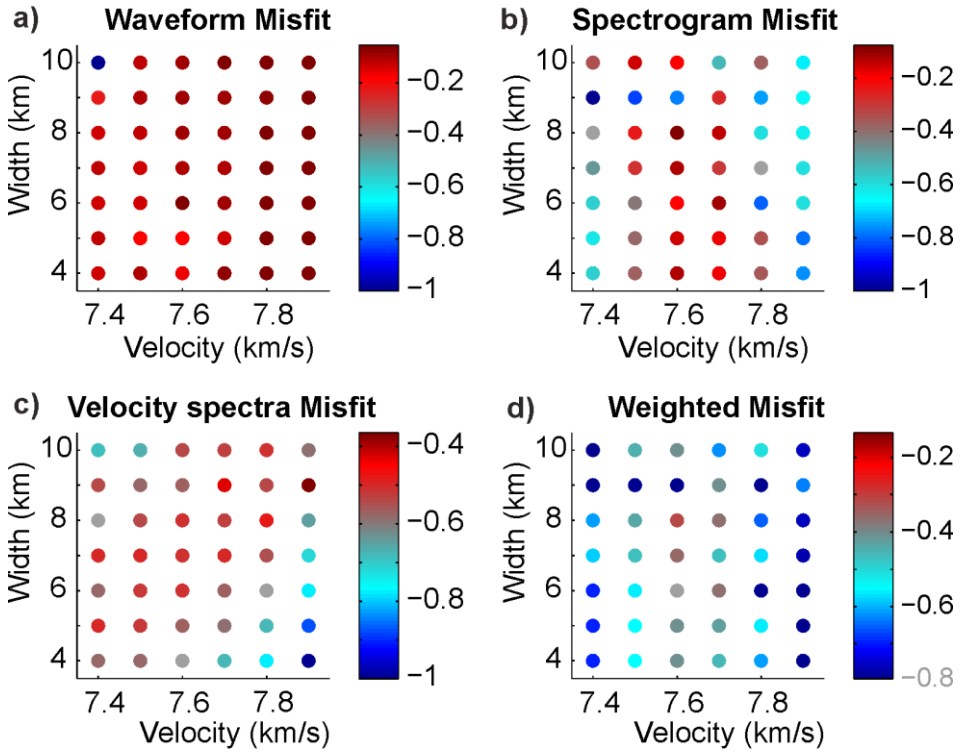

Figure 6.4 –Misfit between synthetic waveforms and waveforms recorded at the station ERM for a range of low velocity layer models. The misfit is shown **a)** for the low pass filtered waveform **b)** the spectrogram **c)** the velocity spectra and **d)** shows the weighted misfit, calculated as outlined in section 6.3.3.

The spectrogram is most sensitive to the velocity contrast of the waveguide, as this controls the overall delay of the higher frequencies. The spectrogram is however much less sensitive to the width of the waveguide, as is demonstrated in figure 6.4b. The relative amplitudes of different frequencies in the velocity spectra of the dispersed signal are sensitive to both the width and the velocity of the waveguide. Therefore there is a trade-off between the velocity and width of LVL that fit the velocity spectra well. The waveform misfit is not as sensitive to the waveguide structure overall, though the misfit is higher for the extremes of the model space tested. Figure 6.4d shows that combining the misfit of these different plots allows both the velocity and width to be well constrained.

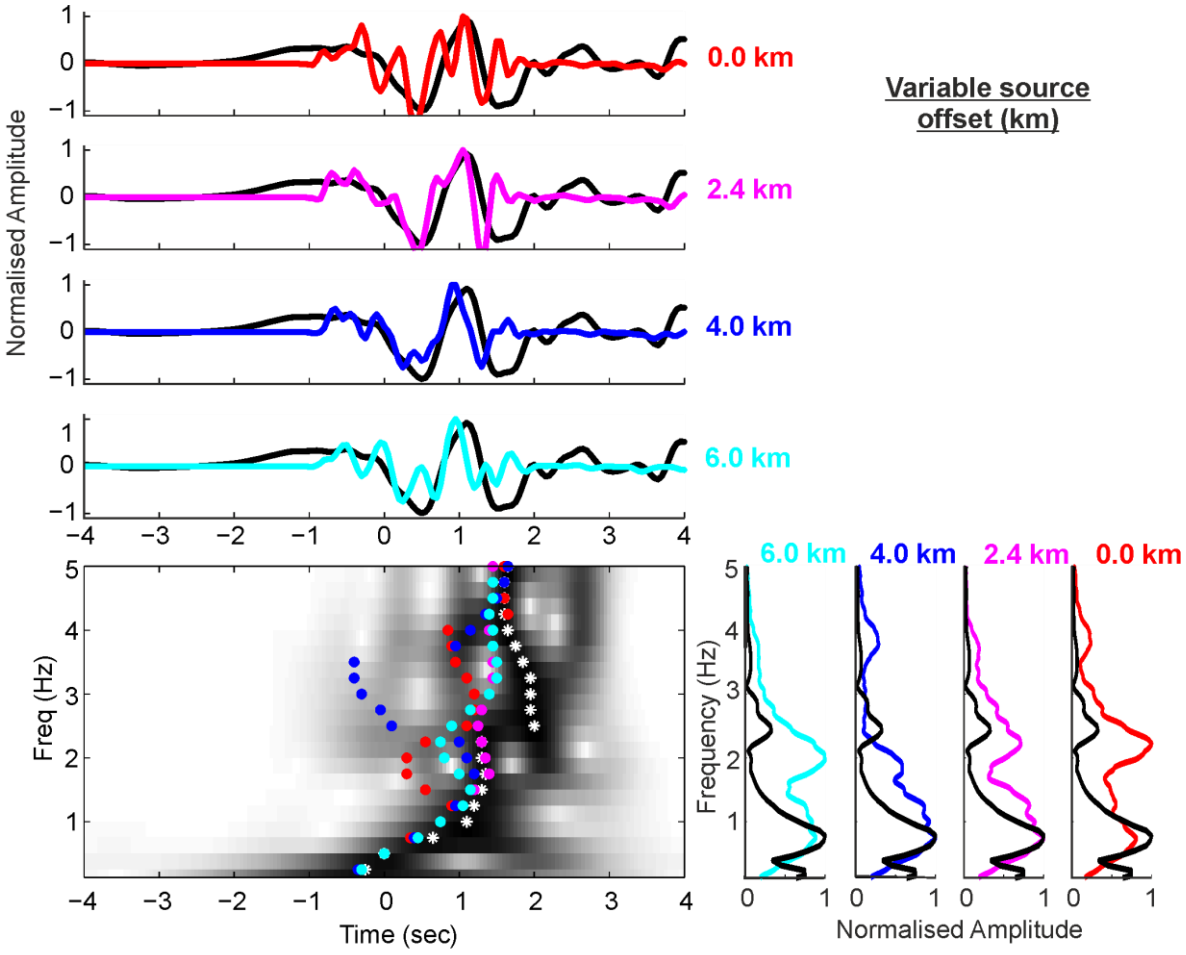

Figure 6.5 – Sensitivity tests with different source offsets within the waveguide are shown for event A. The observed and synthetic waveforms (top), spectrogram (lower left), and velocity spectra (right) of synthetic arrivals from events of different offset within the slab are shown. The observed waveform is shown in black and white in all figures while the synthetic waveforms are shown in blue to red colours. Synthetic models with the source at 6.0 km, 4.0 km, 2.4 km and 0.0 km from the top of the slab are shown in light blue, dark blue, pink and red respectively. Exciting the source too close to the top or bottom or centre the LVL does not produce a clear dispersion curve. Waveguide energy is excited most effectively at one third of the LVL width below the surface of the waveguide.

The position of the source within the waveguide affects the amount of energy that is excited within the waveguide (e.g. Martin & Rietbrock, 2006), and therefore affects the clarity of the dispersion curve that is seen, as well as the relative amplitude of peaks in the frequency domain. We find that the guided wave dispersion is seen most clearly when the source is close to the top of the LVL as demonstrated in figure 6.5. Therefore, the source is positioned one third of the width of the LVL below the top of the slab in the resolution tests shown in figure 6.4 and described below.

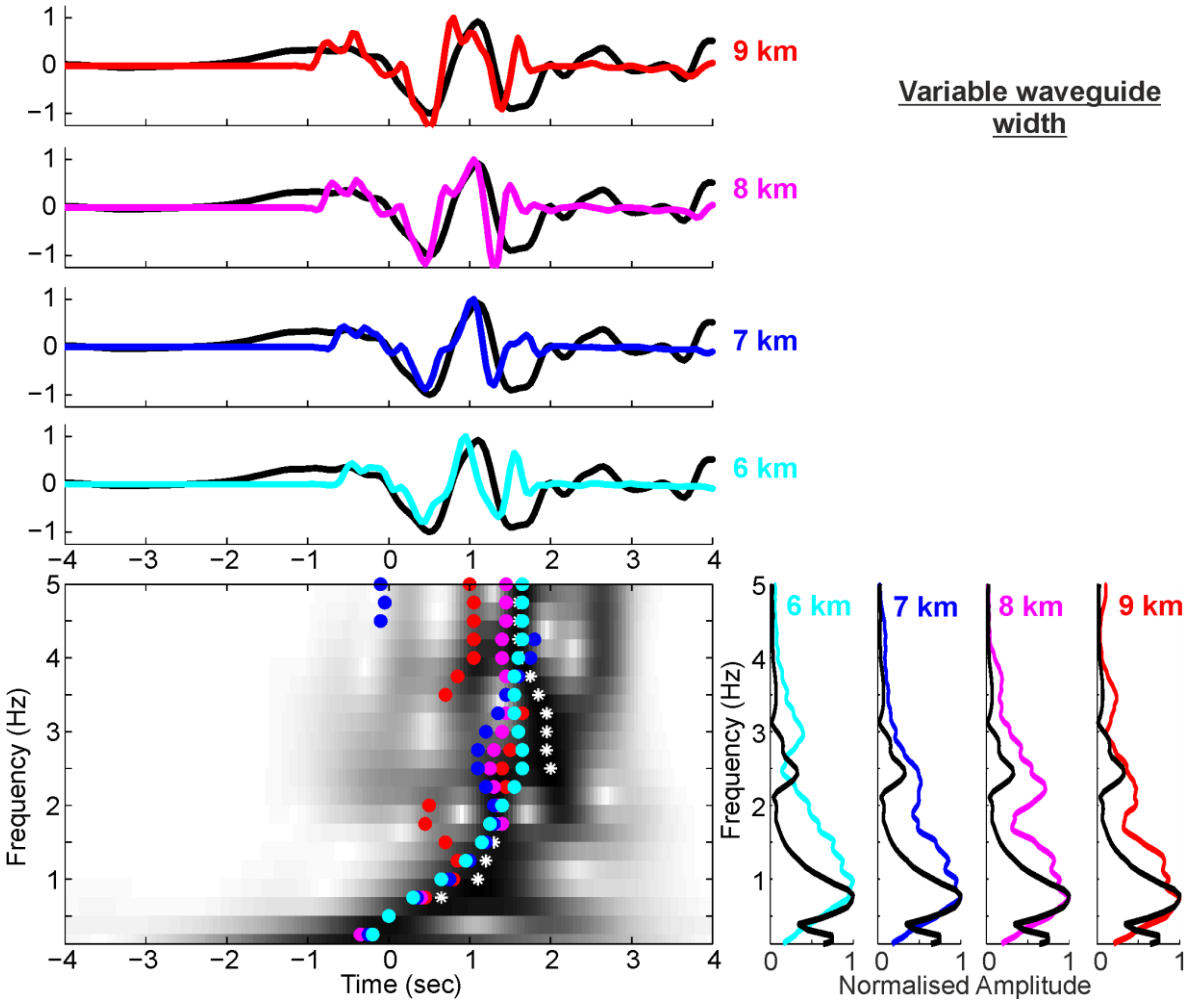

Figure 6.6 – Sensitivity tests with a variable waveguide width are shown for event A. The observed dispersive signal is shown in black and white while the synthetic signals are shown in colour. The spectrogram comparison is shown in the lower left panel, the velocity spectra comparison is shown to the right, and the waveforms comparison is seen at the top of the figure. Synthetic waveforms from simulations with a waveguide width of 6 km, 7 km, 8 km and 9 km shown in red, pink dark blue and light blue respectively. The simulations shown have a constant waveguide velocity of 7.7 km/s, and the source is placed one third of the waveguide width below the top of the LVL. All but the thinnest waveguide width give a reasonable dispersion. Clear differences are seen though in the velocity spectra of the signal, and so are also seen in the waveform.

6.4.1 Waveguide thickness

A range of waveguide thicknesses between 4 – 10 km have been tested. A subset of these results for waveguide thicknesses of 6 – 9 km are shown in figure 6.6 for a fixed waveguide velocity of 7.6 km/s. While the dispersion curve is not overly sensitive to small variations in the waveguide width the dispersion curve does break down for wider LVL widths. The velocity spectra of the signal however show much more variation with waveguide width.

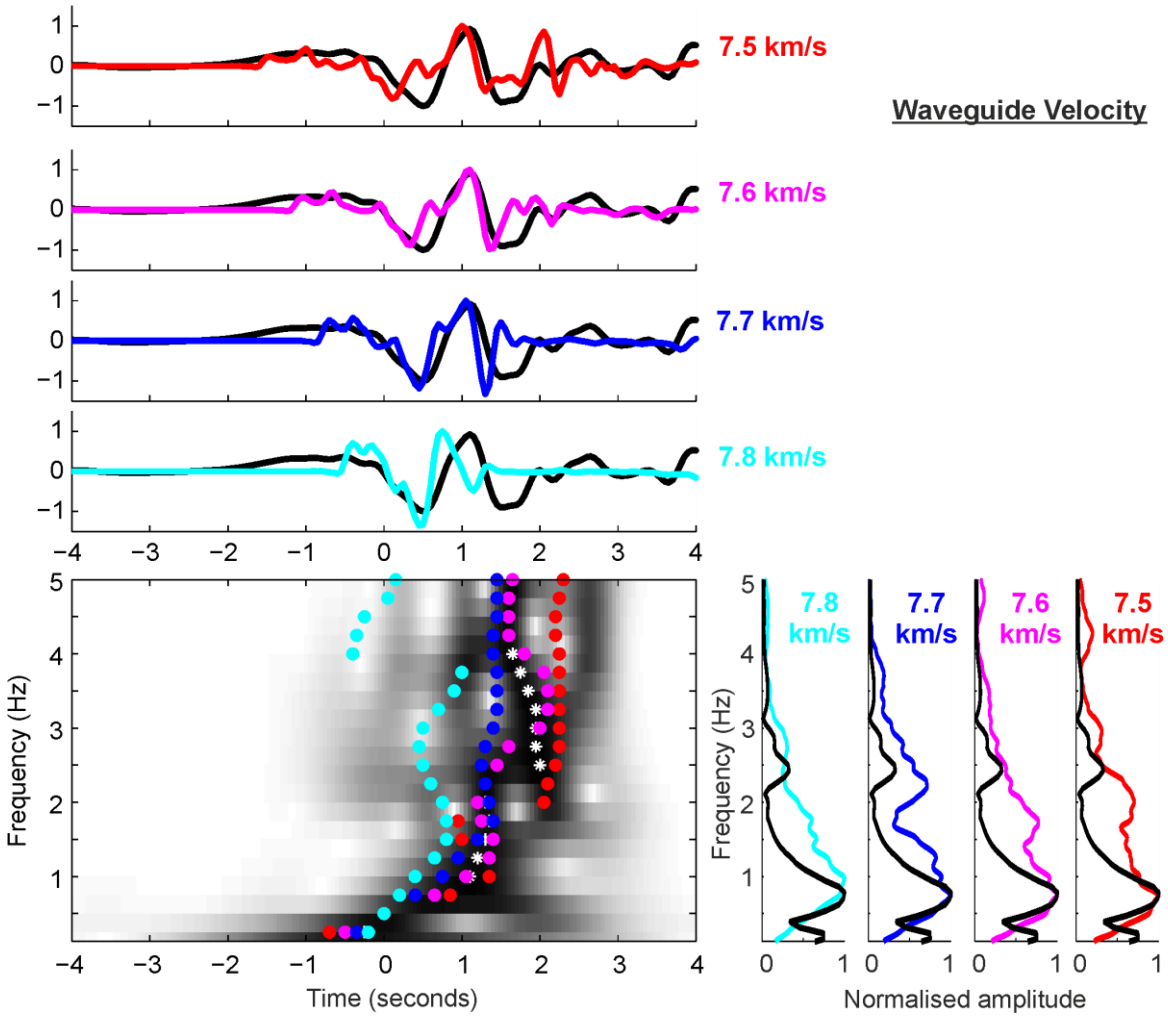

Figure 6.7 – Sensitivity tests with a variable waveguide velocity are shown for event A. The observed and synthetic waveform are shown in black and white and synthetic waveform are shown in colour for the spectrogram, velocity spectra and waveforms as described in figure 6.5 and 6,6. Synthetic waveforms from simulations with a waveguide velocity of 7.5, 7.6, 7.7 and 7.8 km/s are shown in red, pink, dark blue and light blue respectively. The waveguide width is 8 km in the results shown, and the source is one third of the waveguide width below the top of the LVL. A clear difference in the magnitude of dispersion seen in the spectrogram allows the average waveguide velocity to be interpreted.

If the waveguide is to narrow then the high frequency peak that is seen at 2 Hz in the observed signal is seen at higher frequencies in the synthetic waveform. This therefore provides a lower limit on the waveguide width. If the waveguide velocity is too wide, the secondary peak in the frequency domain is seen at frequencies that are too low, and therefore is not seen as a clear secondary peak. Taken with the breakdown of the of the dispersion curve at this waveguide width our approach provides an upper limit on the width of the LVL. Resolution tests for event A shown in figure 6.6 suggest that a waveguide of 6 - 8 km width explains the observed dispersion well. In further waveform fitting examples the waveguide width is assumed to be 8 km.

6.4.2 Waveguide velocity

A range of waveguide velocities have been tested and compared to the observed waveform. Varying the waveguide velocity affects both the spectrogram and the velocity spectrum of the waveform. The spectrogram however shows the clearest change, with the high frequency component of the arrival being most delayed in models with a higher velocity contrasts. If the modelled velocity contrast is too large then the dispersion in the synthetic waveform is too great. If the velocity contrast is too small the dispersion seen in the synthetic waveform is less than in the observed waveform. Figure 6.7 shows a range of velocity contrasts compared to the dispersive arrival at the station ERM from event A at 220 km depth.

An average velocity of 7.6 - 7.7 km/s explains the dispersion observed from event A well. This represents a velocity contrast of approximately 6.1 - 7.3% with the underlying cool mantle material, or a velocity contrast of 4.75 - 5.0% with the mantle material above the slab. These velocities also provide a good fit in the velocity spectra and for the waveform, and therefore have a low combined misfit.

6.4.3 Full waveform modelling

If both the relative arrival times of different frequencies and the relative amplitude of the different frequencies are constrained by the spectrogram and the velocity spectra respectively, the low pass filtered synthetic and recorded P-wave arrivals can be directly compared. Comparison of the observed and synthetic waveforms is shown in the top of figures 6.5 – 6.6. The waveform fits are clearly better for synthetic waveforms that are fitted well in the spectrogram and velocity spectra, with good fits showing several peaks and troughs that correspond well, while poor fits only match one maximum or minimum.

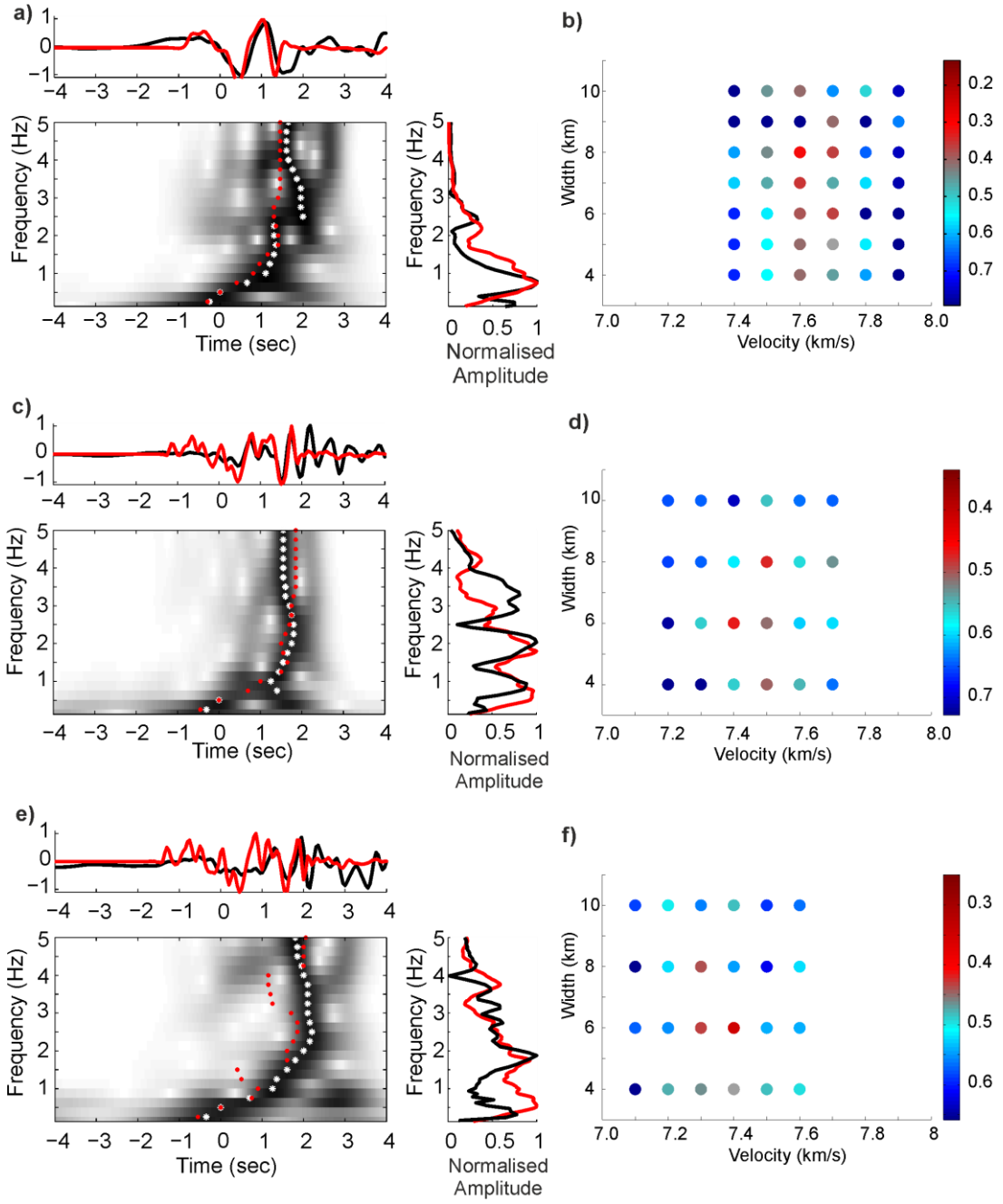

Figure 6.8 – Waveform fits for events at different depths. The optimum waveform fits are shown for a) event A at 220 km depth, c) event B at 186 km, and e) event C at 150 km depth (see figure 6.1). The waveform recorded at the station ERM is shown in black and white, and the synthetic waveform is shown in red. The recorded and synthetic spectrogram (lower left), velocity spectrum (right) and waveform (top) of each of these events is compared. The best fitting waveguide velocity for these events reduces with depth. The waveforms shown here are from simulations with a wave guide velocity of 7.7, 7.5, and 7.4 km/s for event A, B and C respectively. The combined misfit for the models tested for a given event are shown for b) event A at 220 km depth, d) event B at 186 km, and f) event C at 150 km depth.

This method of constraining waveguide structure has been applied to dispersive arrivals observed from other events seen at 150 - 220 km depth. The resulting waveform fits for these events are shown in figure 6.7 (including event A) along with the combined misfit for each of the LVL velocity models that were tested for each event.

While the observations can be explained by a constant waveguide width of 8 km, the events occurring at more shallow depths than event A are not modelled well by a waveguide with the same average velocity contrast. The dispersive arrival from event B (which occurs at 186 km depth) is explained well by a LVL with a velocity of 7.4 - 7.6 km/s, representing an average velocity contrast of 7.3 – 9.8 % with the slab below. Event C occurs at 150 km depth and the dispersion observed at ERM suggests a waveguide velocity of 7.2 – 7.4 km/s, which is 9.8 - 12.2 % slower than the fast slab below.

The best fitting synthetic waveform, and the parameter study for each event is shown in figure 6.8. These waveform fits suggest that an ~8 km thick LVL may persist to a depth of 220 km. These observations also suggest that the velocity contrast of the waveguide reduces with depth and that the average velocity contrast of the waveguide is less for deeper events as summarised in figure 6.9. These results are discussed in further detail in section 6.7 and 6.9.

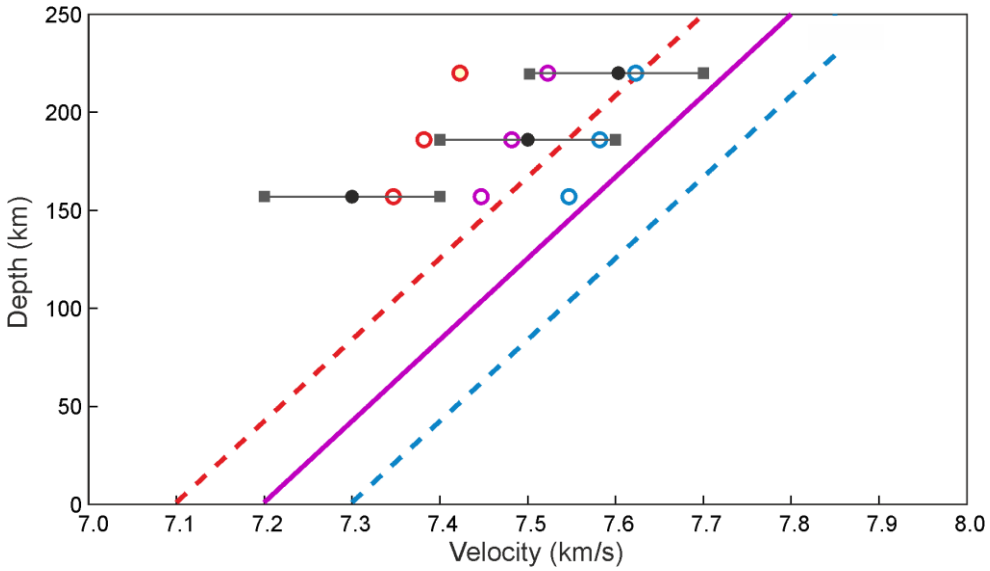

Figure 6.9 – Average waveguide velocities for events of different depths are shown in black. The grey bar shows the range of acceptable average waveguide velocities for each event, with the black circles showing the optimum average waveguide velocity for that event, the waveform fit for which is shown in figure 6.7. Variable waveguide velocity models are shown in red, purple and blue. The open circles show the average velocity of these variable velocity models, assuming the guided wave decouples at 50 km depth, in order to compare with the average velocities produced by guided waveform fitting. The solid purple line shows the optimum variable velocity waveguide model shown in figures 6.12 and 6.13. The dashed red and blue lines show the upper and lower velocity limits of the variable velocity models.

6.5 Attenuation Structure

Significant variations in attenuation and therefore Q are seen in subduction zones, most notably in the highly attenuating mantle wedge (e.g. Tsumura *et al.,* 2000; Haberland & Rietbrock, 2001; Schurr *et al.,* 2003; Rychert *et al.,* 2008). While attenuation tomography is able to resolve the broad scale features of the subduction zone such as the low Q mantle wedge and the cool high Q subducting oceanic lithosphere, these tomographic studies do not have the resolution to resolve the Q of low velocity structures at the top of the subducting slab. In other examples of seismic waveguides such as fault zones it has been shown that low values of Q within the waveguide significantly affect the guided wave arrivals (e.g. Ben-Zion *et al.,* 1999). We therefore consider the effect of a reduced Q in the low velocity waveguide, as well as a reduced Q in the mantle wedge.

6.5.1 Mantle wedge Q

The range of quality factors considered is based on the Q values seen in the tomographic studies of the Northern Japan subduction zone (e.g. Tsumura *et al.,* 2000). Testing a range of values of Q from 160 – 1000 showed that attenuation in the mantle wedge does not change the magnitude of the dispersion that is seen in a spectrogram (figure 6.10). It does however have a significant effect on the signal in the frequency domain.

The example shown in figure 6.10 for event A indicates that a lower Q in the mantle wedge reduces the relative amplitude of the high frequency peak at ~2 Hz. A Q of less than 500 gives a good fit without the need to apply a source corner frequency to the synthetic waveforms as is done for the synthetic waveforms from elastic waveform simulations. The comparison of the observed and synthetic waveforms also shows that introducing an attenuating mantle wedge can improve the waveform fit.

6.5.2 Reduced Q in the LVL

Introducing a low Q in the LVL reduces the amplitude of the higher frequency arrivals significantly as shown in figure 6.11. A Q of 500 produces a good fit in the frequency domain, but does not affect the spectrogram at the frequencies that are resolved. Lower values of Q significantly reduce the amplitude of the high frequency arrivals (> 2 Hz). The waveform fit is not greatly affected as the signal is dominated by low frequency waves. The spectrogram is however affected significantly. Clear dispersion is not seen for values of Q that are 250 or lower as the amplitude of the high frequency guided wave arrivals cannot be detected anymore.

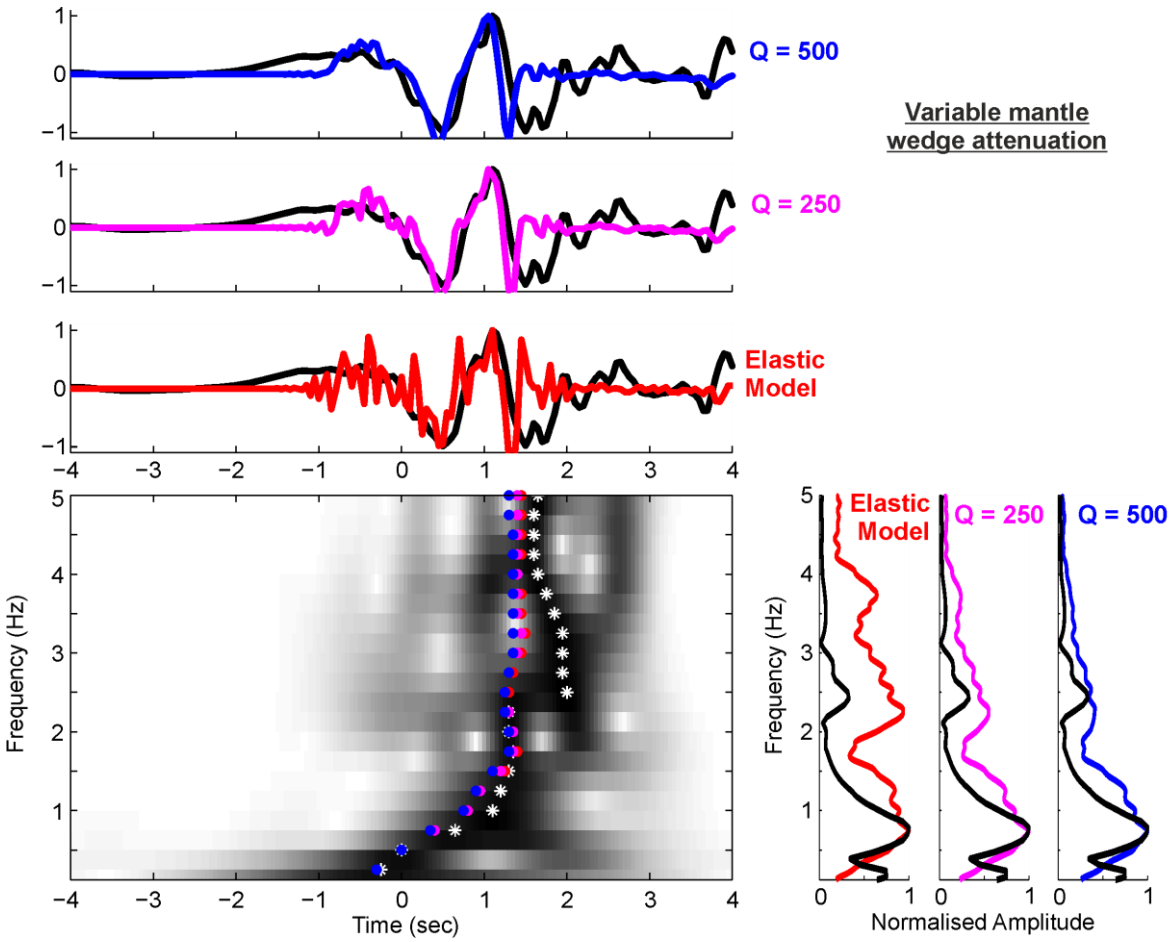

Figure 6.10 – Variable mantle wedge attenuation. Waveforms, spectrograms and velocity spectra are shown as in figures 6.4. The waveform produced by an elastic FD model, low pass filtered at 5 Hz, is shown in red. Waveforms produced by a visco-elastic FD modelling with a mantle wedge Q of 250 and 500 are shown in pink and blue respectively.

Visco-elastic waveform simulations therefore show that observed guided wave dispersion cannot be explained by low values of Q in the subduction zone system. Values of Q in the LVL must be greater than 250 and are likely to be at least 500 in order for the LVL to act as an effective waveguide.

Using Azimi's attenuation law (Aki & Richards, 1980) we estimate that in the 0.5 – 5.0 Hz frequency range considered, a Q of 250 could cause dispersion equivelant to an appartent velocity contrast of ± 0.2 %. The more realistic case of a LVL Q of 500 would produce a maximum velocity contrast of ± 0.1 %. We can therefore conclude that elevated attenuation does not contiribute significantly to the dispersion observed in this frequency range.

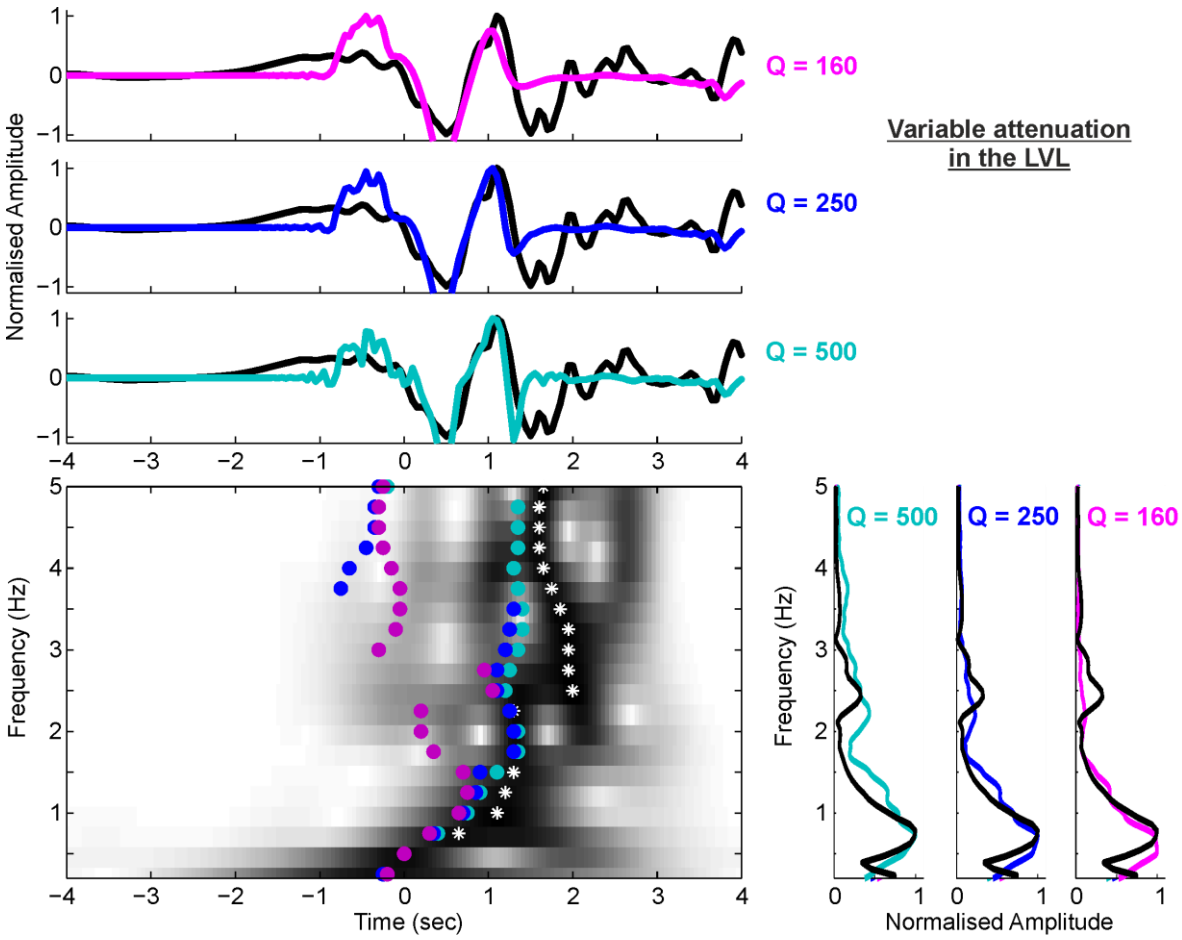

Figure 6.11 – Attenuation within the waveguide. Waveforms, spectrograms and velocity spectra are shown as in figures 6.4. The waveforms from visco-elastic FD models with a Q factor of 500, 250, 160 are shown in light blue, dark blue and purple respectively and are directly compared to the arrival of event A at the station ERM. A Q of 250 or lower reduces the amplitude of high frequencies within the waveguide, and so clear dispersion is not seen.

Using the lower limit on the Q of the LVL we are also able to estimate the maximum degree of melting that can have occurred within the LVL, i.e. on the ray path of the guided wave. We assume that the Q of melted oceanic crust corresponds to the lowest value of Qp that has been inferred in the mantle wedge, where pervasive melting is thought to occur. We therefore assume that the melted LVL material would have a Q of 30, based on the attenuation tomography of the Nicaraguan mantle wedge (Rychert et al., 2008). Assuming the Q of the solid LVL is 1000, the Q of melted LVL is 30, and the average Q of the LVL is 500 (constrained above), we can calculate the maximum degree of melting over the ray path by calculating t* along the LVL. We calculate that a maximum of 2.6 % of the LVL may be molten, suggesting that while melting within the LVL is far from pervasive, small localised pockets of melting cannot be ruled out.

6.6 3D Modelling

The modelling presented in this paper so far has all been performed in 2D. These models are relatively computationally "cheap" to run and therefore have allowed the extensive resolution tests described above to be performed. Waveguides are however 3D features, and 3D waveform propagation may affect the relative amplitude of dispersive arrivals and therefore the interpreted structure. The 3D FD model setup used in this study, which is accurate to 2 Hz takes approximately 8.5 hours to run on 1440 processors (90 KAu) on the UK national super computer Hector (phase 3). The cost of running a 2D simulation accurate to 5 Hz on the same machine is approximately 0.15 % of this (0.138 KAus).

This means that the computational cost of modelling in 3D is still too high to perform systematic parameter studies with 3D models. Instead we benchmark the 2D models with 3D simulations, to test if the structures inferred by resolution tests using 2D simulations produce similar dispersion in 3D.

6.6.1 3D Model Setup

To keep computational costs to a minimum 3D modelling is performed using a corridor model that is just over the length of the ray path, and just over the depth of the source in the x- and z-direction, respectively. The model width (the y-direction) is as small as possible. The width must however be greater than the Fresnel zone of the lowest frequency wave considered and large enough to ensure that reflections form the model sides do not alter the synthetic dispersed wave.

To ensure that all frequencies considered are not affected by the absorbing boundary conditions, the width of the model must be at least 1.5 times the maximum wavelength at 0.5 Hz. In practice however, the model corridor width is defined by the need to ensure that the side reflections arrive later than the time window analysed. In this case the modelled corridor has a width of 129.6 km, which is wide enough to remove side reflections from the dispersive wave train (i.e. the first 5 seconds). The amplitude of the side reflections is also reduced by > 90 % as the result of the absorbing boundary conditions. As the side reflections in a corridor model are likely to be grazing waves we use exponential dampeners.

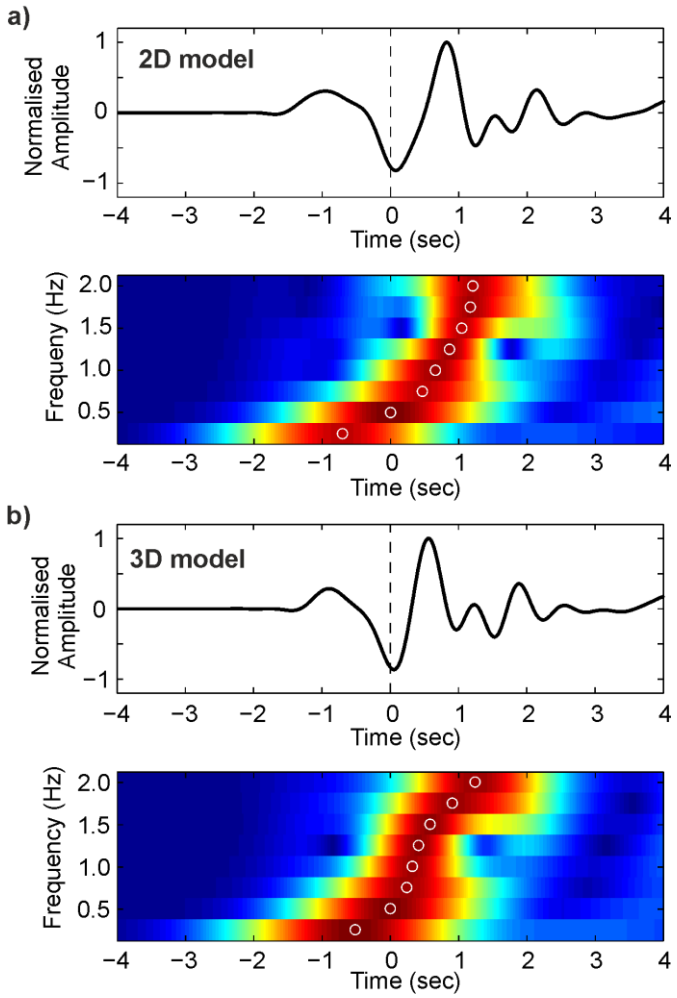

Figure 6.12 – Waveform and spectrogram of 2D and 3D models. **a)** Synthetic waveform and spectrogram from 2D FD simulation of event A accurate to 2Hz. **b)** Synthetic waveform and spectrogram from a 3D simulation of event A accurate to 2Hz. Both models have an 8 km wide LVL with a velocity of 7.7 km/s.

6.6.2 Benchmarking 2D and 3D models

2D and 3D simulations are run with the same nodal spacing and temporal resolution. The simulations are accurate up to 2 Hz. The best fitting 2D velocity model for event A is used in both the 2D and 3D simulations. The resulting waveforms, and spectrograms are shown in figure 6.12. Figure 6.13 shows a comparison of 3D simulations with different velocities of LVL with arrivals from event A.

The 1 - 1.75 Hz frequency bands are more delayed in the 2D model than the 3D model, but the difference is only ~0.2 seconds. Varying the position of the source in the LVL changes the fit only slightly. The best fitting velocities from the 3D simulations for this event are

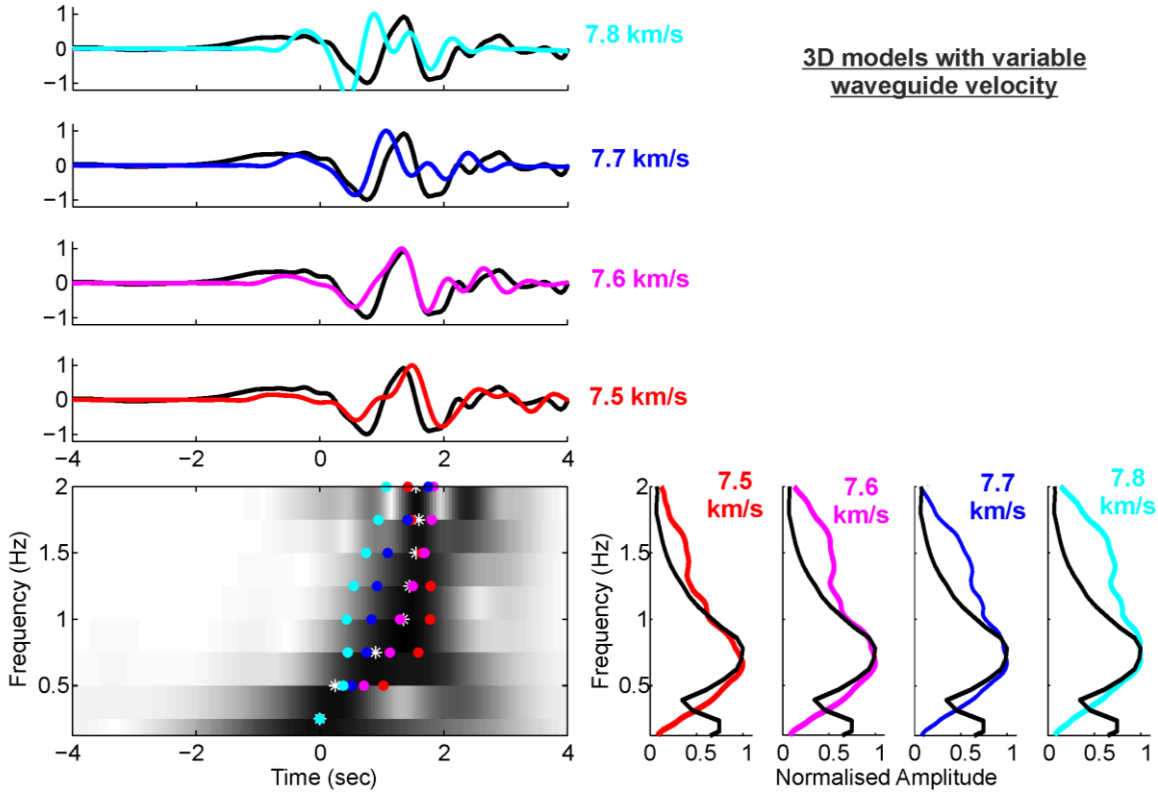

Figure 6.13 – Comparison of 3D models with different average LVL velocities. The top four panels show the low pass filtered waveforms. The bottom left panel shows the spectrogram comparison, and the right four panels show the velocity spectra comparison. The synthetic waveforms from the 3D corridor model with a LVL velocity of 7.5, 7.6, 7.7 and 7.8 km/s are shown in red, pink, blue and light blue respectively.

between 7.5 and 7.7 km/s, with an optimum average LVL velocity of 7.6 km/s. This is the same range of velocities that is inferred from the 2D simulation.

This benchmark shows that the waveguide structure inferred from the 2D parameter study leads to a reasonable dispersion in the 3D model, and therefore the 2D model provides a reasonable approximation of the 3D waveguide structure. We therefore conclude that a 2D waveform model provides a reasonable approximation of the waveguide structure.

6.7 Variable Down Dip Velocity Contrast

Modelling dispersive arrivals from individual events at depth of > 150 km has shown that the average velocity of the waveguide increases with depth. This may well be due to the progressive dehydration of subducted oceanic crust as proposed by various thermo-petrological studies (e.g. Hacker *et al.,* 2003a).

If phase transformations are occurring, the average velocity inferred for these events will be a composite of the mineralogies seen along the waveguide. In order to interpret these

low velocity features further we need an indication of the actual velocities occurring at these depths. We therefore test several models where the velocity contrast of the LVL reduces with depth, in order to produce a single velocity model that accounts for the dispersion seen from events at different depth. This velocity model can then be used to interpret the mineralogies at these depths.

A range of velocity models are considered for the upper crust. For simplicity the waveguide width is kept at 8 km, as constrained by the sensitivity tests described in section 6.4. Introducing a variable velocity LVL increases the amplitude of the refracted P-wave arrival 'Pn', relative to the guided wave. The Pn arrival travels in the faster mantle material below the LVL and is artificially strong in the synthetic waveforms due to the sharp velocity contrast of the velocity model. In these variable velocity LVL models, the velocity at the point at which the waveguide decouples may also affect the relative amplitude of the decoupled guided wave.

In order to reduce the amplitude of Pn in the dispersive arrivals the waveforms shown are recorded closer to the trench than the offset of the station ERM, as depicted in figure 6.14. This does not have a significant effect on the observed dispersion of the guided wave at this offset, as it will be the same as a wave which has decoupled as the guided wave 10 km further from the trench. A difference of 10 km can however easily be accommodated in the error in the slab geometry.

6.7.1 Variable velocity LVL

The velocity of this variable velocity waveguide is derived from the average waveguide velocities estimated in section 6.4. The average velocity at the depth of each event is calculated assuming that the waveguide decouples at 50 km depth, and is compared to the average waveguide velocity estimates. This is shown for three velocity models in figure 6.9. The resulting velocity model can then be tested against the observed dispersive waves using a full waveform simulation. The best fitting variable low velocity waveguide model is shown in figure 6.14. The resulting dispersion for events at depths of 150 - 220 km is shown in figure 6.15.

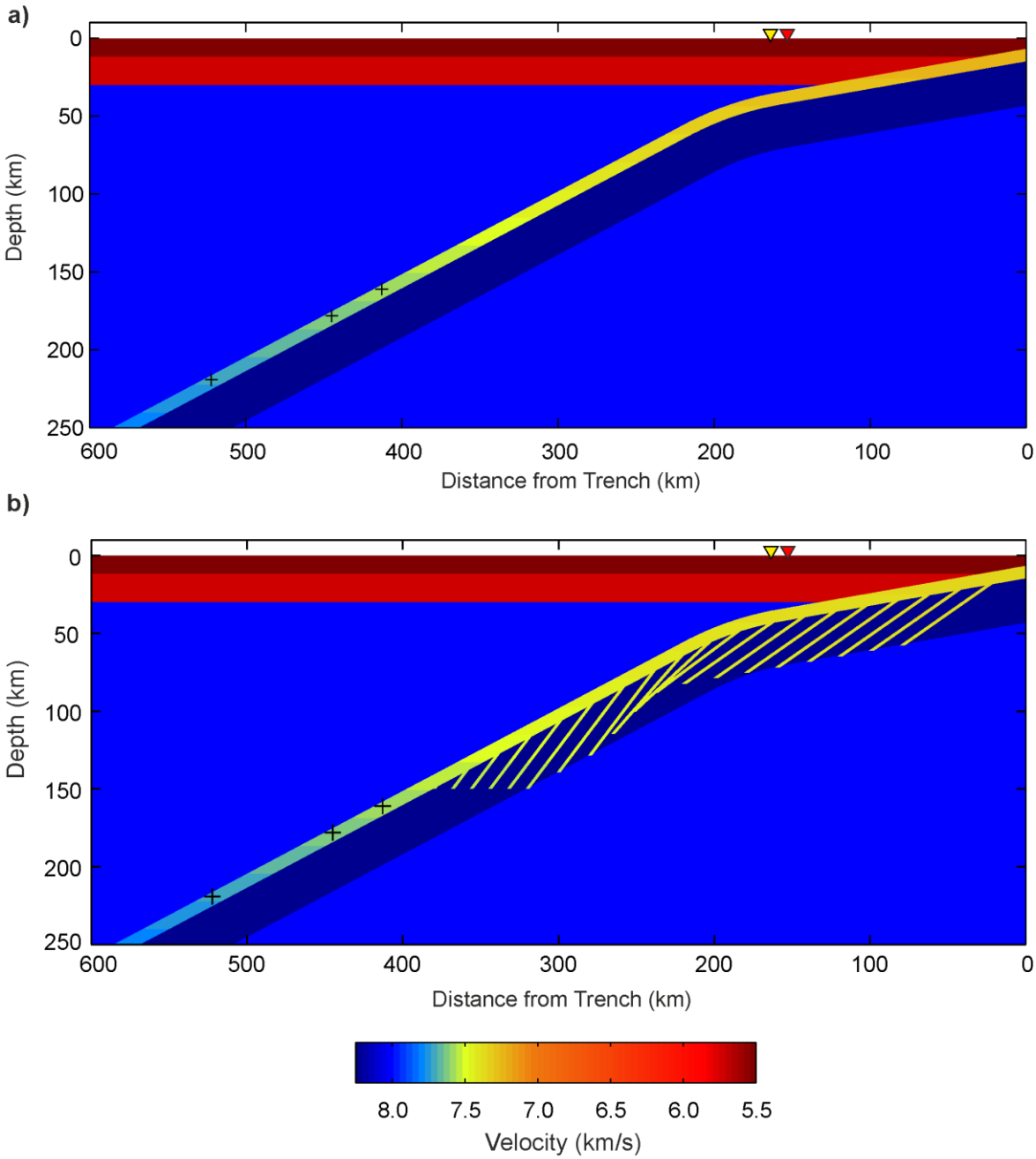

Figure 6.14 – Variable velocity waveguide velocity model. **a)** The single LVL. **b)** LVL and low velocity dipping fault zones inferred by Garth & Rietbrock (2014).The velocity (and velocity contrast) of the waveguide reduces with depth as inferred from the average waveguide velocity fits. The velocity of the waveguide with depth is shown by the purple line in figure 6.8, or the solid grey line in figure 6.15. The position of the station ERM used in figures 6.4 – 6.7 and 6.9 – 6.12 is shown by the yellow triangle, and the revised receiver position is shown by the red triangle. The source positions in the model are shown with black crosses.

Figure 6.9 shows the down dip variation in velocity along the LVL for the optimum model shown in figure 6.14a. The upper and lower velocity models with the same velocity gradient are also shown to give an indication of the uncertainty in fitting the dispersive waveforms. Other velocity gradients have been tested and can account for the dispersion seen from

events at different depths. Steeper velocity gradients however cause an even stronger Pn arrival, as the velocity contrast of the LVL is less at greater depth, so the waveguide is less efficient at depth. Less steep velocity gradients mean that either the deepest or shallowest event is poorly fitted. Velocity models with different gradients still fall within the upper and lower velocity shown by the dashed line.

6.7.2 Variable velocity model with fault zones

Introducing dipping normal fault structures in the subducting mantle as inferred by Garth & Rietbrock (2014) may affect the dispersed arrivals seen from deeper events. We test the effect of introducing low velocity fault zones on the dispersion seen from the best fitting variable velocity model. The velocity model is shown in figure 6.13b, along with the source positions tested in this model.

The resulting waveforms are presented in figure 6.16. The addition of the low velocity fault zones to the velocity model does not stop the LVL from acting as an effective waveguide and the synthetic dispersions are still reasonably similar to the recorded dispersive waveforms. The overall quality of the fit is however generally reduced, suggesting that details such as source offset may need to be revised to optimise this model. The variation in the fits of the spectrogram however suggest that including fault zone structures in the guided wave parameter study would not greatly affect the waveguide velocities inferred.

6.7.3 Relative timing of synthetic and recorded arrivals

As an independent test for the variable LVL velocity model we compare the absolute delay time of the P-wave onset to the arrival time from the synthetic full waveform model. The time residual between the recorded and synthetic times is less than 1.5 seconds for all stations except station HID, which has a logged timing error. The discrepancy seen at the stations is largest at the station ERM, but does not vary systematically with source depth. The discrepancy in the delay time is therefore unlikely to be caused by a systematic error in the velocity model and is most likely to be explained by local variations topography and geology, as well as errors in the picked arrival time.

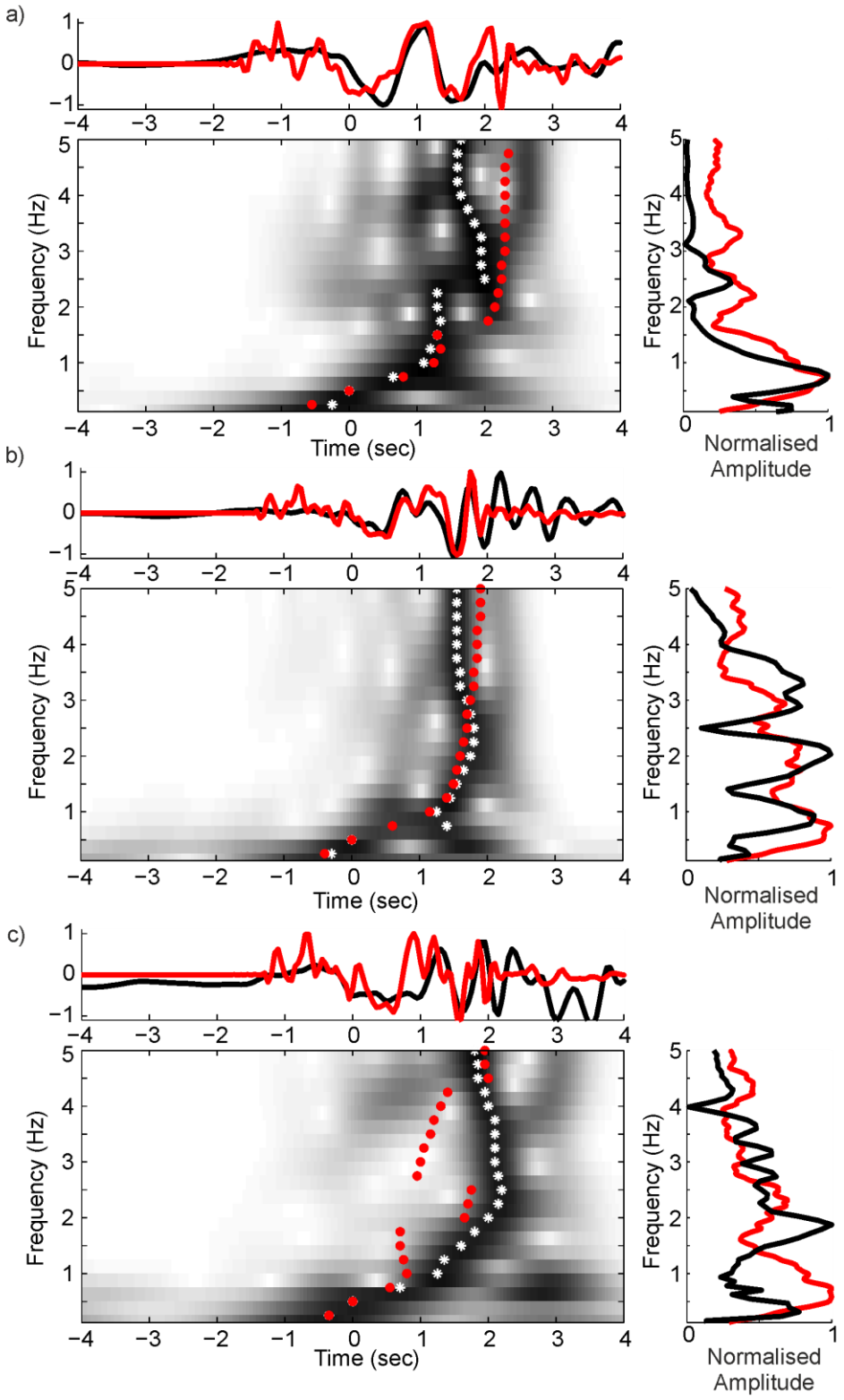

Figure 6.15 – Waveform fits from the single LVL variable velocity waveguide model shown in figure 6.13 a. Figure panels are as in figure 6.7 with arrivals from event A, B and C shown in part **a)**, **b)** and **c)**.

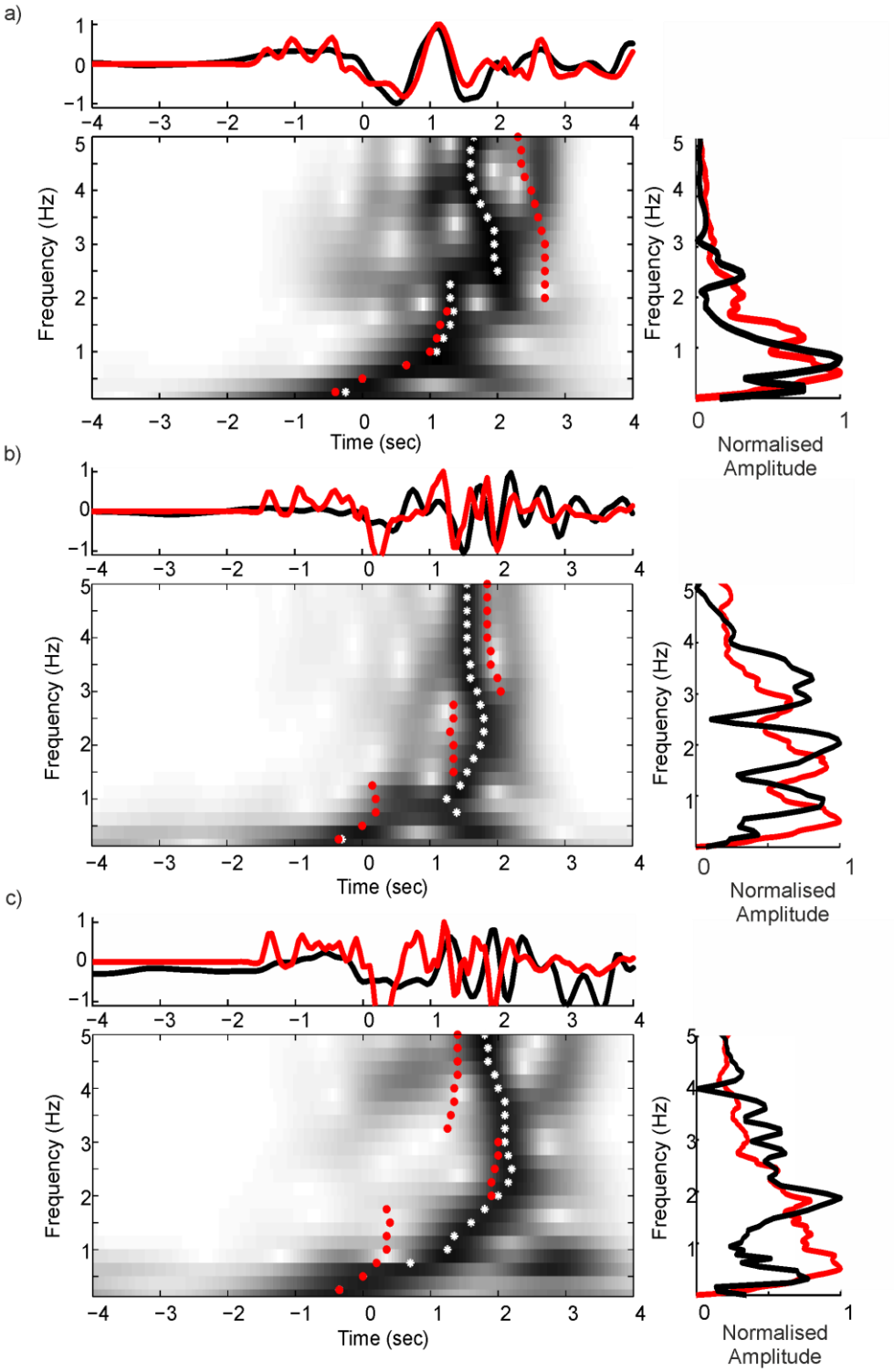

Figure 6.16 – Waveform fits from the variable velocity model including dipping low velocity fault zones. Fits are shown for events A, B and C in **a)**, **b)** and **c)** respectively.

6.8 Calculating MORB Phase Velocities

The velocities calculated above can be directly compared to the velocity of mineralogies that are predicted to occur at the temperature and pressure conditions found at intermediate depths (e.g. Hacker *et al.,* 2003a; 2003b). A suite of mineralogies predicted to occur at intermediate depth in the Northern Japan subduction zone by Hacker *et al.,* (2003a; 2003b) are considered. The velocity of these phases at depth is calculated using mineral abundances of Hacker *et al.,* (2003b) and the excel macro of Hacker & Abers (2004). The pressure and temperature (P-T) conditions of the Hokkaido subduction zone are taken from the global compilation of subduction zone thermal models of Syracuse *et al.* (2010), used by van Keken *et al.* (2011).

The velocities of seven mid-ocean ridge basalt (MORB) mineral phases are plotted in figure 6.16 along with the velocity model determined through guided wave analysis. A sharp decrease in the velocity with depth is seen for each of these phases at approximately 70 km. This relates to the fast increase in temperature seen at the top of the slab in the thermal models of Syracuse *et al.* (2010), as the slab is warmed by the mantle wedge. This reduction in velocity may therefore be overestimated as at greater depth within the subducting slab the increase in temperature may not outstrip the increase in pressure.

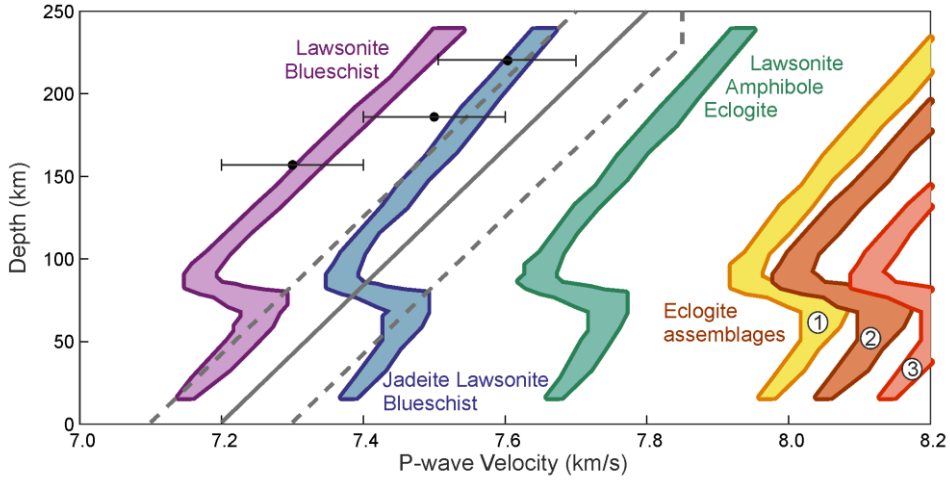

Figure 6.17 – Comparison of LVL velocities and MORB phases. MORB phases predicted to occur in the cool subduction zone conditions of Northern Japan are shown, and the velocities of each phase is calculated using the excel macro of Hacker & Abers (2004), for the P-T conditions of the Hokkaido subduction zone taken from the global thermal model compilation of Syracuse et al. (2010). Average velocities inferred in section 6.4 are shown in black. The variable down dip velocity determined in section 6.7 are shown by the solid and dashed grey lines. The model corresponding to the best fitting solid grey line is shown in figure 6.13. Eclogite assemblages 1, 2 and 3 correspond to amphibole eclogite, zoesite eclogite and eclogite respectively.

6.9 Discussion

6.9.1 Velocity Structure

Thermo-petrological modelling has shown that the low velocity structure detected at depth by various seismic studies can be explained by the persistence of low velocity hydrous mineral assemblages in the subducted basaltic oceanic crust (e.g. Helffrich, 1996). It is proposed that the low velocity mineralogies are seen where lawsonite is stable (Connolly & Kerrick, 2002), and that the low velocity contrast reduces as the oceanic curst dehydrates to seismically indistinguishable eclogite (e.g. Hacker *et al.,* 2003b). Dispersion seen in Northern Japan is explained well by a LVL of 6 - 8 km thickness, and the average velocity of the waveguide is similar to MORB phases that are expected to occur at this depth (figure 6.16). These observations therefore support the hypothesis that low velocity structure seen at these depths is explained by hydrated oceanic crust.

The average velocity contrast of the waveguide inferred from deeper events is less than the average waveguide velocity contrast from shallow events. This variation in average velocity contrast inferred from events of different depth can be explained by a variable velocity LVL as shown in part 6.7 of this chapter. This velocity model allows us to directly compare the velocity contrast of the waveguide with the velocity of mineral assemblages predicted to occur at these depths. Figure 6.16 shows the average velocities inferred from events of different depths as well as the variable velocity model. The velocities of mineral phases predicted to occur in the relatively cool subduction conditions of Northern Japan (Hacker *et al.,* 2003b) are also shown.

The inferred velocities are significantly lower than eclogite assemblages that are predicted to occur at these at high P-T conditions, suggesting that the lawsonite-eclogite transformation has not occurred even at depths of 220 km. The velocities inferred from the guided wave analysis are however similar to the lawsonite bearing minerals that are thought to occur at up to 150 km depth (Hacker *et al.,* 2003b).

At less than 50 km depth the velocity model is not constrained by the guided wave observations, as the guided wave has decoupled from the slab at this point. The high resolution tomography of Nakajima *et al.* (2009) however shows P-wave velocities of ~7 km/s at these depths, which are interpreted as lawsonite blueschist (LB) phase basaltic crust.

At depths of 50 - 75 km the velocities inferred from the guided wave modelling are between the velocities predicted for a LB or jadeite lawsonite blueschist (JLB), suggesting a composite of these two mineralogies may be present. At 75 – 150 km depth the velocity contrast may explained by JLB. With increasing depth however, the estimated waveguide velocity contrast becomes lower than the predicted velocity of JLB. This may represent the progressive transformation to a higher velocity phase such as a lawsonite amphibole eclogite (LAE). The guided wave velocity model suggests that full transformation to a LAE does not occur above 220 km depth. The velocities present at these depths are however consistent with approximately 50 % of the JLB having transformed to LAE. The composite velocities seen may be due to the phase transformations occurring gradually over a range of depths due to kinetic hindering of the metamorphic reactions. This slow onset of the transformations may also explain why full eclogitization is not seen at ~ 150 km depth as predicted by thermo-petrological modelling.

Receiver function studies both in Northern Japan (e.g. Kawakatsu &Watada, 2007) and other subduction zones have however suggested that the eclogite transformation occurs at shallower depths, in good agreement with the depths predicted by thermo-petrological models (e.g. Rondenay *et al.,* 2008). As guided waves spend the majority of their ray path interacting with the low velocity oceanic crust they are likely to be more sensitive to the velocity contrast. Receiver function studies may not be as sensitive to the low velocity structure at this depth because the velocity contrast with the cool slab below is less these depths. P-S conversions from low velocity structure at this depth would be observed most clearly at stations that are far from the trench. Many temporary arrays do not have this extent of coverage, and in Northern Japan the appropriate receiver offsets would be in the Sea of Japan. This may explain why this and other guided wave studies (e.g. Abers 2000; Martin *et al.,* 2003) infer the persistence of low velocity mineralogies to greater depth than they are resolved by receiver function studies. High resolution tomography studies have also resolved low velocity oceanic crust at ~ 100 km depth, but do not have the resolution to image low velocity structures below 150 km depth (e.g. Nakajima *et al.,* 2009).

The persistence of lawsonite bearing mineralogies to depths of at least 220 km suggests that mineral bound H_2O in the subducted oceanic crust may transport water to greater depths than has previously been suggested (e.g. van Keken *et al.,* 2011). The profile of seismicity shown in figure 6.1b shows that a cluster of seismicity is seen at 200 - 250 km depth. The presence of hydrous mineral assemblages may offer an explanation of how this seismicity occurs through dehydration-embrittlement due to the gradual transformation of

lawsonite to eclogite. The delay in the onset of full eclogitization of the oceanic crust inferred by this study may also affect the buoyancy of the slab and therefore the stress state of the subducting lithosphere.

6.9.2 Modelling in 3D

Benchmarking the 2D models with 3D corridor models has shown that the velocity structures that are inferred from 2D modelling produce a similar dispersion in 3D. We therefore show that 2D models are adequate to estimate the waveguide velocity structure through resolution tests.

It is noted that the spectrogram does not have exactly the same shape at 1 – 1.75 Hz. This is likely to be due to the difference in relative amplitude of the guided P-wave arrival and the refracted Pn arrival. In 2D simulations the amplitude of non-guided body waves reduces with distance from the source (r) due to geometrical spreading proportional to $1/\sqrt{r}$. The guided wave amplitude does not reduce due to geometrical spreading in the 2D case. In the 3D case however the guided wave amplitude reduction is proportional to $1/\sqrt{r}$ while the unguided body wave (e.g. Pn) reduces amplitude with $1/r$. Therefore in the 3D case at larger distances the relative amplitude of Pn is higher.

6.9.3 Attenuation structure

Introducing low Q in the mantle wedge reduces the amplitude of the higher frequency arrivals and can improve the overall fit of the synthetic waveform in the frequency domain. Even when very low values of Q are implemented, attenuation in the mantle wedge does not have a significant effect on the overall dispersion seen.

Visco elastic simulations with high attenuation in the LVL have shown that the Q of the LVL is not low enough to explain the observed dispersion and that ≤ 2.6 % of the LVL has undergone melting. The lack of melting is consistent with the predicted thermal models of Northern Japan (e.g. Syracuse et al., 2010). Any melting that does occur on the LVL is likely to be restricted to localised pockets of melt

The reasonable values of Q that are inferred would not give a significant variation in apparent velocity with frequency, therefore we conclude that the dispersive waveforms seen from the subduction zone waveguide occur due to velocity structures. Attenuation structure does not significantly affect the relative timing of different frequencies, and has only a secondary effect on the relative amplitude of a given frequency.

6.10 Conclusions

This study offers new constraint on the intermediate depth low velocity structures seen in the Japan subduction zone. These observations suggest that the metamorphic reactions predicted to occur during subduction occur at greater depths than predicted by current thermo-petrological models, and that low velocity mineral assemblages persist to depths that cannot be resolved by other established seismic imaging techniques. The deeper occurrence of hydrous mineral phases in the oceanic crust potentially explains the cluster of seismicity seen at 200 - 250 km depth, and suggests that water subducted by the oceanic crust may be transported to greater depths within the mantle than has previously been thought.

Part three

Summary and Context

Chapter 7

Discussion and Further Work

Analysis of guided wave arrivals from intermediate depth events occurring in the subducted lithosphere beneath Northern Japan has resolved new details of the Wadati-Benioff zone (WBZ) velocity structure. We study dispersed arrivals from events occurring on a single profile in Northern Japan. This allows the waveguide structure to be constrained more tightly than in a broader analysis of dispersive arrivals from a range of back-azimuths (e.g. Abers, 2000), where the decoupling of the waveguide and the precise part of the slab that is being sampled is less clear. This approach also allows the waveguide geometry to be approximated as a 2D profile allowing parameter studies to be performed with 2D waveform propagation models, which are benchmarked to 3D models.

These waveform simulations have shown that dispersive arrivals from events well below the upper plane of seismicity can be explained by the occurrence of low velocity fault structures which act as a waveguide, transferring high frequency energy to the low velocity crustal waveguide at the top of the slab. Detailed waveform analysis of dispersive upper plane events at 150 – 220 km depth have also given new constraint on the metamorphic reactions that occur at this depth in the hydrated oceanic crust.

In this chapter we discuss the implications of these observations to our understanding of the subduction zones system. These results have particular implications for our understanding of how lower plane WBZ seismicity occurs, and the amount of water that is delivered to the mantle by hydrated subducting lithosphere.

7.1 Hydrated fault zones in the slab mantle

Guided wave analysis presented in Chapter 5 has suggested that lower plane events in Northern Japan are associated with low velocity serpentinised fault zones that penetrate into the slab mantle. While such structures have been inferred at the outer rise they have not been inferred at intermediate depths by any other seismic imaging technique. Current seismic tomography techniques that are based on the P and S arrival times do not have the

resolution necessary to image these structures, as kilometre-scale features such as a serpentinised fault zone will be averaged out along the ray path.

Receiver function methods rely on wave conversions that only occur at relatively sharp velocity contrasts that are orientated approximately perpendicular to the ray path of the incoming wave. Therefore receiver function methods will not be sensitive to the fault zone structures as the velocity boundaries of the dipping faults are orientated at a steep angle compared to the ray path of incoming teleseismic P-wave, and therefore will not give a strong P-S conversion.

It has been proposed that in South and Central American subduction zones normal faults occurring at the outer rise are reactivated at depth accounting for some of the intermediate depth seismicity seen in these subduction zones (e.g. Ranero *et al.,* 2005; Warren *et al.,* 2008). This phenomenon may not occur in all subduction zones, as the fault planes inferred for intermediate depth earthquakes in other subduction do not support the hypothesis that outer rise normal faults are reactivated at intermediate depths (e.g. Warren *et al.,* 2007; Myhill & Warren, 2012). It is possible that these faults are only reactivated when the slab stresses are favourable.

In Chapter 5 we show that some intermediate depth events at least may occur on or near to low velocity fault zone structures in the mantle, explaining the P-wave dispersion that is seen in arrivals from some lower plane events. The strong P-wave coda that is seen from all events in the WBZ indicates that intermediate depth events are likely to occur close to the low velocity fault zone scattering structure allowing S-P conversions to contribute to the P-wave coda. It also has been suggested that S-P conversions from earthquakes that occur just below the LVL may 'couple in' to the LVL, causing delayed P-wave arrivals (Horleston & Helffrich, 2012). This does not however provide an adequate explanation of the dispersed events that occur tens of kilometres below the crustal LVL, and while this hypothesis explains late arriving phases it does not explain the dispersed P-wave arrival.

The evidence presented in Chapter 5 therefore suggests that WBZ seismicity below the upper plane of seismicity is closely related to low velocity hydrated fault zones in the subducted mantle. It is possible that some of these events may occur due to reactivation of these outer rise normal faults, though the observations presented do not directly test this hypothesis. The pervasive serpentinisation associated with these faults may weaken the upper plate allowing bending and unbending of the plate during subduction to occur more easily. Pervasive serpentinisation would also reduce the density of the upper slab,

suggesting that the slab pull due to the dense plate may be slightly less than previously thought.

7.2 Metamorphic reactions in the subducted oceanic crust

Guided waves excited from intermediate depth events occurring within the low velocity oceanic crust at different depths show that the average velocity of the waveguide varies with depth, suggesting that the velocity contrast of the waveguide reduces with depth (Chapter 6). Subduction zone thermo-petrological models have shown that the velocity contrast of the low velocity subducted oceanic crust may decrease with depth (e.g. Hacker *et al.,* 2003b). Observational constraints on this reduction in velocity are however scarce.

The approach of Abers (2005) of stacking dispersion curves from intermediate depth arrivals from a range of back azimuths showed that dispersive arrivals from events occurring above 150 km may sample a waveguide with a greater velocity contrast than events occurring at greater than 150 km depth. Some receiver function studies have proposed that the velocity contrast of the low velocity reflector reduces with depth (e.g. Ferris *et al.,* 2003). The most recent and high resolution seismic tomographies are able to resolve the upper LVL, but do not image the low velocity oceanic crust over a great enough depth range to image changes in the velocity contrast due to dehydration reactions. Guided waves therefore present the best opportunity to detect these phase transformations as they spend most of their ray path trapped within the LVL, and so spend much longer sampling the low velocity oceanic crust than seismic phases used in other seismic techniques (see figure 2.1).

The observations presented in Chapter 6 therefore provide a new detailed seismic constraint on the velocity changes in the low velocity oceanic crust due to metamorphic reactions occurring during subduction. These observations suggest that low velocity hydrous mineralogies generally persist to greater depths than has been proposed by widely accepted thermo-petrological subduction zone models. The persistence of these low velocity hydrous mineralogies to greater depth may explain the cluster of seismicity that is seen at 200 – 250 km depth in the Northern Japan subduction zone, and suggests that mineral bound H_2O subducted in the oceanic crust may be transported to greater depth than has previously been suggested.

Low velocity structures may be due to subducted sedimentary material (e.g. Horleston & Helffrich, 2012). However the thickness of the LVL inferred in Chapter 6 greatly exceeds the thickness of the incoming sediments. It has also been proposed that the LVL may be a layer of serpentinite above the slab (e.g. Kawakatsu & Watada, 2007). The observations presented here however do not support this theory as it is unlikely that guided waves could be excited and propagate in a layer of serpentinised mantle above the slab (as discussed in section 2.2.2). Alternatively the LVL could be explained by anhydrous gabbro that has yet to undergo transformation to eclogite (e.g. Hacker 1996; Helffrich 1996). However the highly hydrated conditions that are inferred in Chapter 5 due to normal faulting in the incoming slab suggests that the occurrence of meta-stable anhydrous gabbro is unlikely.

By far the most widely favoured explanation for these low velocity layers is the persistence of blueschist and lawsonite facies rocks (e.g. Connolly & Kerrick, 2002; Hacker et al 2003a & b). As the subducted oceanic crust subducts and dehydrates with increasing temperature and pressures, this low velocity layer is predicted to become less seismically distinct (e.g. Hacker et al., 2003 a & b).

The observations presented in Chapter 6 also show that the phase transformations expected in subduction zone conditions of Northern Japan occur at greater depth than is suggested by established thermo-petrological models (e.g. Hacker *et al.,* 2003b). This poses the question, how can these mineralogies persist beyond the depths at which they are thought to be stable? There are essentially two possible explanations.

1. The subduction zone conditions are cooler than predicted by current subduction zone thermal models.
2. The predicted metamorphic reactions are inhibited.

The first of these explanations does not seem likely. Slab thermal modelling techniques are well established, are benchmarked to heat flux measurements at subduction zones, and there is no reason to suggest that the Hokkaido subduction zone is cooler than predicted. The second explanation may be more likely, as metamorphic reactions are not likely to occur instantaneously at the predicted P-T conditions. Metamorphic reactions may be delayed for instance due to a lack of water to catalyse reactions that lead to the mineral phase change.

The phase diagrams proposed for an altered MORB composition by various authors assume that the MORB is fully hydrated (e.g. Connolly & Kerrick, 2002; Hacker *et al.,* 2003), and the

mineral phases are calculated assuming a closed system (i.e. water released from dehydration reactions is assumed to be immobile).

In the subduction zone system however we know that some of the fluid released from dehydration reactions in the slab escapes into the mantle wedge. It is also possible that the incoming basaltic oceanic crust is not fully hydrated. These two factors could mean that the amount of water available to catalyse metamorphic reactions in the oceanic crust is limited. This could mean that parts of the crust may undergo a phase transformation, while other parts of the crust do not, giving a composite crustal velocity. The lack of water in the oceanic crust could therefore explain delay of the Blueschist-Amphibole transformation, and the persistence of metastable Lawsonite bearing assemblages to greater depths than inferred by fully hydrated closed system petrological models (e.g. Connolly & Kerrick, 2002; Hacker *et al.,* 2003b).

Guided wave studies in various subduction zones resolve low velocity structures to greater depth than receiver function studies in the same arc, as is summarised in table 2.2. It is possible that receiver functions may not be sensitive to the reduced velocity contrast that is inferred in the LVL at 200 km depth.

The increased dip of the slab at these depths would also mean that P-S conversions from the low velocity crust at these depths would only be seen at great distance from the trench (e.g. Mackenzie *et al.,* 2010). In the case of Northern Japan this could mean that the P-S conversions are only seen outside the aperture of the array, in the Sea of Japan. The limited inland extent of the seismic arrays used for receiver function analysis may be a common factor in why low velocity structure is not imaged by receiver function analysis in other subduction zones.

7.3 Water delivered to the deep mantle

Previous work on the global H_2O flux has focused on the amount of water that is transported to the mantle in a variety of subduction zone conditions (e.g. Rüpke *et al.,* 2004; Hacker *et al.,* 2008; van Keken *et al.,* 2011). A major source of uncertainty that is common to all of these estimates is the degree of hydration of the subducted slab mantle.

In Chapter 5 we present a case study using an original technique to quantify the degree of slab mantle hydration in the Northern Japan subduction zone, by quantifying the P-wave coda from events occurring below the upper plane of the WBZ. This analysis shows that the

slab mantle, hydrated by outer rise normal faults, has the potential to carry the majority of H_2O that is subducted beneath Northern Japan. Our estimates of the H_2O flux beneath Northern Japan are compared to published estimates in table 7.1. The published estimates are largely based on thermo-petrological models. They also estimate the degree of hydration of the incoming slab. Our methods however quantify the hydration of the slab mantle at intermediate depths. It is widely thought that some water would be lost from the slab between these depths, and therefore the published estimated quoted in table 7.1 may be an overestimate of the hydration predicted at intermediate depths by these published models.

Study	**Assumptions**	**Amount of water subducted per metre of arc (Tg/Myr)**		**Percentage of estimate carried in lithospheric mantle**
		In slab mantle (Tg/Myr/m)	**In whole lithosphere (Tg/Myr/m)**	
Rüpke *et al.* (2004)	Assuming 120 Myr old crust, and 6 cm/yr subduction rate	22.8	36.0	63.0 %
Van Keken *et al.* (2011) – no mantle serpentinisation	Using figures quoted for the Hokkaido trench	0.0	21.5	0.0 %
Van Keken *et al.* (2011) – 2 wt% serpentinisation		9.6	31.1	30.9 %
Van Keken *et al.* (2011) – Full serpentinisation		44.0	65.5	67.2 %
Iyer *et al.* (2012) – Extrapolated from CHILEAN observations	Assuming plate age and subduction rate for the Hokkaido trench from van Keken *et al.* (2011).	-	60.0	-
Iyer *et al.* (2012) – Extrapolated from NICURAGUAN observations		-	187.5	-
This study	Assuming the upper slab hydration of van Keken *et al.* (2011).	170.4 - 318.7	191.9 - 340.2	88.8 – 93.7 %

Table 7.1 – Comparison of slab mantle, and whole slab hydration from estimates from this and other studies.

Our estimates of the degree of slab hydration are significantly higher than existing observations, and an order of magnitude higher than the established estimates of Rüpke *et al.* (2004) and van Keken *et al.* (2011). Iyer *et al.* (2012) benchmark their thermo-petrological models to observations from South and Central America to provide a higher estimate of slab mantle hydration. The extrapolation of these models to subduction zone conditions found in Northern Japan gives the best agreement with the hydration we infer for Northern Japan. The maximum H_2O flux inferred by Iyer *et al.* (2012) for the subduction zone conditions found in Northern Japan is however only slightly greater than the minimum H_20 flux due to mantle hydration estimated in Chapter 5.

Rüpke *et al.* (2004) suggest that up to 40 % of the H_2O that is carried by this part of the slab can be transported to the deep mantle. This suggests that cool subduction zone conditions such as those found in Northern Japan may transport far larger amounts of water to the deep mantle than has previously been proposed. The persistence of hydrated MORB compositions also has implications for the water that is delivered to the mantle wedge. Van Keken *et al.* (2011) estimate that approximately 50 % of the mineral bound water subducted by the oceanic crust and sediments in Northern Japan leaves the slab at less than 150 km depth. This released water hydrates the mantle wedge, allowing melting to occur, and therefore causing arc volcanism. The observational constraint on the breakdown of MORB assemblages presented in Chapter 6 suggest that water may be retained in the crust to greater depths, meaning that less water would be returned to the Earth's surface via arc volcanism.

These two observations may provide a mechanism to explain the high water content of the mantle transition zone that is inferred from seismic (e.g. Lawrence & Wysession, 2006) and electrical conductivity studies (e.g. Karato, 2011). The hypothesis that such large amounts of water are delivered to the deep mantle by subduction would broadly support the theory of Bercovici & Karato, (2003), who advocate that the mantle transition acts as water filter preventing incompatible elements from crossing the 410 km boundary

7.4 Intermediate and deep focus seismicity

Our observations suggest that the gradual onset of eclogitization in the subduction zone beneath Northern Japan at 200 – 250 km depth may explain the abundance of seismicity seen at these depths in this arc. Fault zones that are proposed to explain dispersive arrivals

well below the surface of the slab, imply that lower plane seismicity may occur due to hydration of the subducting slab mantle via the low velocity fault zone structures. Our results therefore suggest that all intermediate depth events in the upper and lower plane of the WBZ occur in the presence of low velocity hydrous mineral assemblages. We conclude that dehydration embrittlement is a viable and likely mechanism by which all intermediate depth events beneath Northern Japan can occur.

This study also shows that hydrous mineral assemblages may persist to greater depth in the oceanic crust, and that the subducting lithospheric mantle may subduct large quantities of water to the transition zone. It is therefore possible that deep focus earthquakes occurring in old subducted plates may also be related to large amounts of H_2O that are inferred to be transported to 300 – 700 km depth in the hydrated slab mantle. We propose that deep focus earthquakes may also be explained by fluid processes, though no direct constraint on the mineralogies present at these depths are presented in this study.

7.5 Other observations

Analysis of arrivals from WBZ seismicity in the Northern Japan subduction zone have provided new constraint on the metamorphic reactions that occur during subduction, and have shown that low velocity outer rise fault zone structures are present at intermediate depths, and are directly related to lower plane WBZ seismicity. The methods developed in this study could be applied in other subduction zones, to test if similar low velocity structures exist in different subduction conditions. Below we present examples of dispersive arrivals observed from upper and lower WBZ seismicity in South America.

In the appendix we show observations of dispersed P-wave arrivals from events occurring at intermediate depths in the South American subduction zone. Delayed high frequency arrivals with elevated amplitude observed in this subduction zone have been attributed to a low velocity oceanic crust by previous guided wave studies in this area (e.g. Martin *et al.,* 2003; Martin & Rietbrock, 2006). The observations in the appendix show that the delay of the high frequency arrivals from upper plane events increases with the depth of the event, as the wave spends longer interacting with the waveguide.

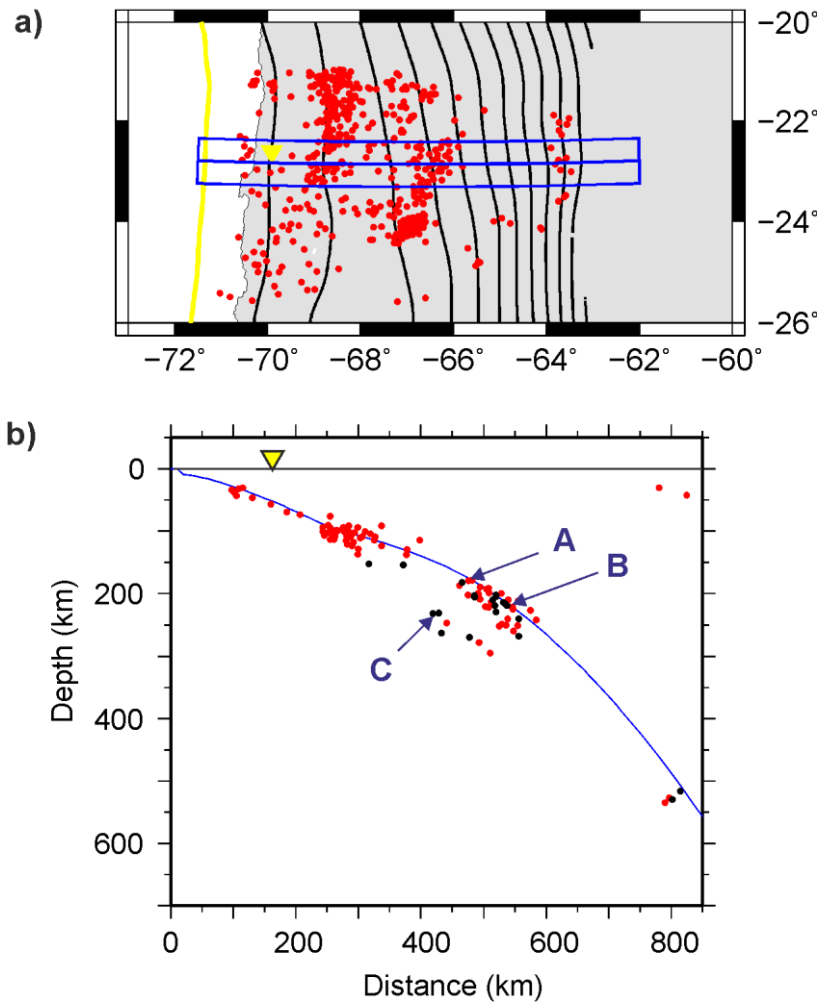

Figure 7.1 – Map and profile of WBZ occurring in Central Chile, and the station at which dispersive arrivals are observed. **a)** Area map. Seismicity from the EHB catalogue is shown by the red circles, and slab contours from *slab1.0* (Hayes *et al.,* 2012) are shown in black. The station at which the dispersive waveform are observed is shown by the inverted yellow triangle. The subduction zone trench is shown by a yellow line. **b)** Slab profile. Background seismicity from EHB catalogue is show in red. Waveforms from events shown in black are shown in figure A1 & A2. Station LVC is shown by the yellow triangle, and events shown in figure 7.2 are labelled A-C.

Examples of these waveforms recorded at the station LVC are plotted both as a spectrogram and in the velocity spectra are shown in figure 7.2. We note that the delayed frequencies seen in the forearc of South America are observed at higher frequency than in Northern Japan. The spectrogram and velocity spectra are therefore plotted from 0.125 – 16 Hz for these observations.

Dispersive arrivals are also seen from lower plane WBZ events in the Chilean forearc. We propose that these dispersive events are caused by low velocity normal fault structures in the WBZ beneath Central Chile, as has been shown for Northern Japan in chapter 5. This

observation suggests that low velocity hydrated fault zone structures in the WBZ may be present many subduction zones, and at a range of subduction zone conditions. The observations South American presented here present an exciting potential test for the hypothesis that the lithospheric mantle is highly hydrated by outer rise normal faults.

7.6 Further work

7.6.1 South American observations

Waveform modelling of the type performed for dispersive arrivals observed in Northern Japan may determine whether the dispersion from upper plane seismicity can be caused by a crustal waveguide, and if the dispersive arrivals from lower plane events can be described by low velocity fault zone waveguides.

Detailed modelling of these dispersive arrivals may provide constraint on the low velocity structure in the WBZ in this younger and hotter subduction zone. This work may therefore provide a test of the applicability of the methods developed here to other subduction zones, and of the prevalence of low velocity faulting in the slab mantle in other subduction zones. Thermo-petrological models predict the velocity structure of the subducted crust to be different in warm subduction zone conditions such as these. Observations from South America may therefore provide an additional test for the established subduction zone petrology models.

7.6.2 Scattering analysis

The coda analysis presented in Chapter 5 has the potential to constrain the degree of hydration in other subduction zones. This is particularly important for younger hotter subduction zones as they are expected to carry less water in the lithospheric mantle (e.g. Iyer *et al.,* 2012). Understanding the amount of water subducted by subduction zones with a range of thermal parameters may allow a more comprehensive estimate of the amount of water subducted by the hydrated lithospheric mantle globally. To this end, coda analysis could be performed on arrivals from intermediate depth earthquakes at several temporary deployments above the South and Central American subduction zones.

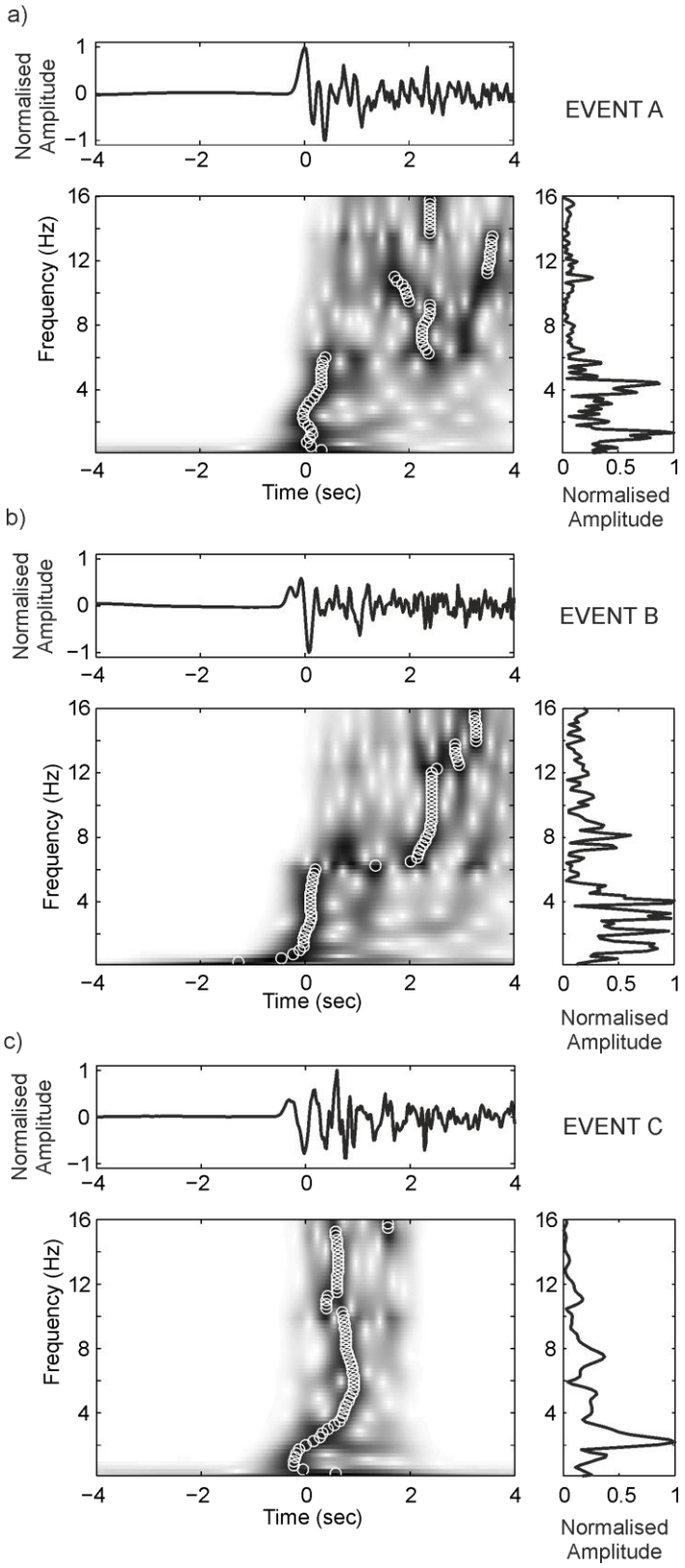

Figure 7.2 – Example dispersion curves from three WBZ events, from the upper plane of the WBZ (**a** & **b**) and lower plane of the WBZ (**c**) The location of these events is shown on the profile in figure 7.1. The lower left panel shows the spectrogram of the signal, the right hand panel shows the velocity spectra of the signal and the upper panel shows the unfiltered waveform.

7.6.3 Petrological modelling

The observations from Northern Japan arguably provide the first independent constraint on the velocity changes due to dehydration reactions that occur during subduction. We suggest that partial hydration of the oceanic crust may allow for the persistence of low velocity minerals to greater depth than is inferred from existing modes (such as the subduction factory models of Hacker *et al.* 2003 a & b; van Keken *et al.* 2011).

This hypothesis however needs to be to be tested for Northern Japan using a model setup similar to the subduction factory papers to calculate the mineralogies that may be present if a fully hydrated closed system is not assumed. Phase diagrams for these less hydrated altered MORB conditions could be calculated following the methodology of Connolly & Kerrick (2002). Subduction zone thermal models may then be used to simulate the temperature and pressure conditions found in Northern Japan subduction zone (e.g. Syracuse *et al.,* 2010).

Ultimately though, the occurrence of metamorphic reactions in the subducting plate needs to be calculated at the same time as the pressure-temperature conditions, allowing feedbacks such as changes in density, volume and water content to be accounted for. This may allow a more precise prediction of where given metamorphic phases occur in a subduction zone, rather than where they are stable as is done in the subduction factory modelling approach. This may also lead to a refinement of the estimated global H_2O flux in subduction zones, and the recent detailed claims of which mineralogies lead to intermediate depth WBZ in various different subduction zones (e.g. van Keken *et al.,* 2012; Abers *et al.,* 2013).

7.7 Summary

Guided wave observations in Northern Japan have shown that both upper and lower plane intermediate depth seismicity are associated with low velocity mineral assemblages. The upper plane of seismicity is associated with hydrated oceanic crust, while the lower plane of seismicity is associated with hydration due to outer rise normal faulting. These observations suggest that both the upper and lower plane WBZ seismicity can be explained by dehydration embrittlement.

Our observations also suggest that large amounts of water may be delivered to the deep mantle by the hydrated subducting lithospheric mantle. As the composition of upper

mantle derived MORBs are largely anhydrous it seems unlikely that the large amounts of water that are inferred to be subducted in cool subduction zone conditions are delivered to the asthenosphere. The assertion that large amounts of water are subducted to the deep mantle supports the hypothesis that the mantle transition zone is highly hydrated and acts as a filter, retaining water delivered by subduction (e.g. Bercovicic & Karato, 2003).

Chapter 8

Conclusions

In this project we have shown that guided waves are sensitive to features of the WBZ velocity structure that are not resolved by other seismic imaging techniques. This has allowed us to address some of the key questions about the structure of the WBZ that are not fully understood, and were highlighted at the end of chapter 2. To conclude we outline what has been addressed in each of these key questions, before summarising the potential further work.

8.1 Fault zone structures in the subducted mantle beneath Northern Japan

We present the first observational evidence that hydrated normal fault structures are present at intermediate depths. The low velocity hydrated fault zones act as a waveguide, transferring high frequency energy to the overriding oceanic crustal waveguide. These fault zone waveguides are 2 – 3 km thick, and have a velocity 12 - 15 % slower than the surrounding material. We interpret these dipping low velocity waveguides as hydrated outer rise normal faults that are 50 – 71 % hydrated.

The fact that guided wave dispersion is excited from these events suggests that lower plane WBZ events are directly associated with hydrous, low velocity mineralogies. While guided wave dispersion is not seen for every event occurring at depth in the WBZ, extended P-wave coda is seen at stations close to the trench for all the events we have looked at, suggesting that these events also occur close to low velocity structures. Therefore we conclude that lower plane WBZ seismicity in Northern Japan occurs in the presence of low velocity hydrous mineral assemblages, and is therefore likely to occur through dehydration embrittlement.

8.2 Hydration of the subducting lithospheric mantle

We suggest that these low velocity normal faults that are present in the WBZ may lead to the extended P-wave coda that is seen in arrivals from WBZ events, observed at stations close to the trench in the Northern Japan subduction zone. Analysis of the P-wave coda observed from intermediate depth WBZ events at 100 – 150 km depth suggests that the subducting lithospheric mantle may be 17.4 – 31.1 % serpentinised by outer rise normal faults structures that persist to intermediate depths.

This suggests that the hydrated lithospheric mantle alone subducts 170.4 - 318.7 Tg/Myr of water per metre of trench. Taken with the estimate of van Keken *et al.* (2011) for the upper slab this suggests that in total 191.9 - 340.2 Tg/Myr of water per metre of trench is subducted beneath northern Japan. This implies that approximately 90 % of the water subducted beneath Northern Japan is transported by the hydrated lithospheric mantle. As much of the water in the cool lithospheric mantle may be transported to great depths (e.g. Rüpke *et al.,* 2004), we advocate that large amounts of water are transported to the mantle transition zone, supporting the hypothesis that the transition zone may be highly hydrated.

8.3 Depth of phase changes in the subducted oceanic crust

The guided wave analysis presented here gives the first detailed constraint of the velocity reduction in the subducted oceanic crust as metamorphic dehydration reactions occur. We infer that an 8 km thick low velocity crustal waveguide persist at up to 220 km depth beneath Japan. We show that the velocity contrast of the crust decreases with depth, which is interpreted as the progressive dehydration of the crust.

Our analysis shows that lawsonite bearing hydrous mineral assemblages persist to depths of up to 220 km. The low velocities seen at 100 – 150 km depth also suggest that blueschist assemblages may persist to these depths. This is much deeper than is suggested by established thermo-petrological models (e.g. Hacker *et al.,* 2003b) or imaged by receiver function studies (e.g. Kawakatsu & Watada, 2007). The persistence of blueschist bearing assemblages to > 100 km depth, and the persistence of lawsonite bearing assemblages up to 220 km depth may be explained by limited water in the oceanic crust due to partial hydration of the oceanic crust, and water that is lost to the mantle wedge. Receiver function studies may not image low velocity structure at these depths due to the relatively low velocity contrast, the steeper dip of the slab, and the limited aperture of seismic arrays

used for receiver function analysis. The deep persistence of hydrous mineral assemblages may explain the cluster of seismicity seen at 200 – 250 km depth below Northern Japan, and suggests that mineral bound water in the oceanic crust may be transported to greater depth than previously thought.

8.4 Further work

Analysis of dispersive arrivals observed from other subduction zones, e.g. South America, may give a constraint on the dehydration reactions that occur as younger, hotter oceanic crust subducts. Quantifying the lithospheric mantle hydration at intermediate depths in other subduction zones may allow a better estimate of the global H_2O flux to the mantle due to subduction. Applying the methods presented here to a greater range of subduction zones may give further insights into the role of fluids in the WBZ during subduction, as well as the significance of subducted fluids to the global water cycle.

References

Abers, G. A., 2000. Hydrated subducted crust at 100-250 km depth. *Earth and Planetary Science Letters.* Vol. **176**, Pg. 323-330.

Abers, G. A., 2005. Seismic low-velocity layer at the top of subducting slabs: observations, predictions, and systematics. *Physics of the Earth and Planetary Interiors,* Vol. **149,** Pg. 7-29.

Abers, G.A. & Sarker, G., 1996. Dispersion of regional body waves at 100-150 km depth beneath Alaska: In situ constraints on metamorphism of subducted crust. *Geophysical Research Letters,* Vol. **23**, No. 10, Pg. 1171-1174.

Abers, G.A., Nakajima, J., van Keken, P.E., Kita, S., & Hacker, B.R., 2013. Thermal–petrological controls on the location of earthquakes within subducting plates. *Earth and Planetary Science Letters*, Vol. **369–370**, Pg. 178–187

Abers, G.A., Plank, T., & Hacker B.R., 2003. The wet Nicaraguan slab. *Geophysical Research Letters*, Vol. **30**, No. 2, 1098, doi:10.1029/2002GL015649.

Ben-Zion, Y., 1998. Properties of seismic fault zone waves and their utility for imaging low velocity structures*, J. Geophys. Res*., Vol. **103**, Pg.12,567–12,585.

Bercovici, D., & Karato, S., 2003. Whole mantle convection and the transition-zone water filter*. Nature,* Vol. **425**, Pg. 39–44.

Berenger, J., 1994. A Perfectly Matched Layer for the Absorption of Electromagnetic Waves, *Journal of Computational Physics,* Vol. **114**, Pg. 185-200.

Blanch, J., Robertsson, J., & Symes, W., 1995. Modeling of a constant Q: Methodology and algorithm for an efficient and optimally inexpensive viscoelastic technique. *Geophysics,* Vol. **60**, No. 1, Pg. 176-184.

Bohlen, T., 2002. Parallel 3-D viscoelastic finite difference seismic modelling. *Computers & Geosciences,* Vol. **28**, Pg. 887-899.

Bohlen, T., 1998. Viskoelastische FD-Modellierung seismischer Wellen zur Interpretation gemessener Seismogramme, (Visco-elastic seismic FD modelling for the interpretation of measured seismograms), PhD thesis, Kiel University, (in German).

Bohlen, T., De Nil, D., Köhn, D., & Jetschny, S., 2011. SOFI3D – seismic modeling with finite differences, 3D acoustic and elastic version. Karlsruhe Institute of Technology, Karlsruhe, Germany.

Brudzinski, M. R., Thurber, C. H., Hacker, B. R., & Engdahl R., 2007. Global Prevalence of Double Benioff Zones. *Science*, Vol. **316**, Pg. 1472-1474.

Cerjan, C., Kosloff, D., Kosloff, R., & Reshef, M., 1985. A nonreflecting boundary condition for discrete acoustic and elastic wave equations. *Geophysics,* Vol. **50**, Pg. 705–708.

Collino, F., & Tsogka, C. 2001. Application of the perfectly matched absorbing layer model to the linear elastodynamic problem in anisotropic heterogeneous media. *Geophysics,* Vol. **66**, No. 1, Pg. 294–307.

Connolly, J. A. D. & Kerrick D. M., 2002. Metamorphic controls on seismic velocity of subducted oceanic crust at 100-250 km depth. *Earth and Planetary Science Letters,* Vol**. 204,** Pg. 61-74.

Coutant, O., Virieux, J., & Zollo, A., 1995. Numerical Source Implementation in a 2D Finite Difference Scheme for Wave Propagation. *Bull. Seis. Soc. Am.,* Vol. **85**, No. 5, Pg. 1507-1512.

Dorbath, C., Gerbault, M., Carlier, G., & Guiraud M., 2008. Double seismic zone of the Nazca plate in northern Chile: High-resolution velocity structure, petrological implications, and thermomechanical modeling. *Geochemistry, Geophysics, Geosystems*, Vol. **9**, No. 7, Q07006, doi:10.1029/2008GC002020.

Dziewonski, A., Bloch, S., & Landisman, M., 1969. A technique for the analysis of transient seismic signals. *Bull. Seism. Soc. Am.*, Vol., **59**, Pg., 427–444.

Emmerich, H., & Korn, M.,1987. Incorporation of attenuation into time-domain computations of seismic wave fields. *Geophysics,* Vol. **52**, No. 9, Pg. 1252-1264.

Engdahl, R.E., van der Hilst, R., & Buland, R., 1998. Global teleseismic earthquake relocation with improved travel times and procedures for depth determination. *Bull. Seis. Soc. Am., Vol.* **88**, No. 3, Pg. 722-743.

Essen, K., Braatz, M., Ceranna, L., Friederich, W., & Meier., T, 2009. Numerical modelling of seismic wave propagation along the plate contact of the Hellenic Subduction Zone - the influence of a deep subduction channel. *Geophys. J. Int.,* **179**, 1737–1756.

Faccenda, M., Gerya T. V. & Burlini L., 2009. Deep slab hydration induced by bending-related variations in tectonic pressure. *Nature Geoscience,* Vol. **2**, Pg. 790-793.

Faccenda, M., Gerya T. V., Mancktelow, N. S. & Moresi, L., 2012. Fluid flow during slab unbending and dehydration: Implications for intermediate-depth seismicity, slab weakening and deep water recycling. *Geochemistry, Geophysics, Geosystems,* Vol. **13**. Q01010, doi:10.1029/2011GC003860.

Ferris, A., Abers A.G., Christensen, D.H., & Veenstra, E., 2003. High resolution image of the subducted Pacific (?) plate beneath central Alaska, 50-150 km depth. *Earth and Planetary Science Letters,* Vol. **214,** Pg. 575-588.

Fowler, C.M.R., 2005. The Solid Earth: An Introduction to Global Geophysics. Second Edition, Cambridge University Press.

Frohlich, C., 2006. Deep Earthquakes. First Edition, Cambridge University Press.

Fry, A., 2010. Modelling stress accumulation and dissipation in subducting lithosphere and the origin of double and triple seismic zones. PhD thesis, University of Liverpool.

Furumura, T., & Kennett B., 2005. Subduction zone guided waves and the heterogeneity of the subducted plate: Intensity anomalies in Northern Japan. *Journal of Geophysical Research,* Vol. **110**, B10302, doi:10.1029/2004JB003486.

Garth, T. & Rietbrock, A., 2014, Order of magnitude increase in subducted H_2O due to hydrated normal faults within the Wadati-Benioff zone, *Geology* (published on line) doi:10.1130/G34730.1

Graves, R.W., 1996. Simulating Seismic Wave Propagation in 3D Elastic Media Using Staggered-Grid Finite Differences. *Bull. Seis. Soc. Am.,* Vol. **86**, No. 4, pp. 1091-1106.

Grevemeyer, I., Kaul, N., Diaz-Naveas, J. L., Villinger, H. W., Ranero, C. R. & Reichert C.2005. Heat flow and bending-related faulting at subduction trenches: Case studies of offshore Nicaragua and Central Chile. *Earth and Planetary Science Letters*, Vol. **236**, Pg. 238-248.

Grevemeyer, I., Ranero, C. R., Flueh, E. R., Kläschen, D. & Bialas, J., 2005. Passive and active seismological study of bending-related faulting and mantle serpeninization at the Middle American trench. *Earth and Planetary Science Letters*, Vol. **258**, Pg. 528-542.

Grove, T.L. Till, C.B., Lev, E., Chatterjee, N., & Médard, E., 2009. Kinematic variables and water transport control the formation and location of arc volcanoes. *Nature,* Vol. **459**, Pg. 694 – 697.

Gubbins, D., & Snieder, R., 1991. Dispersion of P Waves in Subducted Lithosphere: Evidence for an Eclogite Layer. *Journal of Geophysical Research,* Vol. **96**, No. B4, Pg. 6321-6333.

Gubbins, D., Barnicoat, A., & Cann, J., 1994. Seismological constraints on the gabbro-eclogite transition in subducted oceanic crust. *Earth and Planetary Science Letters*, Vol. **122**, Pg. 89-101.

Haberland, C., & Rietbrock, A., 2001. Attenuation tomography in the western central Andes, A detailed insight into the structure of a magmatic arc. *Journal of Geophysical Research,* Vol. **106**, Pg. 11,151-11,167.

Hacker, B. R. & Abers, G. A., 2004. Subduction factory 3: An Excel worksheet and macro for calculating the densities, seismic wave speeds, and H_2O contents of minerals and rocks at pressure and temperature. *Geochemistry, Geophysics, Geosystems*, Vol. **5**, Q01005, doi:10.1029/2003GC000614.

Hacker, B. R., Abers, G. A. & Peacock S. M., 2003a. Subduction factory, 1, Theoretical mineralogy, densities, seismic wave speeds, and H_2O contents. *Journal of Geophysical Research*, Vol. **108**, (B1), 2029, doi:10.1029/2001JB001127.

Hacker, B. R., Peacock S. M., Abers, G. A., & Holloway, S. D., 2003b. Subduction Factory 2. Are intermediate-depth earthquakes in subducting slabs linked to metamorphic dehydration reactions? *Journal of Geophysical Research*, Vol. **108**, (B1), 2030, doi10.1029/2001JB001129.

Hacker, B.R., 1996. Eclogite formation and the rheology, buoyancy, seismicity and H_2O content of oceanic crust. AGU Geophys. Monographs 96, Pg. 337–346.

Hacker, B.R., 2008. H_2O subduction beyond arcs. *Geochemistry, Geophysics, Geosystems,* Vol. **9**, No. 3, Q03001, doi:10.1029/2007GC001707.

Hasegawa, A., Umino, N., & Takagi, A., 1978. Double-planed deep seismic zone and upper mantle structure in the Northeastern Japan arc. *Geophys. J. R. astr. Soc.,* Vol. **54**, Pg. 281-296.

Hayes, G.P. & Wald, D.J., 2009. Developing framework to constrain the geometry of the seismic rupture plane on subduction interfaces a priori – a probabilistic approach. *Geophys. J. Int.,* Vol. **176**, Pg. 951-964.

Hayes, G.P., Wald, D.J. & Johnson, R.L., 2012. Slab1.0: A three-dimensional model of global subduction zone geometries. *Journal of Geophysical Research*, Vol. **117,** B01302, doi;10.1029/2011JB008524.

Helffrich, G., & Abers, G.A., 1997. Slab low-velocity in the eastern Aleutian subduction zone. *Geophys. J. Int.,* Vol. **130**, Pg. 640-648.

Helffrich, G., 1996. Subducted lithospheric slab velocity structure: Observations and mineralogical inferences. *Geophysical Monograph series,* Vol. **96**, Subduction Top to Bottom, Pg. 215-222.

Hirth, G. & Kohlstedt, D. L., 1996. Water in the oceanic upper mantle: implications for rheology, melt extraction and the evolution of the lithosphere. *Earth Planetary Science Letters*, Vol. **144**, Pg. 93-108.

Hischmann, M. M., 2006. Water, Melting, and the Deep Earth H_2O cycle. *Annual Reviews Earth and Planetary Sciences*, Vol**. 34**, Pg. 629-653.

Hori, S., Inoue, H., Fukao, Y., & Ukawa, M., 1985. Seismic detection of the untransformed 'basaltic' oceanic crust subducting into the mantle. *Geophys. J. R. Astr. Soc.*, Vol. **83**, Pg. 169-197.

Horleston, A.C. &Helffrich, G.R. 2012. Constraining sediment subduction: A converted phase study of the Aleutians and Marianas*. Earth and Planetary Science Letters*, Vol. 359‐360, Pg. 141‐151.

Iyer, K., Rüpke, L. H., Phipps Morgan, J. & Grevemeyer I., 2012. Controls of faulting and reaction kinetics on serpentinization and double Benioff zones. *Geochemistry, Geophysics, Geosystems,* Vol. **13.** Q09010, doi:10.1029/2012GC004304.

Jacobsen, S. D. & van der Lee, S., 2006. Preface: Earth's Deep Water Cycle. *Geophysical Monograph Series,* Vol. 168.

John, T., Medvedev, S., Rüpke, L.H., Andersen, T.B., Podladchikov, Y.Y., & Austrheim, H., 2009. *Nature Geoscience,* Vol. 2, Pg. 137-140.

Karato, S., 2011. Water distribution across the mantle transition zone and its implications for global material circulation. *Earth and Planetary Science Letters.* Vol. 301, Pg. 413–423.

Kawakatsu, H., & Watada, S., 2007. Seismic Evidence for Deep-Water Transportation in the Mantle. *Science*, Vol. 316, Pg. 1468-1471.

Keleman, P.B. & Hirth, G. 2007. A periodic shear-heating mechanism for intermediate-depth earthquakes in the mantle. *Nature,* Vol. 446, Pg. 787-790.

Kirby, S., Engdahl, E.R., & Denlinger, R., 1996a. Intermediate-Depth Intraslab Earthquakes and Arc Volcanism as Physical Expressions of Crustal and Uppermost Mantle Metamorphism in Subducting Slabs. *Geophysical Monograph series*, Vol. 96, Subduction Top to Bottom, Pg. 195-214.

Kirby, S.H., Stein, S., Okal, E.A., & Rubie, D.C., 1996b. Metastable mantle phase transformations and deep earthquakes in subducting oceanic lithosphere, *Rev. Geophys.,* Vol. 34, Issue 2, Pg. 261–306.

Komatitsch, D., & Martin, R., 2007. An unsplit convolutional perfectly matched layer improved at grazing incidence for the seismic wave equation. *Geophysics*, Vol. **72**, No. 5, SM155 – SM167

Lawrence, J.F. & Wysession, 2006. Seismic Evidence for Subduction-Transported Water in the Lower Mantle. *Geophysical Monograph Series*, Vol. **168**, Pg. 251-261.

Lefeldt, M., Ranero, C.R., & Grevemeyer, I., 2012. Seismic evidence of tectonic control on the depth of water influx into incoming oceanic plates at subduction trenches. *Geochemistry, Geophysics, Geosystems*, Vol. **13**, No. 5, Q05013, doi:10.1029/2012GC004043, ISSN: 1525-2027.

Levander, A. R., 1988. Fourth-order finite-difference P-SV seismograms. *Geophysics,* Vol. **53**, No. 11, Pg., 1425-1436.

MacKenzie, L.S., Abers, G.A., Rondenay, S., & Fischer, K.M., 2010. Imaging a steeply dipping subducting slab in Southern Central America. *Earth and Planetary Science Letters*, Vol. **296**, Pg. 459–468,

Madariaga, R., 1976. Dynamics of a circular expanding fault. *Bull. Seis. Soc. Am.,* Vol. **66**, Pg. 639-66.

Martin, R., & Komatitsch, D., 2009. An unsplit convolutional perfectly matched layer technique improved at grazing incidence for the viscoelastic wave equation. *Geophys. J. Int.,* Vol. **179**, Pg. 333-344.

Martin, S. & Rietbrock, A., 2006. Guided waves at subduction zones: dependencies on slab geometry, receiver locations and earthquake sources. *Geophysical Journal International*, Vol**. 167**, Pg. 693-704.

Martin, S., Rietbrock, A., Haberland, C. & Asch, 2003. Guided waves propagating in subducted oceanic crust. *Journal of Geophysical Research*, Vol. **108**, No. B11, 2536, doi 1029/2003JB002450.

Matsuzawa, T., Umino, U., Hasegawa, A., & Takagi, A., 1986. Upper mantle velocity structure estimated from PS-converted wave beneath the north-eastern Japan Arc. *Geophys. J. R. astr. Soc.,* Vol. **86**, Pg. 767-787.

Mitronovas, W., & Isacks, B.L., 1971. Seismic velocity anomalies in the upper mantle beneath the Tonga-Kermadec Island Arc. *Journal of Geophysical Research*, Vol. **76**, Pg. 7154–7180.

Miyoshi, T., Saito, S., & Shiomi, K., 2012. Waveguide effects within the Philippine Sea slab beneath southwest Japan inferred from guided *SP* converted waves. *Geophys. J. Int.,* Vol. **189**, Pg. 1075–1084.

Myhill R., & Warren, L.M., 2012. Fault plane orientations of deep earthquakes in the Izu-Bonin-Marianas subduction zone. *J. Geophys. Res.,* Vol. **117**, B06307, doi:10.1029/2011JB009047.

Nakajima, J., Tsuji, Y., Hasegawa, A., Kita, S., Okada, T., & Matsuzawa, T., 2009. Tomographic imaging of the hydrated crust and mantle in the subducting Pacific slab beneath Hokkaido, Japan: Evidence for dehydration embrittlement as a cause of intra slab earthquakes. *Gondwana Research*, Vol. **16**, Pg. 470-481.

Okada, H., 1971. Forerunners of *ScS* waves from nearby deep earthquakes and upper mantle structure in Hokkaido. *Zisin. Ser, II,* Vol. **24**, Pg. 228-239 (in Japanese).

Peacock, S. M. & Wang, K., 1999. Seismic Consequences of Warm Versus Cool Subduction Metamorphism: Examples from Southwest and Northeast Japan. *Science,* Vol. **286**, Pg. 937-939.

Peacock, S.M., 2001. Are the lower planes of double seismic zones caused by serpentine dehydration in subducting oceanic mantle? *Geology*, Vol. **29**, No. 4, Pg. 299–302.

Moczo, P., 1998. INTRODUCTION TO MODELING SEISMIC WAVE PROPAGATION BY THE FINITE DIFFERENCE METHOD. Lecture Notes: Lectures given at Disaster Prevention Research Institute, Kyoto University during author's visit from Sep. 7, 1997 to Jan. 9, 1998.

Ranero, C. R., Phipps Morgan, J., McIntosh, K. & Reichert C., 2003. Bending-related faulting and mantle serpentinization at the Middle America trench. *Nature,* Vol. **425,** Pg. 367-425.

Ranero, C. R., Villaseñor, A., Phipps Morgan, J. & Weinrebe, W., 2005. Relationship between bend-faulting at trenches and intermediate depth seismicity. *Geochemistry, Geophysics, Geosystems,* Vol. **6**. Q12002, doi:10.1029/2005GC000997.

Ranero, C.R., & Sallarés, V., 2004. Geophysical evidence for hydration of the crust and mantle of the Nazca plate during bending at the north Chile trench. *Geology*, Vol. **32**; No. 7; Pg. 549–552.

Robertsson, J.O.A., Blanch, J.O., & Symes, W.W., 1994. Viscoelastic finite-difference modeling. *Geophysics,* Vol., **59**, No., 9, Pg., 1444-1456.

Rondenay, S., Abers, G.A., & van Keken, P.E., 2008. Seismic imaging of subduction zone metamorphism. *Geology,* Vol. **36**, Pg. 275–278.

Rüpke, L., Morgan, J.P., & Dixon, J.E., 2006. Implications of Subduction Rehydration for Earth's Deep Water Cycle, Earth's Deep Water Cycle. *Geophysical Monograph Series*, Vol. **168**., Pg. 263-276.

Rüpke, L.H., Phipps Morgan, J., Hort, M., & Connolly, A. D., 2004. Serpentine and the subduction zone water cycle. *Earth and Planetary Science Letters,* Vol. **223,** Pg. 17-34.

Rychert, C.A., Fischer, K. M., Abers, G.A., Plank, T., Syracuse, E., Protti, J.M., Gonzalez, V., & Strauch W. (2008), Strong along-arc variations in attenuation in the mantle

wedge beneath Costa Rica and Nicaragua, *Geochem. Geophys. Geosyst.*, Vol. **9**, Q10S10, doi:10.1029/2008GC002040.

Shapiro, N.M., Olsen, K.B., & Singh S.K., 2000. Wave-guide effects in subduction zones: evidence from three-dimensional modelling. *Geophysical Research Letters*, Vol. **27**, No. 3, Pg. 433-436.

Shito, A., Suetsugu, D., Furumura, T., Sugioka, H., & Ito, A., 2013. Small-scale heterogeneities in the oceanic lithosphere inferred from guided waves. *Geophysical Research Letters*, Vol. **40**, Pg. 1708–1712.

Snoke, A., Sacks, I.S., & Okada, H., 1977. Determination of the subducting lithosphere boundary by use of converted phases. *Bulletin of the Seismological Society of America*, Vol. **67**, Pg. 1051-1060.

Stein, S., & Stein, C.A., 1996. Thermo-mechanical evolution of oceanic lithosphere: Implications for the subduction process and deep earthquakes. *Geophysical Monograph series*, Vol. **96**, Subduction Top to Bottom, Pg. 1-17.

Syracuse, E. M., & G. A. Abers (2006), Global compilation of variations in slab depth beneath arc volcanoes and implications, *Geochem. Geophys. Geosyst.,* Vol. **7**, Q05017, doi:10.1029/2005GC001045.

Syracuse, E. M., van Keken P. E. & Abers G. A., 2010. The global range of subduction zone thermal models. *Physics of the Earth and Planetary Interiors*, Vol. **183,** Pg. 73-90.

Syracuse, E.M., Abers, G.A., Fischer, K., MacKenzie, L., Rychert, C., Protti, M., González., V., & Strauch, W., 2008. Seismic tomography and earthquake locations in the Nicaraguan and Costa Rican upper mantle. *Geochemistry, Geophysics, Geosystems*, Vol. **9**, No. 7, Q07S08, doi:10.1029/2008GC001963, ISSN: 1525-2027.

Syracuse, E.M., van Keken, P.E., & Abers, G.A., 2010. The global range of subduction zone thermal models. *Physics of the Earth and Planetary Interiors*, Vol. **183**, Pg. 73–90.

Tsumura, N., Matmoto, S., Horiuchi, S., & Hasegawa, A., 2000. Three-dimensional attenuation structure beneath the northeastern Japan arc estimated from spectra of small earthquakes. *Tectonophysics,* Vol. **319**, Pg. 241-260.

Umino, N., & Hasegawa, A., 1975. On the two-layered structure of deep seismic plane in Northeastern Japan Arc, *J. seism. Soc. Japan, Ser. II*, Vol. **28**, Pg. 125-139 (in Japanese).

van der Hilst, R.D., Engdahl, E.R., Spakman, W., & Guust, N.,1991. Tomographic imaging of subducted lithosphere below northwest Pacific island arc. *Nature,* Vol., **353**, Pg. 37–43.

van Keken P.E., Kita S., & Nakajima, J., 2012. Thermal structure and intermediate-depth seismicity in the Tohoku-Hokkaido subduction zones. *Solid Earth,* Vol. **3**, Pg. 355-364.

van Keken, P. E., Hacker, B. R., Syracuse, E. M., & Abers, G. A., 2011. Subduction factory: 4. Depth-dependent flux of H_2O from subducting slabs worldwide. *Journal of Geophysical Research*, Vol. **116,** B01401, doi:10.1029/2010JB007922

Virieux, J., 1986. P-SV wave propagation in heterogeneous media: Velocity-stress finite-difference method. *Geophysics*, Vol., **51**, No., 4, Pg., 889-901.

Wadati, K., 1935. On the activity of deep-focus earthquakes in the Japan Islands and neighbourhoods. *Geophys. Mag.,* Vol. **8**, Pg. 119-145.

Warren, L. M., & Silver, P.G., 2006. Measurement of differential rupture durations as constraints on the source finiteness of deep earthquakes. *J. Geophys. Res.,* Vol. **111**, B06304, doi:10.1029/2005JB004001.

Warren, L. M., Langstaff, M.A. & Silver, P.G., 2008. Fault plane orientations of intermediate-depth earthquakes in the Middle America Trench, J*. Geophys. Res.,* Vol. **113**, B01304, doi:10.1029/2007JB005028.

Warren, L.M., Hughes, A.N. & Silver, P.G., 2007. Earthquake mechanics and deformation in the Tonga-Kermadec subduction zone from fault plane orientations of intermediate- and deep-focus earthquakes. *J. Geophys. Res.,* Vol. **112**, B05314, doi:10.1029/2006JB004677.

Worzewski, A., Jegen, M., Kopp, H., Brasse, H. & Taylor Castillo, W., 2011. Magnetotelluric image of the fluid cycle in the Costa Rican subduction zone. *Nature Geoscience,* Vol. **4,** Pg. 108-111.

Yamasaki, T., & Seno T., (2003). Double seismic zone and dehydration embrittlement of the subducting slab. *J. Geophys. Res.,* Vol. **108**, No. B4, 2212, oi:10.1029/2002JB001918.

Yoon, M., 2005. Deep Seismic Imaging in the presence of Heterogeneous Overburden: Numerical Modelling and Case Studies from the Central Andes and Southern Andes, PhD thesis, Free University of Berlin, Berlin.

Yuan, X., Sobolev, S.V., Kind, R., Oncken, O., Bock, G., & the Andes Working Group, 2000. Subduction and collision processes in the Central Andes constrained by converted seismic phases. *Nature,* Vol. **408**, Pg. 958-961.

Zhang, H., Thurber, C. H., Shelly, D., Ide, S., Beroza, G., & Hasegawa, A., 2004. High-resolution subducting-slab structure beneath northern Honshu, Japan, revealed by double-difference tomography. *Geology,* Vol. **32,** Pg. 361-364.

Appendix

Dispersive P-wave Arrivals in South America

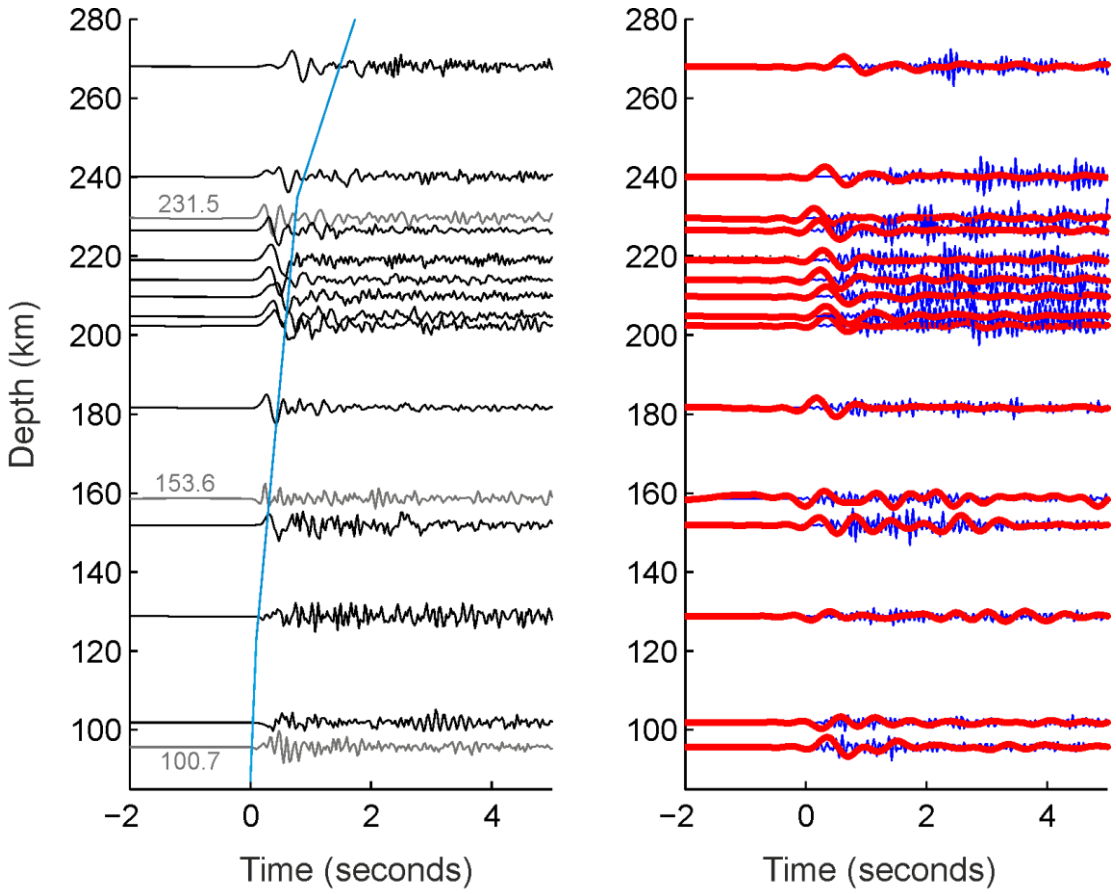

Figure A1 – Dispersive waveforms from upper plane intermediate depth events recorded at the station LVC. Left panel shows the full waveform (black) band pass filtered between 0.25 - 16 Hz. Black traces are plotted at the event depth. Grey traces are plotted away from their true for clarity, and there depth is shown by the grey labels. The light blue line shows the approximated arrival of the high frequencies, which increases with earthquake focal depth. The right panel shows the high pass (> 8 Hz) and low pass (< 2 Hz) filtered waveforms in blue and red respectively.

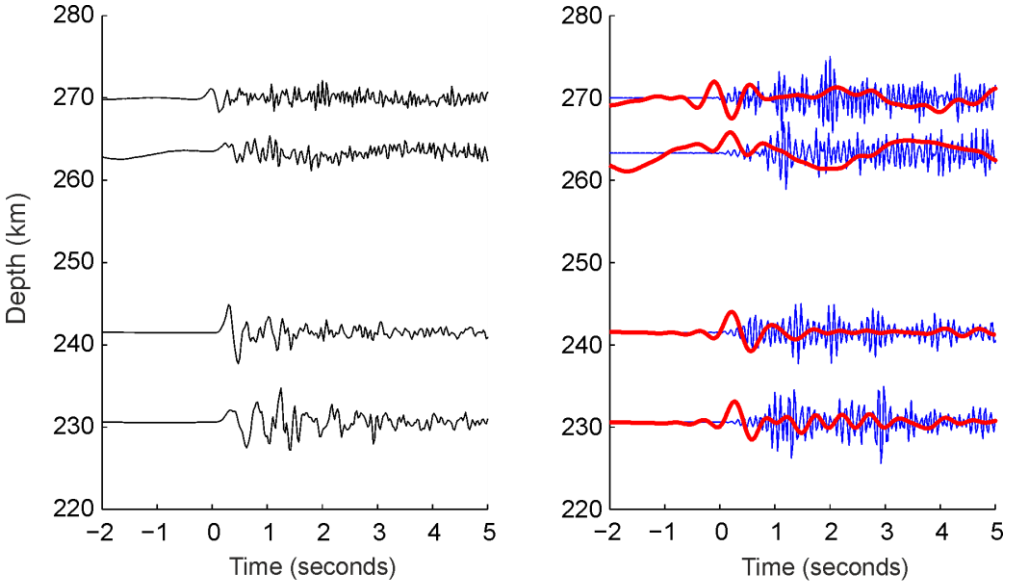

Figure A2 – Dispersive waveforms from lower plane intermediate depth events recorded at the station LVC. Left panel and right panel are as in figure A1.